Electrical impedance studies of uranium dioxide

Hampton, Robert Nigel

Award date:
1986

Awarding institution:
University of Bath

ELECTRICAL IMPEDANCE STUDIES OF URANIUM DIOXIDE

submitted by

Robert Nigel Hampton

for the degree of Ph D

of the University of Bath

1986

ProQuest LLC
789 East Eisenhower Parkway
P.O. Box 1346
Ann Arbor, MI 48106-1346

ABSTRACT

Complex impedance techniques have enabled the equivalent circuit of single crystal uranium dioxide discs to be established as two parallel combinations of conductances and capacitances connected in series. The parallel combinations have been shown to relate to a boundary layer and the bulk crystal. The identification of the boundary layer, 600Å thick, has clarified the position with regard to certain anomalous dielectric constant determinations. The dielectric constants for the bulk and boundary regions for single crystal material have been determined as 36 and 33. Dielectric constants for monocrystalline and polycrystalline material, using single frequency techniques, are 25.5 and 22.8, respectively. The monocrystalline dielectric constant difference has been ascribed to non-stoichiometries of between 0.005 and 0.05. The activation energies of the conductivity for the two regions are 0.17eV (boundary) and 0.22eV (bulk).

Low temperature ($T<77K$) capacitance measurements have established the static dielectric constant in the paramagnetic phase ($T>30.8K$) and the antiferromagnetic phase ($T<30.8K$) as 23.8 and 23.6. Thus the phase transition results in a decrease in the dielectric constant of only about 0.8%; the dielectric constant decrease is characterised by a broad temperature range,

37K to 29K.

The electrical properties of the boundary layer have been examined at hydrostatic pressures between 25Kbar and 70Kbar. The pressure dependences of the boundary conductance and dielectric constant are 6.5μSKbar^{-1} and 0.03Kbar^{-1}. These values have been used to estimate the energy ranges of the binding and hopping energies of the carriers.

The high temperature admittance data for single crystal material has established the correct equivalent circuit for four point probe analysis. An Arrhenius plot of the conductance data showed two linear portions above and below a transition temperature of 1275K. The activation energies in these regions (1.4eV and 0.12eV) and the transition temperature correlate well with previously reported data. The equivalent circuit, a parallel combination of conductance and capacitance connected in series with a capacitance, suggests that the previously reported data need not be reassessed.

ACKNOWLEDGEMENTS

I would like to express my gratitude to Professor GA Saunders for his sustained help and enthusiasm. My thanks are also due to Dr's JH Harding, AM Stoneham and EJ Macdonald for their many valuable discussions and their continued interest.

I am indebted to the technical staff and my colleagues of the solid state physics group for their friendly assistance throughout the period of this work.

I am indebted to Dr MT Hutchings of AERE Harwell for supplying and cutting the crystals used in this work, without his assistance none of this would have been possible. I also wish to acknowledge the experimental assistance of Mr J Penfold for allowing the use of the high pressure equipment at STL Harlow and Dr MV Speight, Dr JC Killeen and Mr D Jones for affording me access to the high temperature furnaces of CEGB Berkeley.

For financial assistance I am indebted to the Science and Engineering Research Council and an EMR contract from AERE Harwell.

CHAPTER 1 INTRODUCTION

Uranium dioxide has attracted considerable experimental and theoretical attention primarily because of its use as a fuel for the AGR and PWR designs of nuclear reactor. This has initiated the quest to understand more fully its physical properties; however this work has been rather thwarted by the nature of the material itself. Uranium dioxide is a high melting point (3120K) fluorite structured oxide, with a multivalent cation which allows it to exhibit oxygen excess or deficiency. Electrically it may be described as a Mott insulator, or a poor semiconductor, or a fast ion conductor depending upon the temperature of measurement! Yet, the nuclear power industry wishes to know its thermal conductivity, electrical conductivity and specific heat, in both the solid and liquid phases. Additionally it desires information on its equation of state up to 5000K. In these areas experimental and theoretical work on uranium dioxide have proceded hand-in-hand, as theoretical models need a certain amount of experimental input, and experimental work is often directed by theoretical predictions.

Much theoretical work is underpinned by the correct evaluation of the relevant interatomic potentials, which are reliant upon experimental data. The starting point of the present work was to measure the variation of the static dielectric constant as a function of pressure.

Initial results of this work showed inconsistencies in the dielectric constant values and because of the central position of the dielectric constant in the parameterisation of the interatomic potentials these inconsistencies had to be resolved.

Anomalous behaviour has also been observed in the enthalpy of uranium dioxide; an understanding of its thermal properties is crucial for reactor safety analyses. The anomaly has been variously ascribed either to electronic defects or Frenkel defects. Work on closely related materials, the fluorite halides, has indicated that electrical conductivity measurements can be used as a powerful tool to probe the nature of the defects.

However the initial work on the dieletric constant indicated that the inconsistencies extended to electrical conductivity measurements in the form of an anomalous frequency dependence. The previously accepted data, which had been used to investigate the enthalpy anomaly, indicated no such dependence. Thus it was essential to examine the electrical conductivity thoroughly to establish whether a reassessment of the accepted data was necessary.

In this thesis the construction of an impedance profiling system has been described, along with the methods necessary to apply these techniques to a wide range of physical conditions including high pressures

and both low and high temperatures (chapter 4). The impedance data measured by this system has been analysed using the technique of complex plane representation (chapter 3) to establish the conductivity and dielectric constant of uranium dioxide. The thermophysical data of this analysis (chapter 5) have been discussed with reference to previously reported experimental and theoretical work (chapter 2) on uranium dioxide and other fluorite structured oxides in chapter 6. Chapter 6 also contains some suggestions for further experimental work using the methods outlined in this text.

Chapter 2 THE ELECTRICAL CONDUCTIVITY, DIELECTRIC RESPONSE AND RELATED PROPERTIES OF URANIUM DIOXIDE

Section 2.1 CRYSTAL STRUCTURE

Uranium dioxide crystallizes in the fcc (fluorite) structure (figure 2.1). The fluorite structure can be best viewed as an array of simple cubic cells of side $a_o/2$ of anions (oxygen), with alternate cube centres occupied by cations (uranium). Fluorite is calcium fluoride; the structure is adopted by a number of halides and oxides eg stabilized zirconia, ceria, thoria and strontium chloride.

UO_2 undergoes a first order structural and magnetic phase transition at 30.8K (Jones et al 1952, Arrott and Goldman 1957, Henry 1958, Leask et al 1963, and Frazer et al 1965). This transition is from a high temperature paramagnetic fluorite structure to a low temperature antiferromagnetic tetragonal structure. The phase transition is accompanied by a small shear (0.014Å) of the planes of oxygen atoms (Faber and Lander 1976) and a rather abrupt change in length of about 20 ppm.

Section 2.2 ELECTRICAL CONDUCTIVITY

Section 2.21 ALKALI HALIDES

The high temperature fluorite structured alkaline earth fluorites PbF_2 and $SrCl_2$ have been shown to exhibit fast ion conduction with conductivities (of the

FIGURE 2.1

THE FLUORITE STRUCTURE OF UO_2

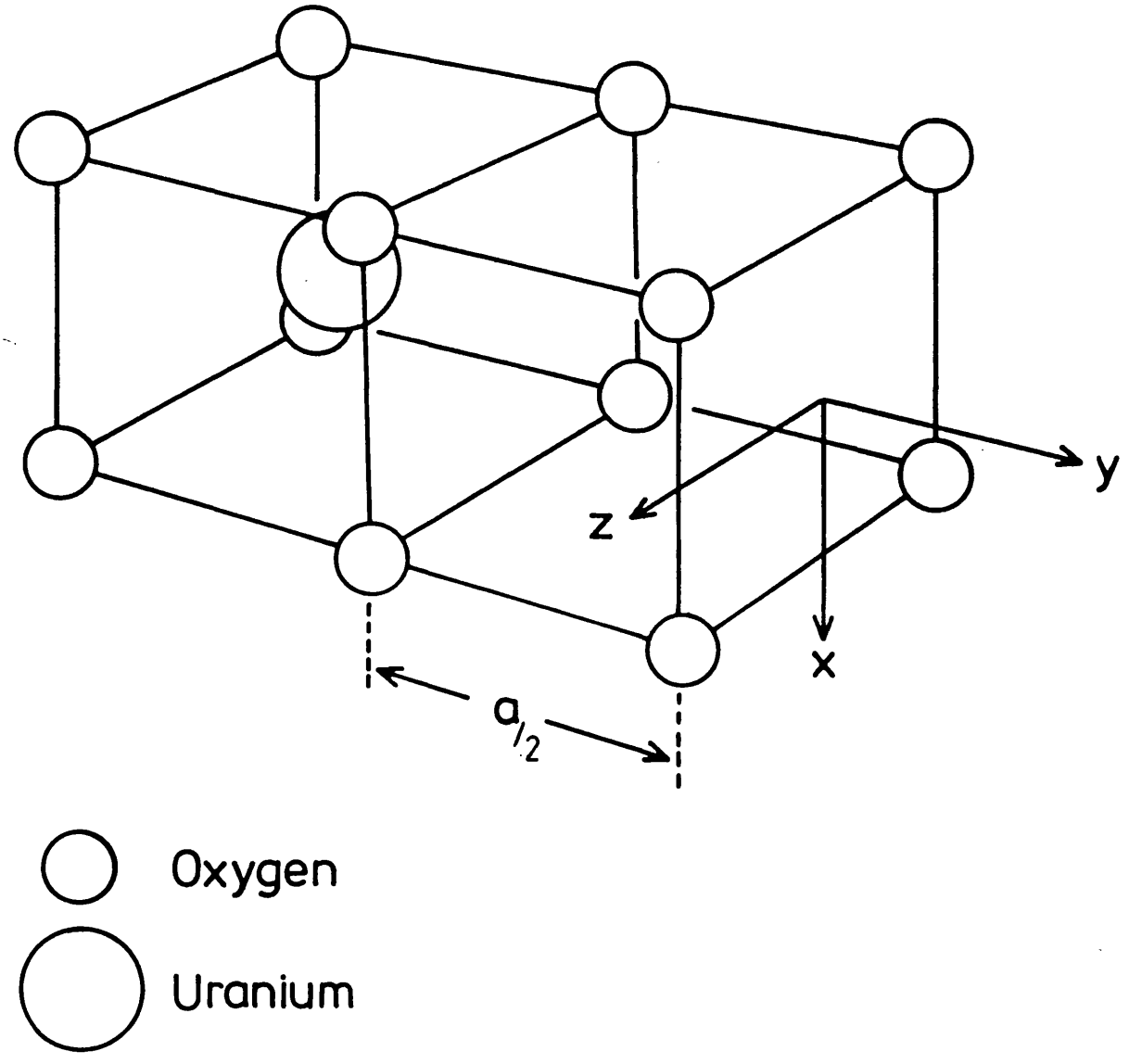

order $1\Omega^{-1}cm^{-1}$) which only increase slightly upon melting, (Derrington and O'Keeffe, 1973, and Derrington et al, 1975). Subsequently a number of other fluorites have been identified as fast ion conductors (Chadwick 1983). At temperatures, T_c, a few hundred degrees below the melting point, T_m, these fluorites exhibit a rapid rise in the ionic conductivity such that above T_c fast ion behaviour is observed (figure 2.2). This rise is accompanied by a broad specific heat anomaly (figure 2.3), discussed elsewhere. The specific heat anomaly and the fast ion conduction have been ascribed to a diffuse transition involving disordering of the anion sublattice. Neutron diffraction studies (Hutchings, 1981) have indicated that a large fraction (about 30%) of anions leave their regular sites in the fast ion phase and form defect clusters. Transport studies and molecular dynamics calculations (reviewed by Chadwick 1983) have indicated that the concentrations of these defects that are mobile above T_c are only a few percent.

The effect of doping fluorites with trivalent impurities has been examined by Catlow et al (1981) and has been found to depress T_c but to increase the conductivity; as an example, data for CaF_2 doped with Er^{3+} are shown in figure 2.4.

SECTION 2.22 FLUORITE OXIDES

The fluorite structured oxide (thoria, ceria and stabilized zirconia) electrolytes have been extensively

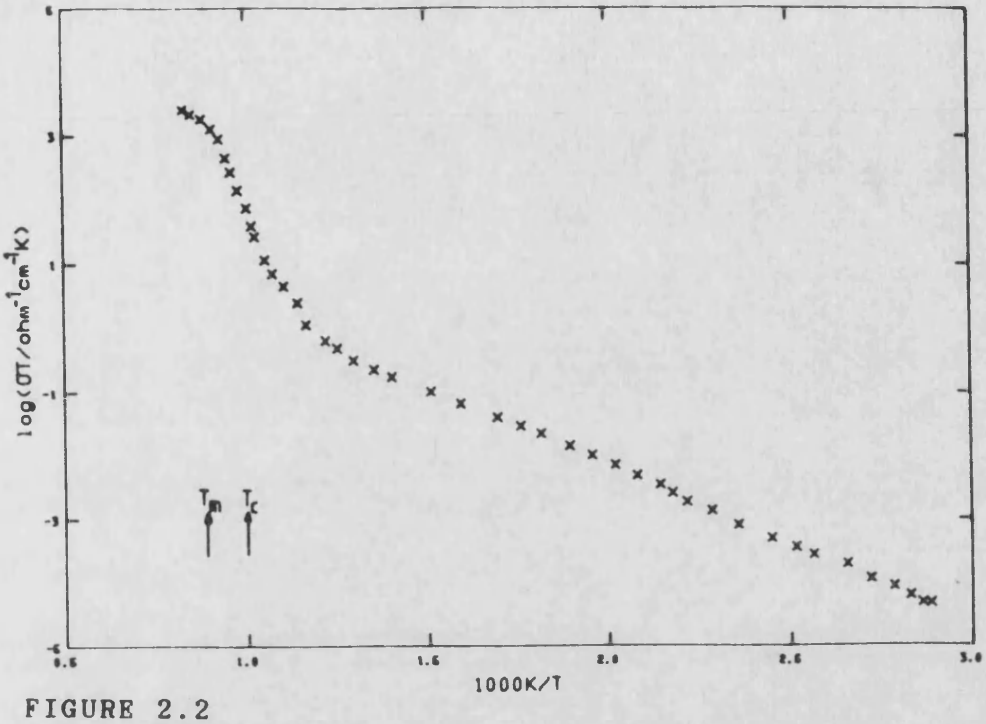

FIGURE 2.2
THE CONDUCTIVITY PLOT FOR NOMINALLY PURE SINGLE CRYSTAL $SrCl_2$, CHADWICK 1983, (T_c INDICATES THE ONSET OF FAST ION CONDUCTION).

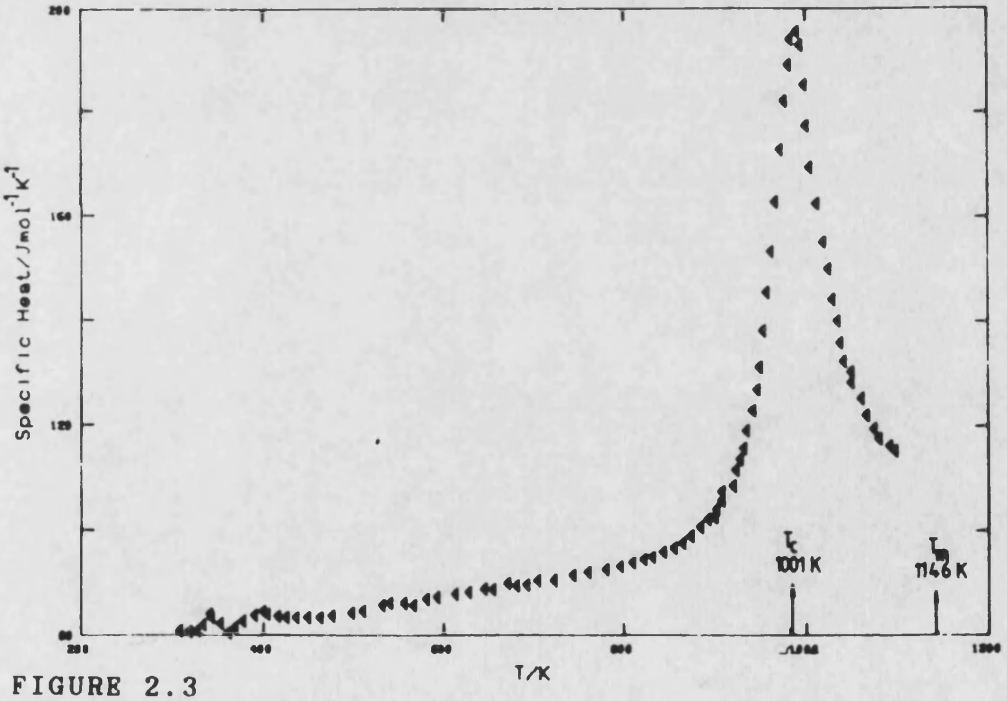

FIGURE 2.3
THE ISOBARIC SPECIFIC HEAT OF $SrCl_2$, CHADWICK 1983.

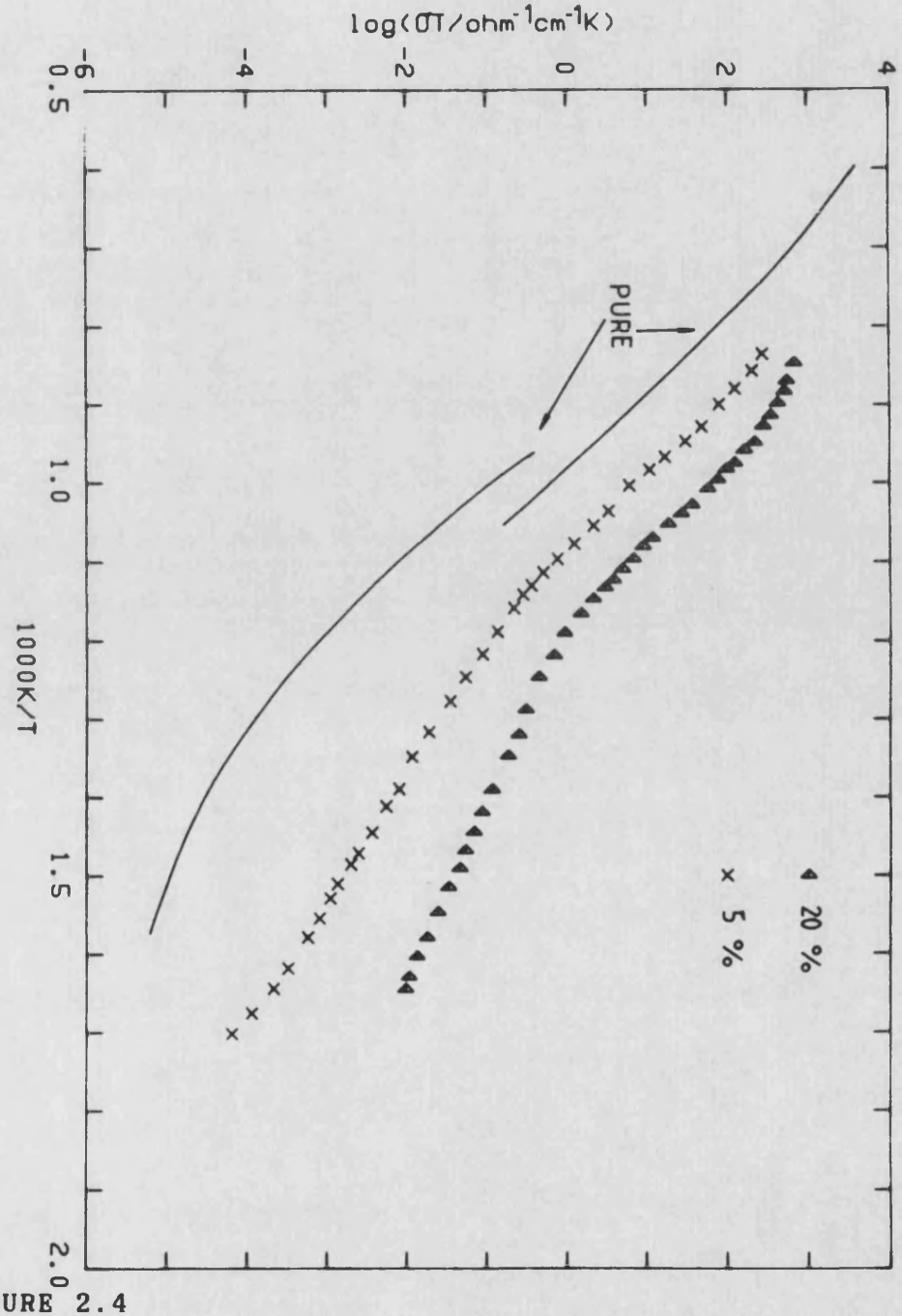

FIGURE 2.4

CONDUCTIVITY PLOTS FOR NOMINALLY PURE (SOLID LINES) AND Er^{3+} DOPED (5% AND 20%) CaF_2, CHADWICK 1983.

studied and found suitable for a wide range of applications (eg high temperature fuel cells and oxygen monitors). The properties of each of these systems, particularily those which are relevant to UO_2 are now discussed separately.

The fluorite structure is adopted by pure zirconia only at temperatures in excess of 2600K; however the fluorite structure can be stabilised at lower temperatures through the formation of solid solutions with CaO, Y_2O_3 or some rare earth oxides (Etsell and Flanges 1970), this material is termed stabilized zirconia. Electrical studies of stabilized zirconia have been reported by a number of workers (Abelard and Baumard (1982), Ikeda et al (1985), Winnubst et al (1984) and Dragoo et al (1984)) who have made extensive use of electrical impedance spectroscopy. The data given by Abelard and Baumard, typical of other reported data, can be represented by a semicircle (which was depressed by 14°) in a complex impedance plot (figure 2.5). The conductivity is thermally activated, although a gradual change of the activation energy, from 1.17eV (high temperature) to 1.33eV (low temperature), is observed. The depression of the semicircles indicates the introduction of frequency dependent conductive processes. The ac electrical conductivity obeys a power law dependence $\sigma(\omega) \propto \omega^n$ with different exponents above (n=0.64) and below (n=0.85) a transition frequency (ω_T).

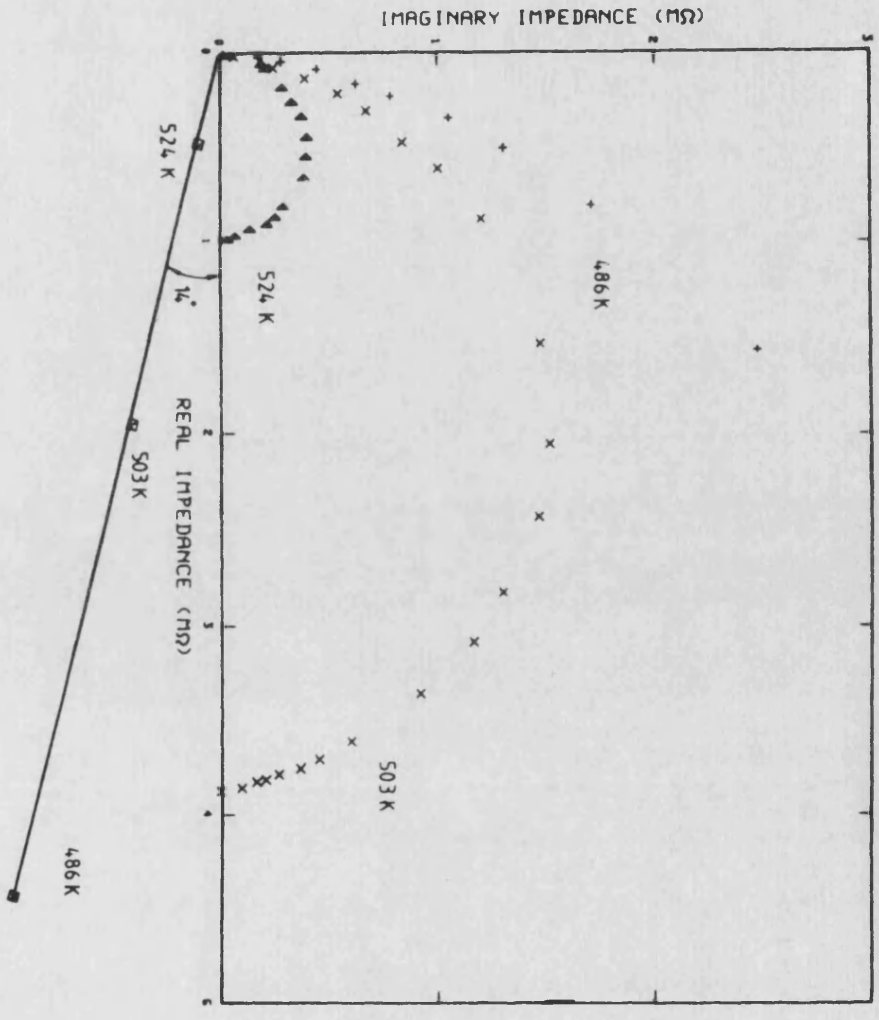

FIGURE 2.5

AC IMPEDANCE PROFILES OF YTTRIA STABILIZED ZIRCONIA, DUE TO ABELARD AND BAUMARD (1982), AT SELECTED TEMPERATURES (◅ 524K, × 503K AND + 486K). THE CENTRES OF THE SEMICIRCULAR ARCS ARE DEPRESSED BY 14°

The transition frequency has been identified as being thermally activated, with the same activation energy as the conductivity. Etsell and Flengas (1970) have noted that increasing the percentage of stabilizing oxide reduces the electrolyte conductivity. Winnubst et al (1984) observed a considerable influence of grain boundaries and impurity levels upon the conductivity of ceramic zirconia: impurities lower the sintering temperature and regulate the grain size. Impedance data for stabilized zirconia obtained by Winnubst et al display an additional impedance arc due to the grain boundary effects. The conductivity of the grain boundaries was found to be, approximately, 2 orders of magnitude lower than the bulk conductivity.

The electrical properties of reduced ceria (CeO_{2-x}) single crystals have been extensively investigated by Tuller and Nowick (1977) using both ac and dc methods. The ac and dc methods gave nearly identical results; consequently grain boundary and electrode effects were assumed to be negligible. The activation energies (figure 2.6) and conductivity prefactors increased with the oxygen deficiency.

Section 2.23 STOICHIOMETRIC URANIUM DIOXIDE

The most comprehensive investigation of the conductivity of stoichiometric UO_2 at high temperatures was that performed by Bates et al (1967). The measurements (figure 2.7) extended from 300K to 3000K,

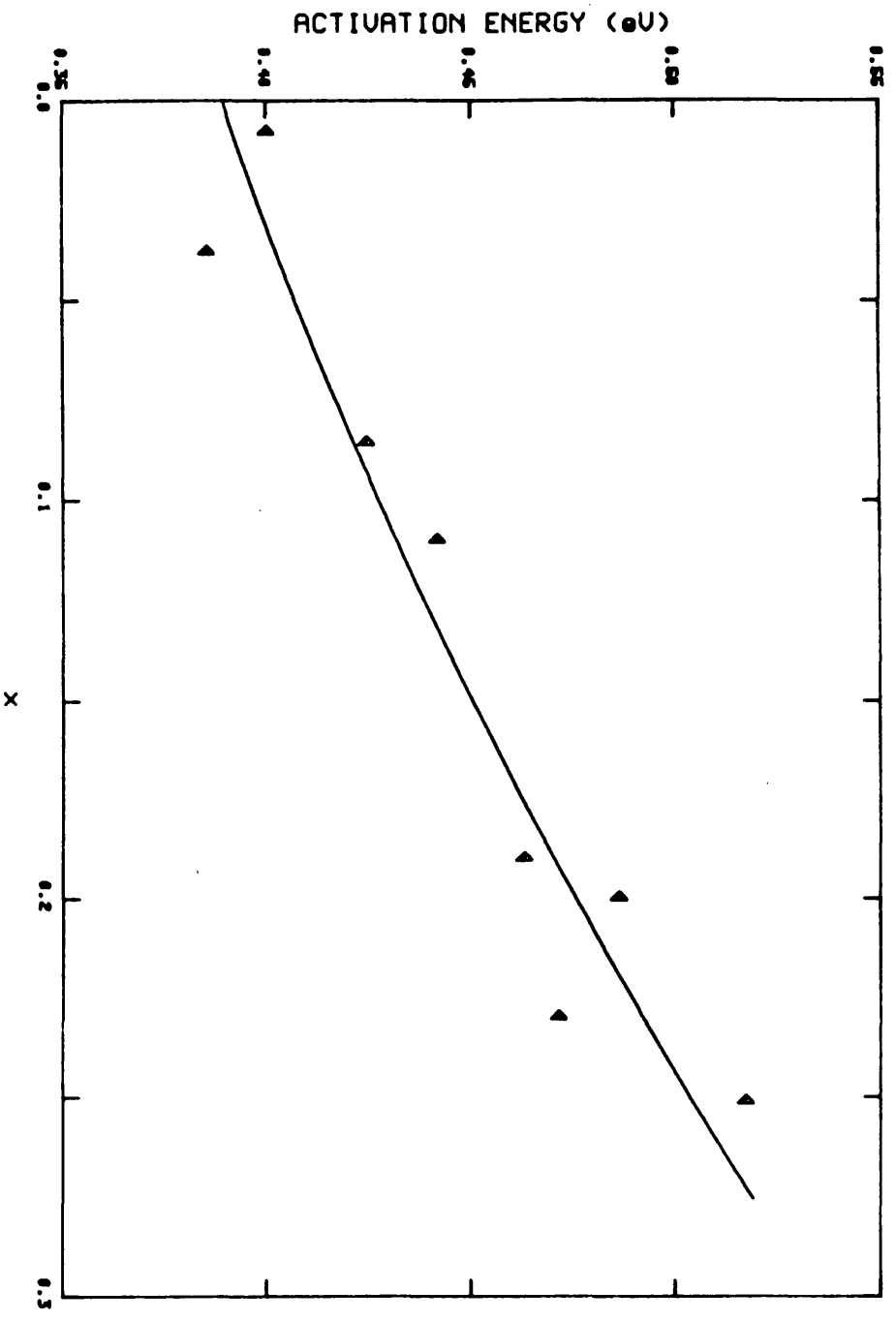

FIGURE 2.6

THE ACTIVATION ENERGY OF REDUCED CERIA AS A FUNCTION OF OXYGEN DEFICIENCY (X IN CeO_{2-x}), DUE TO TULLER AND NOWICK (1977).

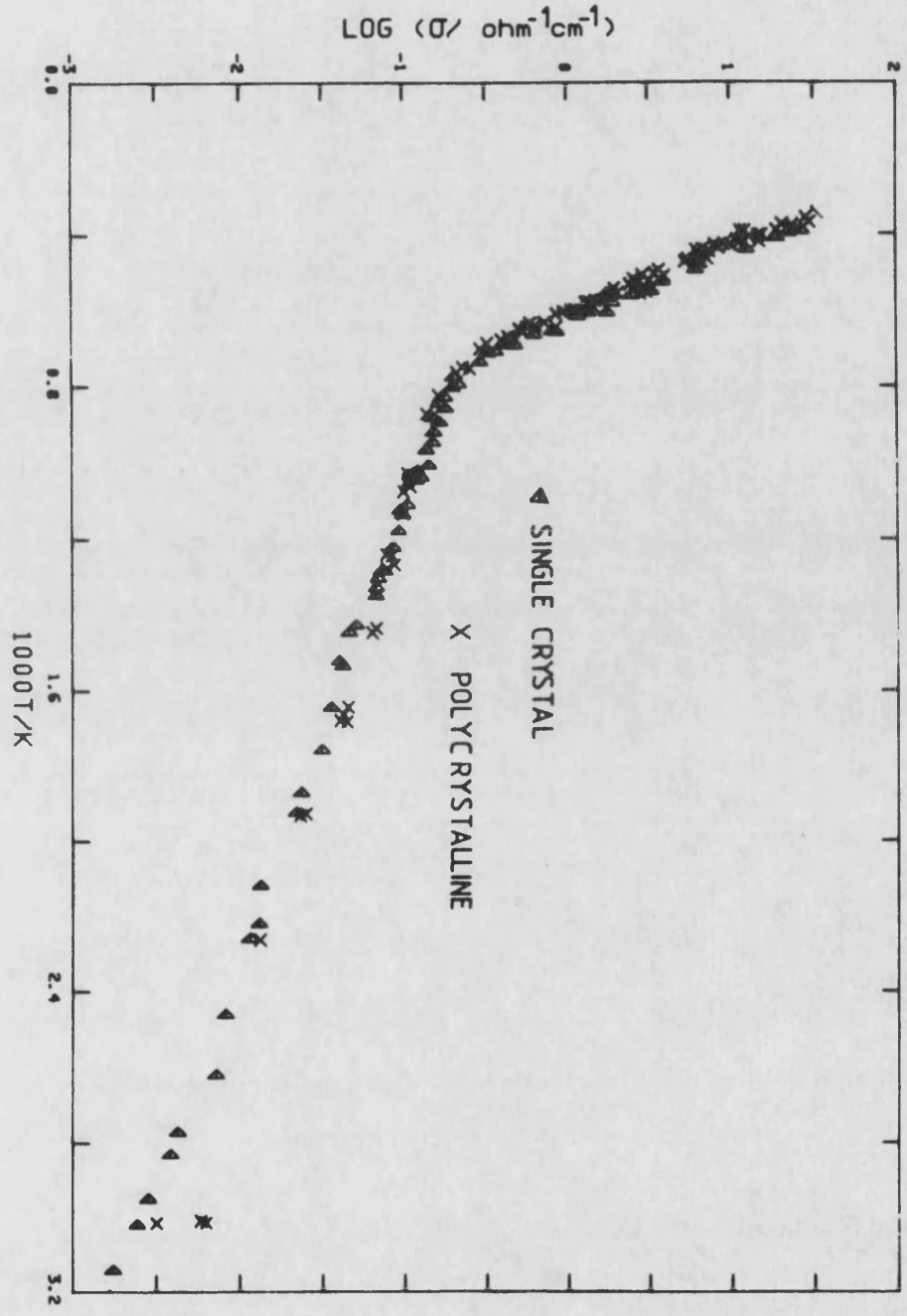

FIGURE 2.7

CONDUCTIVITY PLOTS FOR SINGLE CRYSTAL (◀) AND POLYCRYSTALLINE (X) SAMPLES OF UO_2 USING AC AND DC METHODS (BATES ET AL, 1967). THE AC AND DC DATA ARE INDISTINGUISHABLE AND HAVE NOT BEEN IDENTIFIED SEPARATELY.

encompassing ac and dc, four point probe, methods on both monocrystalline and polycrystalline material. The data was interpreted by the Bates group (subsequently reffered to simply as Bates for convenience) in terms of a process characterised by a thermally activated carrier concentration. The temperature dependence of the conductivity could be fitted by

$$\sigma=\sigma_0 T^{-3/2}\exp(-E_a/kT) \qquad 2.1$$

The conductivity of UO_2 was seen to increase rapidly above 1400K, where it would be adequately described by

$$\sigma=\sigma_0\exp(-E_a/kT) \qquad 2.2$$

where the prefactor σ_0 was equal to $3.57*10^{-3}\Omega^{-1}cm^{-1}$ and the activation energy, E_a was 1.15eV. At these temperatures the exponential temperature term dominated the power dependence of the temperature (ie $2E_a>>kT$), so that the power term could be excluded from the analysis. The activation parameters were established from arrhenius plots of $\log_e\sigma$ versus 1/T. Bates did not find that the expression used by Aronson et al (1961),

$$\sigma=(\sigma_0/T)\exp(-E_a/kT) \qquad 2.3$$

who had analysed his own data in terms of a small polaron mechanism, improved the linearity of the fit. Analysis using this model was found to produce activation energies and prefactors that were increased by approximately 20% (Bates et al 1967).

Bates' data above 1900K showed an enhanced increase (ie in excess of that predicted by equation 2.2) with temperature. He estimated the magnitude of the enhancement and suggested that the conductivity, above 1900K would be more adequately fitted by

$$\sigma = 2.104 * 10^{-2} T^{1.40} \exp(-0.9157/kT) \qquad 2.4$$

This would suggest that the $T^{3/2}$ term for the thermally activated carrier concentration must be included in the high temperature analysis.

Subsequently Bates found that a statistically better fit was obtained the conductivity measured over the complete temperature range using a third order polynomial:

$$\log_e \sigma = 9.646 - 2.078 * 10^4 T^{-1} + 1.231 * 10^7 T^{-2} - 6.484 * 10^9 T^{-3} \qquad 2.5$$

Below 1250K the conductivity was not reproducible: significant changes occured upon thermal cycling. These effects were attributed to stoichiometric changes resulting from the high oxygen content of the reducing atmospheres used in the experimental cell. The conductivity values were also found to vary between samples, though the temperature gradients were essentially the same. The conductivity below 1250K was characterised by an activation energy of 0.17eV; it was not possible to quote a value for the prefactor of the conductivity in this low temperature region.

Other dc investigations over more limited temperature ranges are in substantial agreement with Bates et al, (Willardson 1957, Aronson 1961, Nagels 1963, Myers 1964, Killeen 1980, Munir 1981). Additionally the measurements of Killeen (1980) displayed inconsistencies between the prefactors for monocrystalline and polycrystalline material below 1373K; above this temperature no differences in the prefactors were observed. The analysis of Willardson (1957) showed a range of activation energies, with values of the order 0.30eV below 873K; these scattered values were ascribed to stoichiometry changes taking place during he experiments: this is a plausible explanation in view of the experimental conditions. The work of Myers (1964), Killeen (1980) and Munir (1981) clearly showed two conductivity regions, with enhanced conduction above 1400K. The activation parameters for these data are collected in table 2.1.

The conductivity, measured by Bates for both monocrystalline and polycrystalline material, showed a strong dependence on the measurement frequency (figure 2.8 a) and 2.8 b)); this was most pronounced in polycrystalline material. Bates ascribed the frequency dependence of the conductivity to either resistance effects within the measuring system or surface conduction. Good agreement was noted between dc values and ac values that had been extrapolated to zero

TABLE 2.1 THERMAL ACTIVATION PARAMETERS FOR THE ELECTRICAL CONDUCTIVITY OF UO_2

SOURCE	TEMP RANGE	ACTIVATION ENERGY/eV	PREFACTOR/ $\Omega^{-1}cm^{-1}$
DC MEASUREMENTS			
Aronson*	773-1423	0.30	--------
Nagels*	90-900	0.34	--------
Bates*	<1250	0.22	--------
Bates*	1400-1900	1.4	--------
Bates**	<1250	0.17	--------
Bates**	1400-1900	1.15	$3.569*10^3$
Iida**	<700	0.21	--------
Iida**	700-120	1.25	--------
Myers**	1373-2273	1.30	--------
Killeen**	673-2000	1.07	$2.6*10^3$
Killeen**	<673	0.14	0.9
Munir**	<1600	0.13	1.010
AC MEASUREMENTS			
Lee**	770-1430	0.31	$3*10^3$
Matsui**	1270-1400	0.27	--------
Dudney*	1000-1600	1.4	--------

* parameters calculated from plots of $\log_e \sigma T$ vs 1/T

** parameters calculated from plots of $\log_e \sigma$ vs 1/T

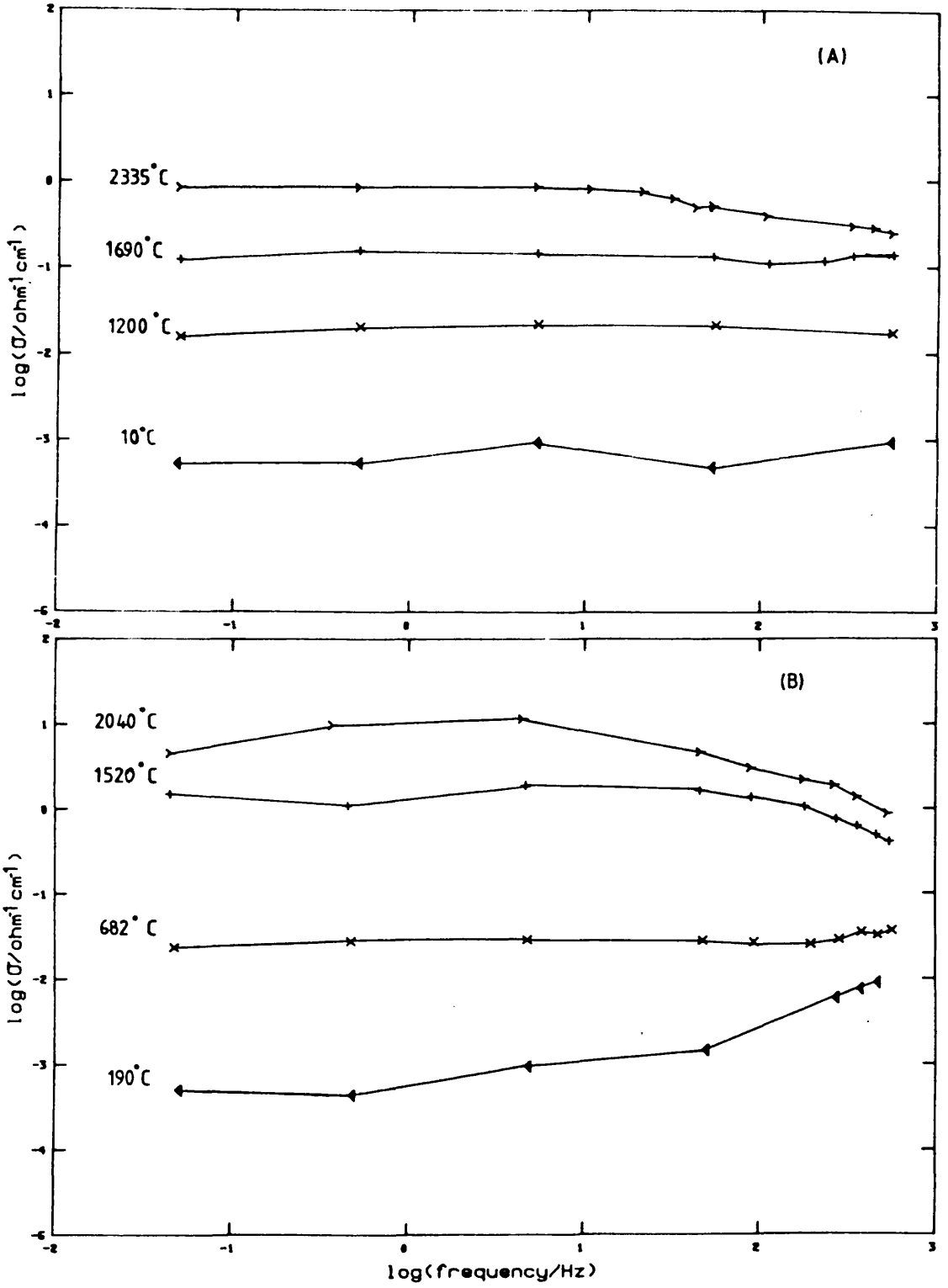

FIGURE 2.8

CONDUCTIVITY AS A FUNCTION OF MEASUREMENT FREQUENCY AT SELECTED TEMPERATURES FOR A) SINGLE CRYSTAL AND B) POLYCRYSTALLINE UO_2 (BATES ET AL 1967).

frequency (figure 2.7). Other workers have also made ac measuements (Gesi and Tateno 1969, Dudney 1981, Tateno 1984, and Matsui 1986) though they reported no dependence upon the measurement frequency. Lee (1975) was the only worker, apart from Bates, to report a dependence at low frequencies of the electrical conductivity, his measurements were accomplished using a capacitance-resistance bridge with a frequency range of 0.5-10KHz. The conductivity was found to vary, though not by more than 10%, across this frequency range. The temperature dependence was in general agreement with that of Bates.

The only reported measurement of the electrical conductivity up to and through the melting point (3120K) was that due to Wright (1981) using a capacitor discharge technique. This entailed examination of the current and voltage profiles of a capacitor discharge through a preheated UO_2 sample (figure 2.9) -so that the sample exhibited fast ion conduction. The discharge current was used to heat the sample and to determine simultaneously its resistance. The experimental data strongly suggested that the conductivity decreased after a finite time (t_d) subsequent to the initiation of the discharge; this time increased when the sample preheat temperature was lowered. The decrease in the conductivity at t_d was ascribed to the melting of the sample. The experimental conditions did not allow for

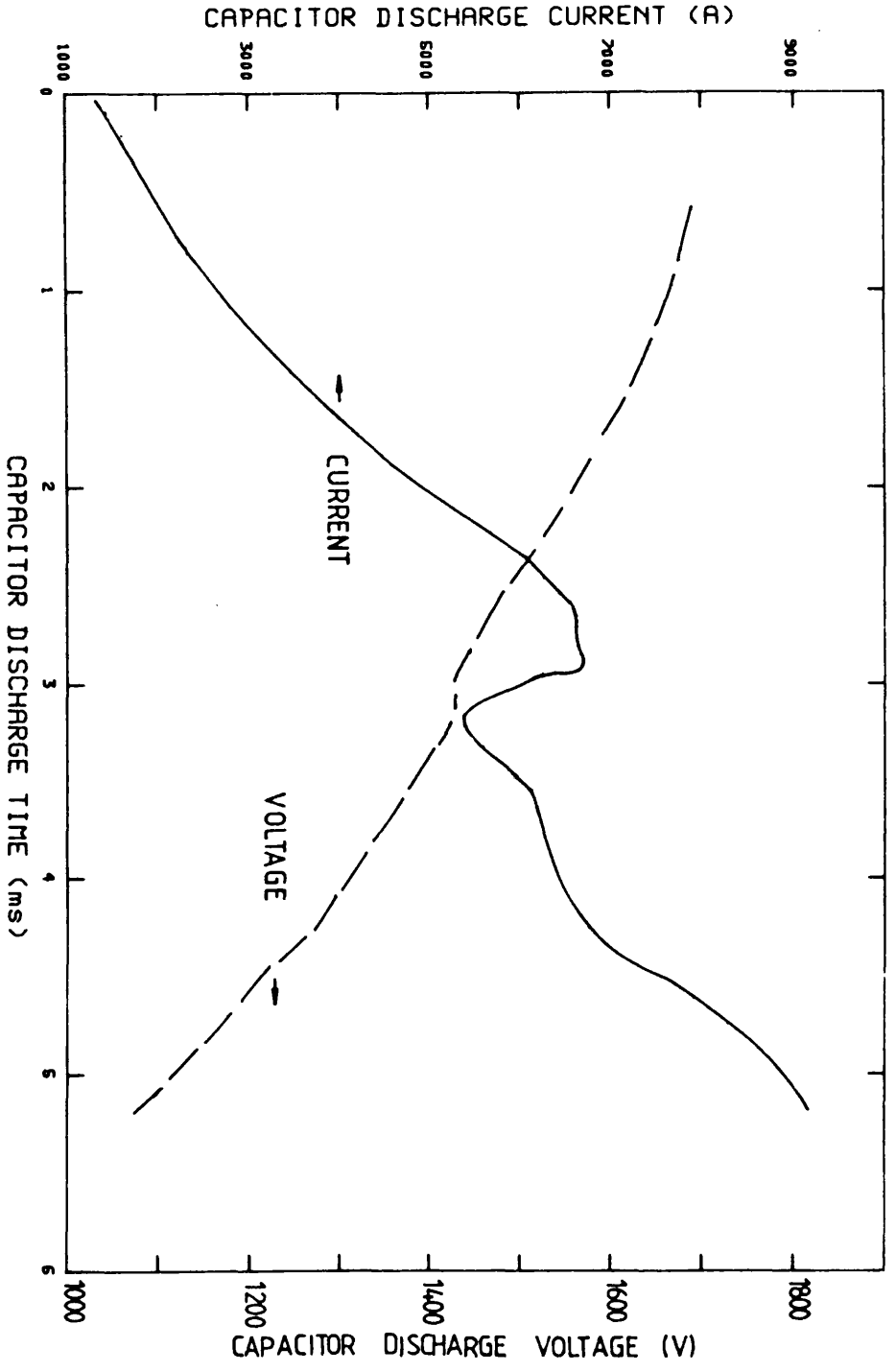

FIGURE 2.9

THE CURRENT AND VOLTAGE AS A FUNCTION OF TIME AFTER INITIATION OF A CAPACITOR DISCHARGE THROUGH A PRE-HEATED POWDER SAMPLE OF UO_2 (WRIGHT ET AL 1981).

this time to be identified unambiguously as that at which melting took place.

Section 2.24 NON-STOICHIOMETRIC URANIUM DIOXIDE

The electrical conductivity of non-stoichiometric UO_2 has been studied by a number of workers using a wide range of experimental techniques. The most comprehensive data have been that published by Aronson et el (1961), Lee (1975) and Tateno (1984); these data were obtained under dc, ac and microwave conditions, respectively.

The work of Aronson and Lee examined the thermally activated conductivity as a function of excess stoichiometry, figures 2.10(a) and 2.10(b) respectively. Qualitatively, the agreement between the data was good; the conductivity was found to increase and the activation energy to decrease with increased positive deviations (x in UO_{2+x}) from stoichiometry. Microwave measurements, due to Tateno (1984), extended the range of non-stoichiometry to the oxide U_4O_9,at 300K (figure 2.11).

Dudney et al (1981) noted that the oxygen partial pressure had a very marked effect upon the conductivity (figure 2.12); the isotherms displayed a characteristic "S" shape, though the increase in conductivity became less pronounced at high oxygen partial pressures. From the work of Peron (1968) and Willis (1963), he concluded that this was due to stoichiometry changes within the

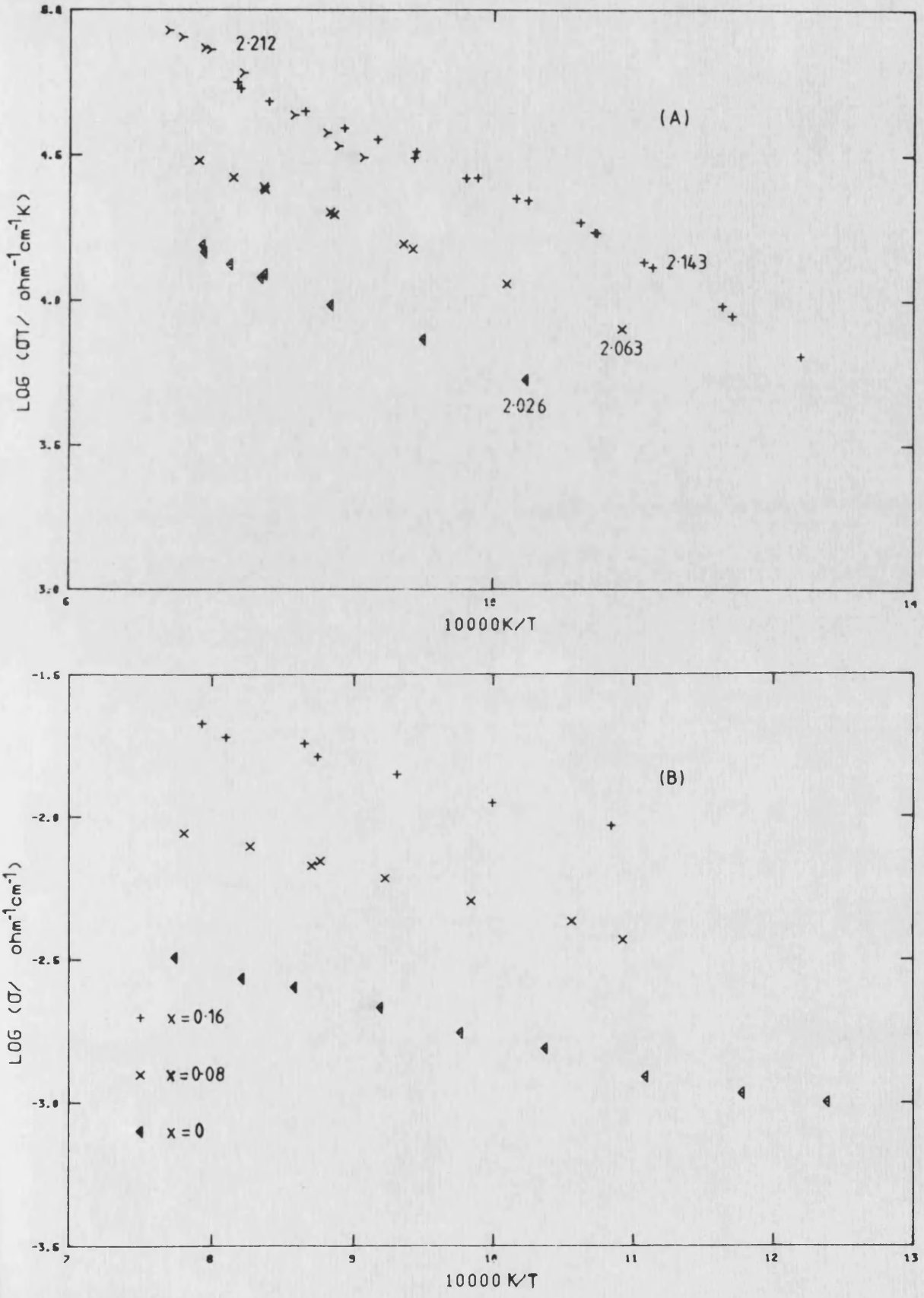

FIGURE 2.10
CONDUCTIVITY PLOTS FOR SINGLE CRYSTAL UO_2 AT SELECTED STOICHIOMETRIES, AFTER A) ARONSON ET AL (1961) AND B) LEE (1975).

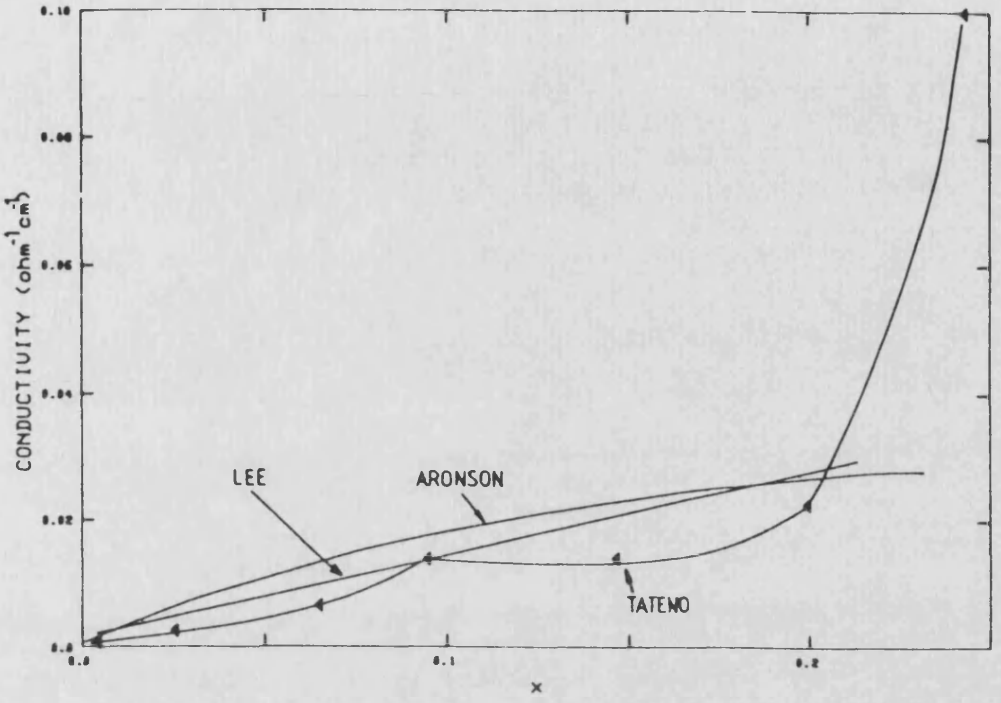

FIGURE 2.11
THE CONDUCTIVITY AS A FUNCTION OF EXCESS OXYGEN (X IN UO_{2+x}) FOR MEASUREMENTS TAKEN AT 9.1GHz, (TATENO 1984), (THE LINE THROUGH THE DATA POINTS SERVES AS A GUIDE TO THE EYE). THE SOLID LINES REPRESENT THE DATA OF ARONSON ET AL (1961) AND LEE (1975).

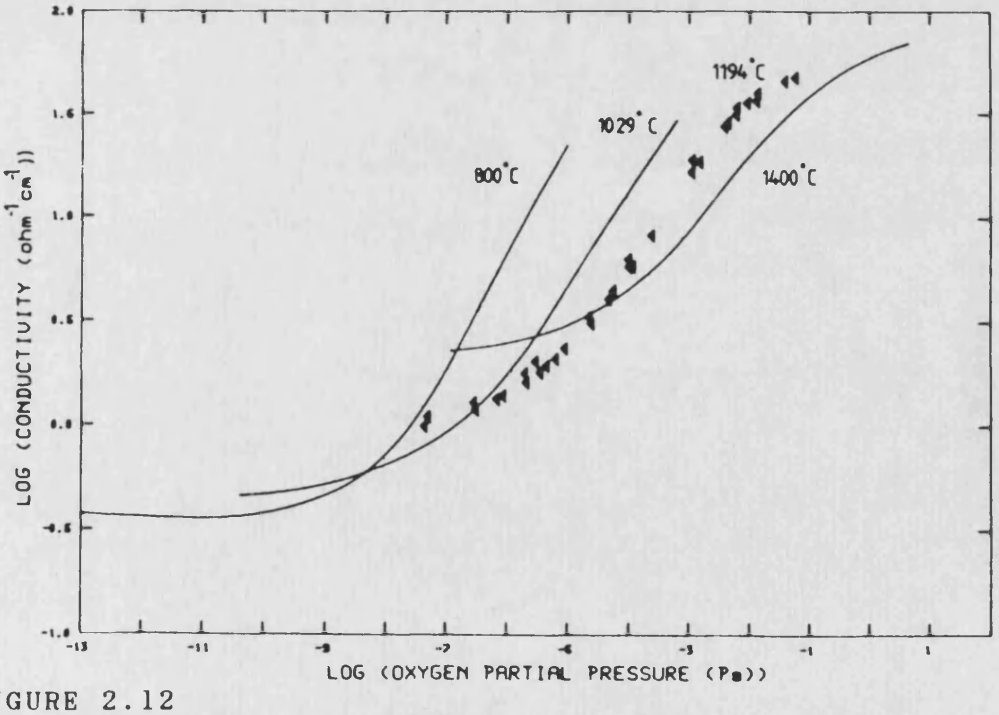

FIGURE 2.12
THE CONDUCTIVITY OF NOMINALLY PURE URANIA AS A FUNCTION OF OXYGEN PARTIAL PRESSURE, AT SELECTED TEMPERATURES (DUDNEY ET AL 1981). THE SOLID LINES REPRESENT THE FITS FOR THE DATA AT THE TEMPERATURES INDICATED.

samples, and that defect clusters of oxygen interstitials and oxygen vacancies were formed in oxygen excess UO_2. Consequently they attributed the measured conductivity to holes, which compensated for the excess oxygen; he concluded that this mechanism would be consistent with the increase of the conductivity with oxygen excess. The data also showed that the dependence of the conductivity upon the oxygen partial pressure, and hence the deviation from stoichiometry, was less pronounced at elevated temperatures. This they attributed to conduction by a separate carrier mechanism which was not dependent upon excess oxygen.

Only one study has been reported (Iida 1965) on the conductivity of oxygen deficient UO_{2-x} where the temperature dependence of the conductivity at selected oxygen defficiencies (table 2.2) was measured using dc techniques.

Section 2.25 DOPED URANIUM DIOXIDE

A number of studies have been caried out on the effects of dopant types and dopant levels on UO_2, the largest study of dopant type has been that conducted by Munir (1981). In this study the conductivity was measured in the temperature range 300K-1600K for the dopants Cr_2O_3, Gd_2O_3, TiO_2, La_2O_3 and Nb_2O_5. Data for pure UO_2 and samples doped with Cr_2O_3 and Gd_2O_3 are shown in figure 2.13. The conductivity increased with the dopant level; the conductivity increase associated with gadolinia doping was the most pronounced

TABLE 2.2 ACTIVATION ENERGIES OF URANIA CRYSTALS HAVING AN OXYGEN TO METAL RATIO OF LESS THAN 2, IN TWO TEMPERATURE REGIONS (IIDA 1965)

O/U RATIO	ACTIVATION ENERGY/eV	
	T<700K	T>700K
2.000	0.210	1.250
1.999	0.179	1.230
1.994	0.432	1.291
1.990	0.119	1.360

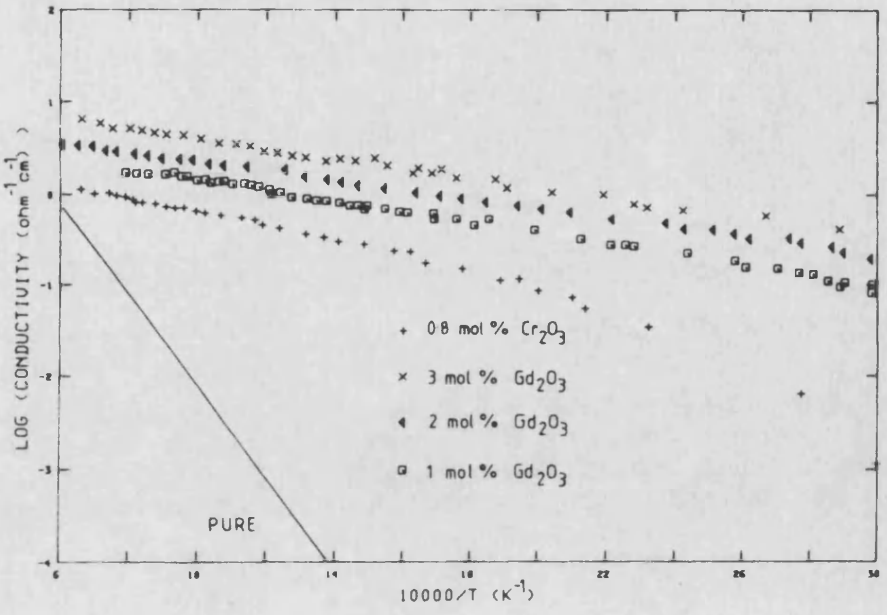

FIGURE 2.13
CONDUCTIVITY OF DOPED UO_2 AT SELECTED DOPANT LEVELS (MUNIR 1981). THE SOLID LINE REPRESENTS DATA FOR NOMINALLY PURE MATERIAL.

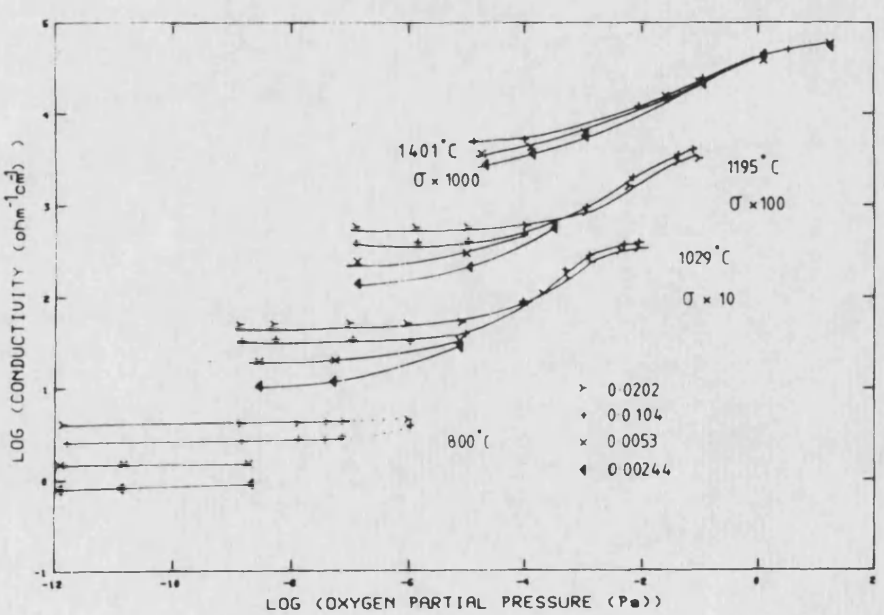

FIGURE 2.14
CONDUCTIVITY OF URANIA versus OXYGEN PARTIAL PRESSURE AT SELECTED TEMPERATURES AND DOPANT (YTTRIA) LEVELS (DUDNEY ET AL 1981). CONDUCTIVITY VALUES AT EACH TEMPERATURE HAVE BEEN OFFSET BY ONE DECADE.

Killeen (1980) examined the electrical conductivity of UO_2 doped with Nb_2O_5 as a function of temperature. His data clearly separated at 750K into two regions; above this temperature the data were characterised by an activation energy of 1.13eV and below 750K the activation energy was 0.12eV. The prefactors for the doped material were significantly larger than those for the undoped materials; this behaviour was attributed to niobium ions localising the holes that were produced by the excess oxygen.

Dudney et al (1981) examined the effect of doping UO_2 with small quantities of yttria as a function of oxygen partial pressure at selected temperatures. For low yttria concentrations the electrical conductivity, at modest oxygen partial pressures, was enhanced (figure 2.14). Increased dopant levels led to the dependence of the conductivity upon the oxygen partial pressure being progressively reduced. This was ascribed to the carrier concentration becoming fixed by the yttria doping, thus allowing the carrier concentration to be determined. The magnitude of the carrier mobilities calculated from this analysis, 0.06 to 0.085 cm^2/Vs, were consistent with small polaron conduction. An Arrhenius plot of the dopant controlled conductivity showed high temperature (dopant independent) and low temperature (dopant dependent) regions, the high temperature region having an activation energy of 1.4eV. This was taken as clear

evidence that the high temperature conduction was due to the intrinsic conductivity of UO_2.

SECTION 2.26 THERMOELECTRIC POWER

Electrical conductivity studies examine the motion of carriers when subjected to an electric field. However carrier motion can also be initiated by the application of a thermal gradient; carrier motion so generated is characterised by the Seebeck coefficient or thermoelectric power (TEP). Charge carriers in a solid are redistributed under the action of a temperature gradient resulting in a thermal emf; the total emf is the sum of three contributing factors:
1) the thermal emf due to the temperature gradient (ΔT), 2) the sum of the contact potentials, 3) the sum of the lead emf's. The magnitude of the third term is normally insignificant when compared to the first, and the second term can be eliminated by careful experimental techniques. For a small temperature difference (ΔT) the TEP (α) is given by

$$\alpha = \Delta V / \Delta T \qquad 2.6$$

where V is the thermal emf. Measurement of the TEP provides useful information about the formation and transport of defects and the sign of the predominant charge carrier. This technique in relation to solid electrolytes, has been reviewed by Shahi (1977).

A thermally activated conductivity can arise from either activation of the carrier concentration or from

activation of the carrier mobility or both. Thermal activation of the TEP results from the activation of the carrier concentration as the TEP only includes terms for the carrier production, thus a temperature independent TEP is indicative of a unactivated carrier concentration. Should both a thermally activated conductivity and an unactivated TEP be established, then the thermal properties can only be ascribed to the mobility term. A thermally activated mobility is characteristic of electrical conduction by small polarons. Tuller and Nowick (1977), Chen et al (1982) and Karim and Aldred (1979) have analysed data on ceria, FeO and $La(Sr)CrO_3$, respectively, using a small polaron model to account for an activated mobility which had been established through TEP measurements. The consequences of a thermally activated conductivity and a thermally activated TEP, when both the mobility and the carrier concentration may be activated, have been discussed by Chen et al (1982).

The thermoelectric power (TEP) of reduced ceria was measured by Tuller and Nowick (1976) at selected stoichiometries (figure 2.15) within a temperature range of 600 to 1100 °C. The data showed that the TEP was temperature independent over the range studied and that it posessed a negative value. The data obtained for the TEP was very sensitive to the sample stoichiometry; this was consistent with data previously obtained for PrO_2

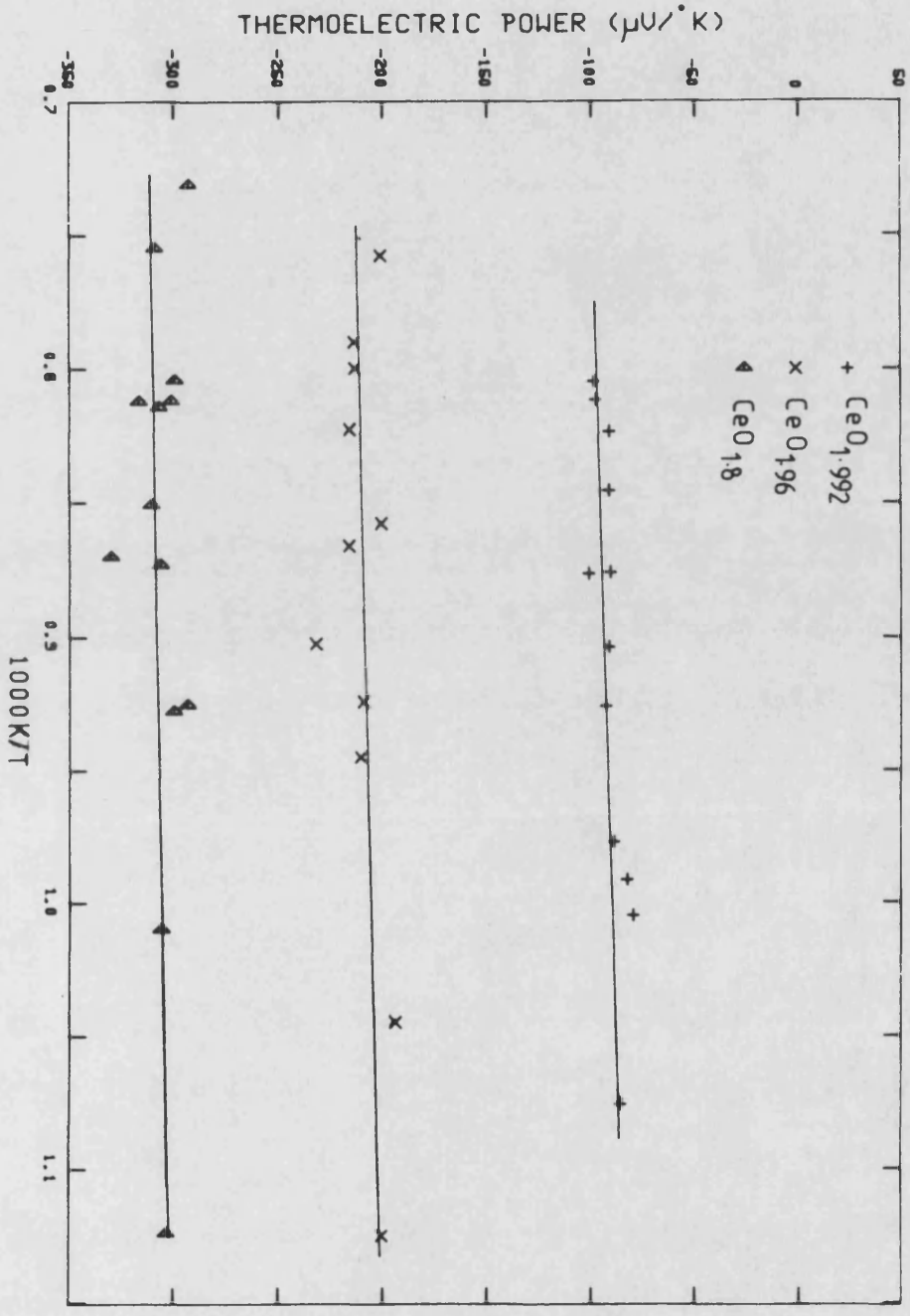

FIGURE 2.15

THERMOELECTRIC POWER OF REDUCED CERIA AS A FUNCTION OF TEMPERATURE AT SELECTED OXYGEN DEFFICIENCIES (TULLER AND NOWICK 1977).

(Honig et al 1960) and ThO_2 (Subba Rao et al 1970). The negative value for the TEP of ceria established that the sign of the predominant charge carrier was negative. Tuller and Nowick also reported data on the electrical conductivity of ceria (section 2.22) which showed the conductivity to be thermally activated: together these indicated an activated mobility.

The temperature dependence of the TEP for UO_2 was examined experimentally for temperatures below 1500K (Killeen 1980). Electrical conductivity data was also examined within an identical temperature range for the same samples. The TEP data (figure 2.16) clearly showed a transition from the p-type to n-type conduction at 1383K for polycrystalline material, with the single crystal material undergoing the transition at a slightly higher temperature. This transition correlated extremely well with the extrinsic-intrinsic transition observed in the conductivity plots (figure 2.8). The TEP saturated at approximately 600μV/°C in the p-type region with the temperature independent region extending over 900°C, for both monocrystalline and polycrystalline material. The polycrystalline material also showed a tendency to a saturated value in the n-type region.

Results for a Nb_2O_5 doped sample showed a clear p-n transition (figure 2.16) at 1053K with saturated values of 200μV/°C and 400μV/°C in both n-type and p-type regions respectively. The TEP in the p-type region was

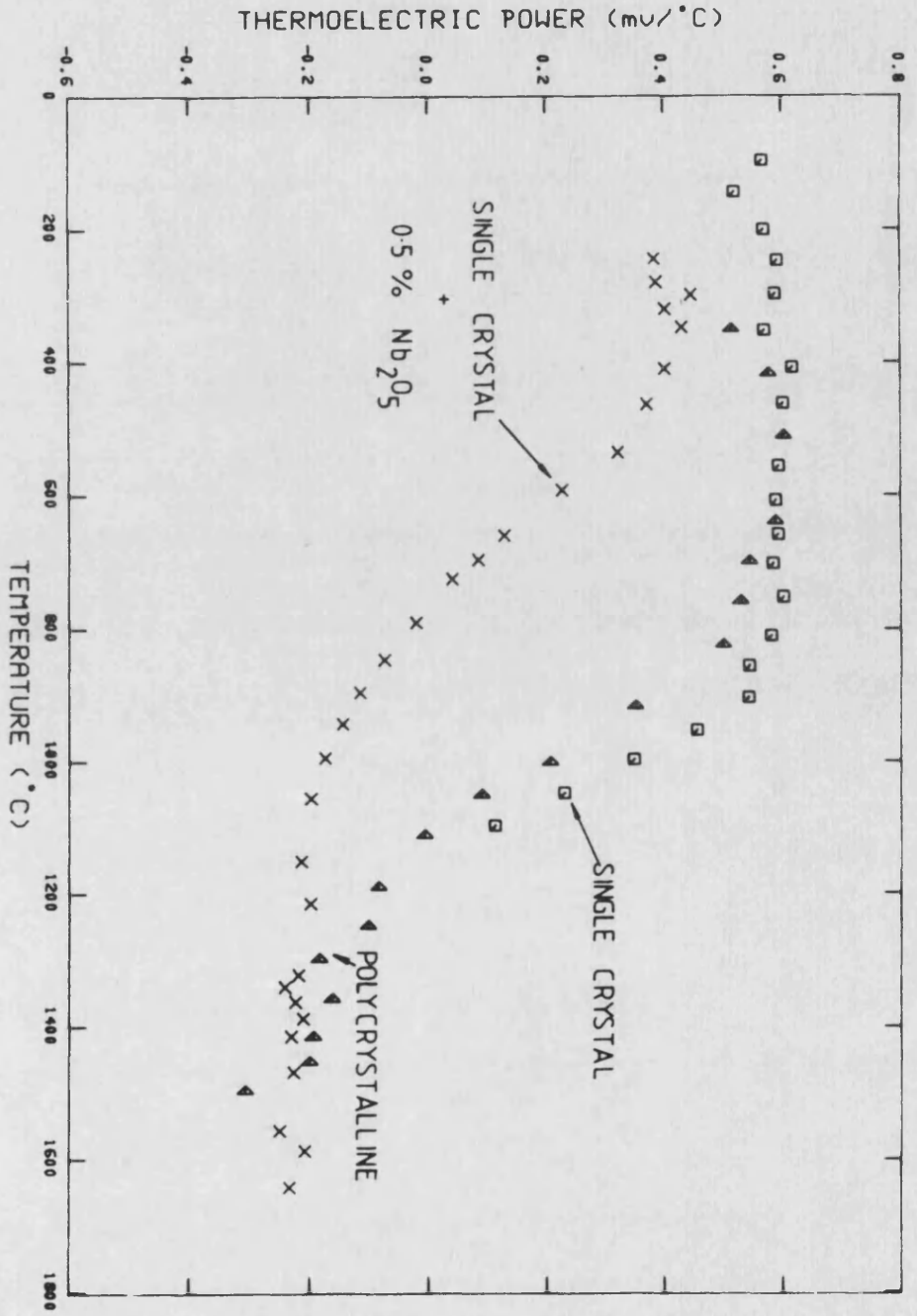

FIGURE 2.16

THERMOELECTRIC POWER OF PURE (□ SINGLE CRYSTAL AND ◁ POLYCRYSTALLINE) AND 0.5% Nb_2O_5 DOPED (X) UO_2 AS A FUNCTION OF TEMPERATURE (KILLEEN 1980).

approximately 30% smaller than in the undoped sample; the transition occured 370K lower than in the pure material.

Section 2.27 CONCLUSION

The electrical conductivity of UO_2 has been ascribed to two conduction mechanisms within the temperature range 300K to 3000K (Hyland and Ralph 1983).

1) At low temperatures (<1400K) the conductivity exhibited a strong dependence upon the sample stoichiometry; it was concluded from this that the conductivity was due to holes compensating for excess oxygen; the sign of the charge carriers was confirmed by the sign of the low temperature thermoelectric power. The temperature independence of the TEP and the low carrier mobility indicated that the charge carriers (holes) formed small polarons and that the conductivity was due to a thermally activated mobility term. The conductivity in this temperature regime (<1400K) was characterised by an activation energy of approximately 0.28eV (arithmetic mean of Table 2.1).

2) Above 1400K the conductivity no longer exhibited a dependence on the stoichiometry. The activation energy for conduction underwent a sharp increase at this temperature and the TEP indicated that this was accompanied by a change in the sign of the predominant charge carrier. The conduction was ascribed to a different mechanism from that operating below 1400K.

Catlow and Lidiard (1974) noted that carriers could be produced by the disruption of the Mott insulating state according to:

$$2U^{4+}(5f)^2 = U^{3+}(5f)^3 + U^{5+}(5f)^1 \qquad 2.7$$

The electrons (U^{3+}) and holes (U^{5+}) so produced would be free to move and contribute to transport phenomena; it has been established that the charge carriers in fact interact with the lattice to form small polaron eigenstates. The activation energy for conduction was approximately 1.4eV.

Generally the whole conductivity data can be decomposed into two components 8using the work of Bates):-

$$\sigma T = A_1 \exp(-0.22eV/kT) + A_2 \exp(-1.4eV/kT) \qquad 2.8$$

Such an approach was suggested by Nagels (1963) and has been used successfully by Oberschmidt and Lazarus (1980) on a number of fluorite structured alkali halides.

Section 2.3 DIELECTRIC PROPERTIES OF UO_2

The dielectric properties of UO_2 have been examined by a number of workers, using various techniques; the methods can be divided into two categories dependent upon the frequencies used. Optical methods (Axe and Pettit 1954, Ackerman et al 1959 and Schoenes 1980) have

been employed to probe the high frequency dielectric constants. Whereas the microwave techniques of Gesi and Tateno (1969) and Tateno (1984) together with the capacitance methods of Briggs (1959), Iida (1965) and Huntley (1966) examined the low frequency dielectric properties.

Schoenes (1980) reported reflectivity measurements, from 0.0025eV to 13eV, together with absorption and Faraday rotation measurements. Kramers-Kronig analysis of the reflectivity data allowed the real and imaginary parts of the dielectric response to be extracted (figure 2.17). The energy gap of 2eV in the imaginary dielectric constant indicated that UO_2 is a semiconductor with a band gap of approximately 2ev. The structures in the dielectric functions at higher energies were used to derive the energy level scheme for UO_2, reported by Schoenes. The reflectivity data of Axe and Pettit (1954) were similar to that of Schoenes, though analysis using the data indicated that the Lydanne-Sachs-Teller (LST) relation

$$\epsilon_{st}/n^2 = (\omega_{LO}/\omega_{TO})^2 \qquad 2.9$$

exhibited a large deviation (12%) when applied to UO_2. Lowndes (1971) noted that the LST relation was well observed by alkaline earth fluorites; Axe and Pettit also reported good agreement for ThO_2 with the LST relation. Schoenes calculated the necessary parameters using his data and compared them with the parameters

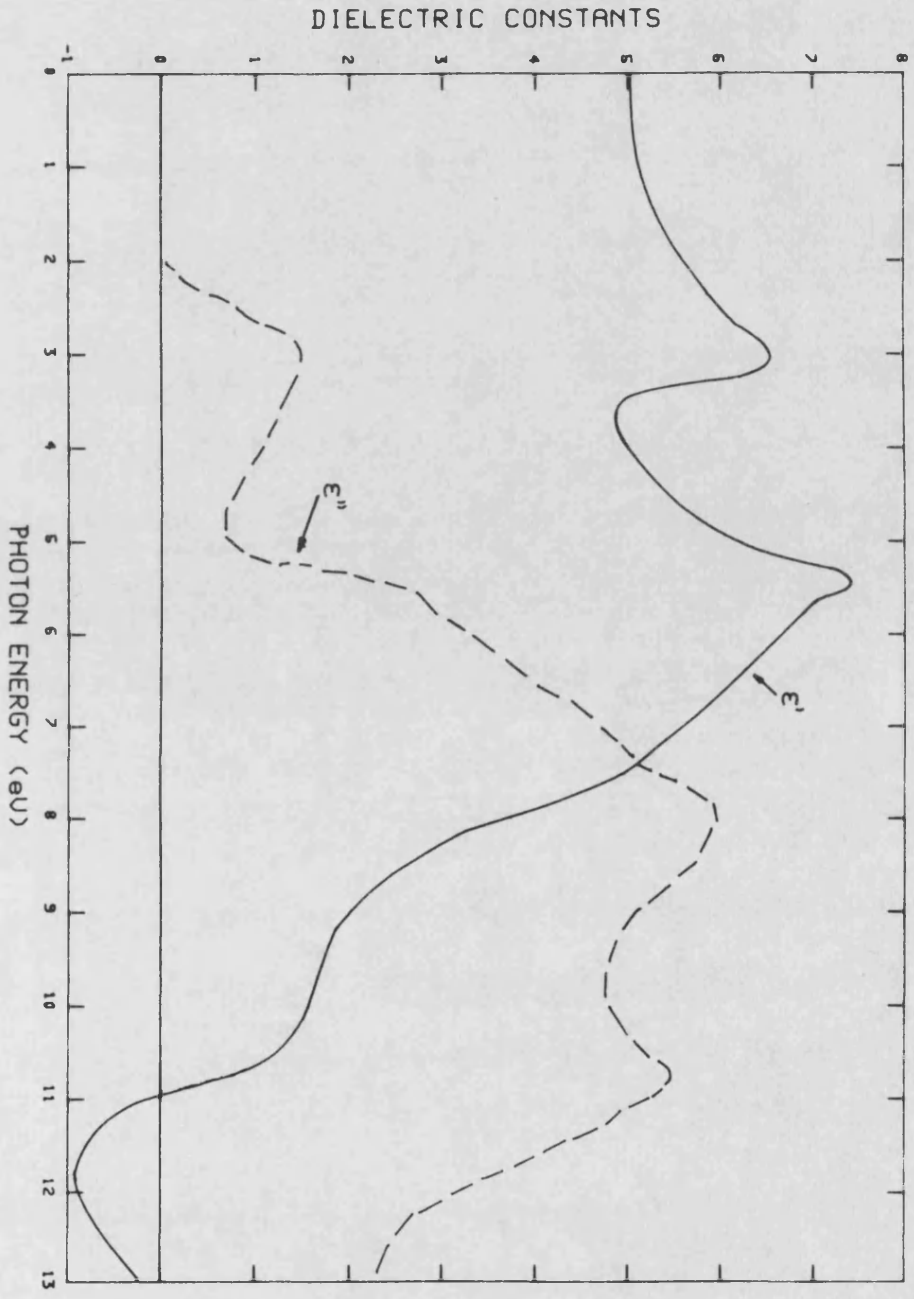

FIGURE 2.17

REAL AND IMAGINARY PARTS OF THE DIELECTRIC CONSTANT OF UO_2 AS A FUNCTION OF PHOTON ENERGY AT 293K (SCHOENES 1980). THE DATA WERE CALCULATED FROM REFLECTIVITY DATA USING THE KRAMERS-KRONIG TRANSFORMATION.

used by Axe and Pettit (table 2.3). The transverse optical frequencies were in good agreement though the longitudinal optic frequency of Axe and Pettit was too small; also the static dielectric constant used by Axe and Pettit was too large. Taking these discrepancies into account, Schoenes concluded that the LST relation is in fact well obeyed in UO_2.

Briggs (1959) obtained a value of 23.6±1 for the static dielectric constant of UO_2 (used by Axe and Pettit in their LST analysis) from Q meter measurements (at a frequency of 178KHz) of the capacitance of single crystal material. This result was an average of a number of readings over a number of samples. Briggs also attempted to measure the dielectric constant of polycrystalline material, but he was unable to obtain consistent values. A similar, capacitative, technique was used in two other determinations (Iida 1965, Axe and Pettit 1966). Iida measured the capacitance of single crystal discs over the frequency range 100Hz to 1MHz and obtained the values 165 and 36 for the static and high frequency dielectric constant, respectively! Axe and Pettit tried, without success, to obtain a value for the static constant, and ascribed the lack of meaningful data to high electrical conductivity.

Microwave techniques were used by Gesi and Tateno (1969) to measure the low temperature temperature dependence of the real and imaginary dielectric

TABLE 2.3 THE PARAMETERS USED BY SCHOENES (1980) AND AXE AND PETTIT (1966) TO VALIDATE THE L.S.T. RELATION FOR UO_2

QUANTITY	SCHOENES	AXE AND PETTIT
ω_{TO} cm^{-1}	280±2	278±2
ω_{LO} cm^{-1}	578±2	556±4
ϵ_{st}	21.5±1	24
n^2	5±0.05	5.3
ϵ_{st}/n^2	4.30	4.53
$(\omega_{LO}/\omega_{TO})^2$	4.26	4.00

constants. These were found to be essentially temperature independent, with the static (real) dielectric constant being 21±1, at 300K. This result was supported by the further microwave work of Tateno (1984).

Huntley (1966) measured the electrical admittance of UO_2 discs (20mm diameter * 5mm thick) at frequencies between 15KHz and 500KHz to assess the static dielectric constant as a function of porosity (figure 2.18). However the O/U ratio of the samples used varied from 2.007 (porosity of 2.5%) to 2.11 (porosity of 40%), so that the data included the combined effects of porosity and non-stoichiometry. The value of capacitance measured, at 293K and low frequencies, yielded an apparent dielectric constant that was three orders of magnitude larger than would be expected; Huntley attributed this to the structure of the material. Increasing the measurement frequency caused the capacitance values to undergo a transition from anonalously high values (at low frequencies) to low, frequency independent, values (at high frequencies). Huntley observed that in UO_2 the transition frequency could be lowered by increasing the sample resistance, this was achieved by cooling the sample with liquid nitrogen where frequency independent capacitances were measured for the whole of the frequency range available. Data obtained in this way allowed the assessment of the

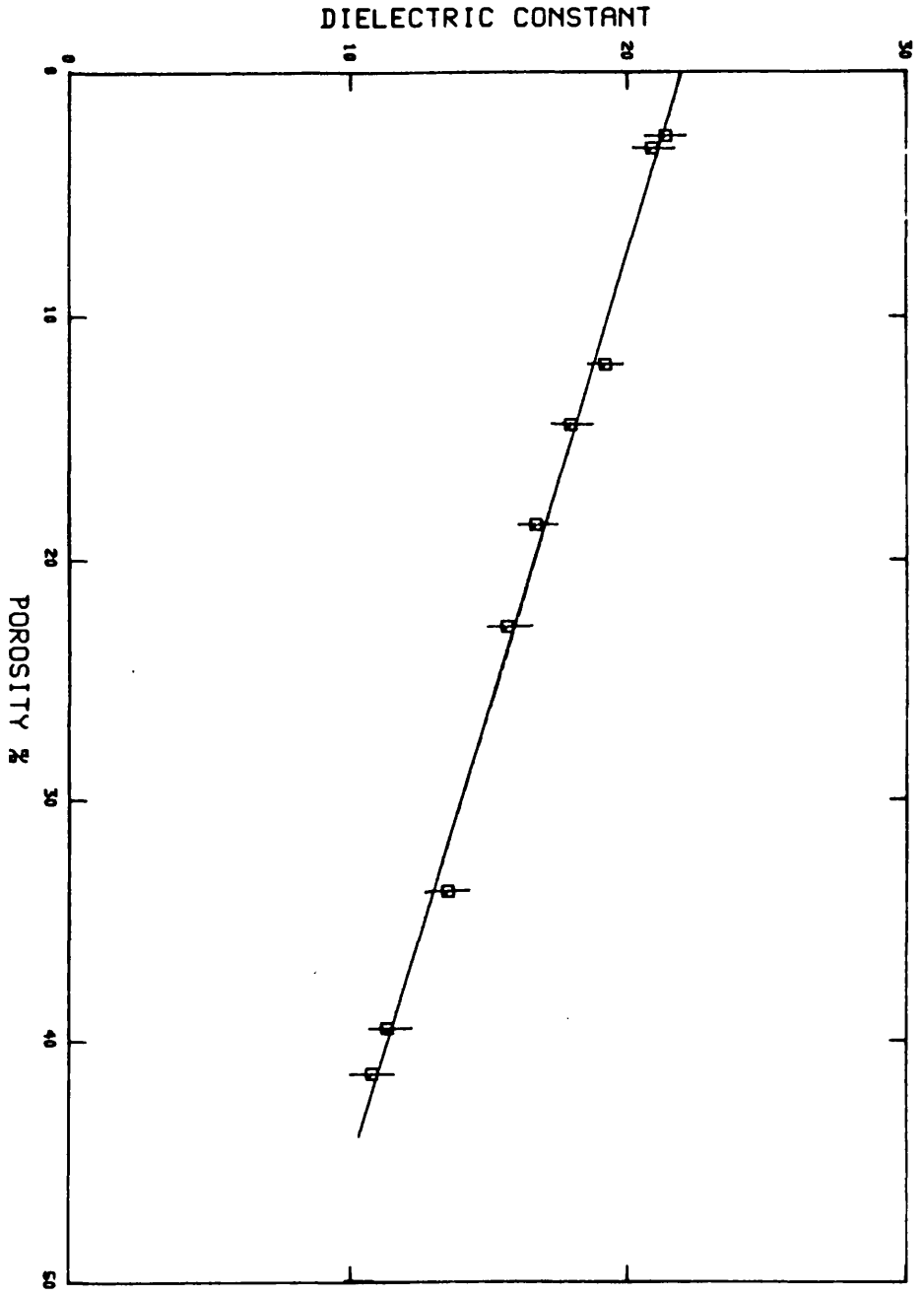

FIGURE 2.18

THE REAL STATIC DIELECTRIC CONSTANT OF URANIA AS A FUNCTION OF POROSITY AT 78K (HUNTLEY 1966). THE STOICHIOMETRY WAS NOT HELD CONSTANT THROUGHOUT THE RANGE OF POROSITIES

static dielectric constant as 21.7±0.5 at 78K for stoichiometric material of zero porosity.

Tateno (1984) conducted microwave studies over a range of stoichiometries and obtained values for the real and imaginary parts of the dielectric constant. The microwave technique allowed measurements to be taken well within the, high frequency, frequency independent regime reported by Huntley, without having to resort to cooling the sample. Both of the dielectric constants (figure 2.19) showed significant increases with increased nonstoichiometry.

A synopsis of the published dielectric constants is given in table 2.4.

Section 2.4 ENTHALPY AND HEAT CAPACITY

In common with other fluorites (section 2.21) there has been considerable interest in determining the heat capacity of UO_2 in the region of it's melting point. However the direct evaluation of heat capacities, especially above 2000K, has been plagued by the practical difficulties of thermal isolation and accurate temperature measurement. Consequently the heat capacity curves have been derived from fits of the enthalpy, as a function of temperature, the enthalpy being experimentally a more accessible quantity. Enthalpies for UO_2 have normally been measured using drop calorimetry techniques. Heat capacity curves for UO_2

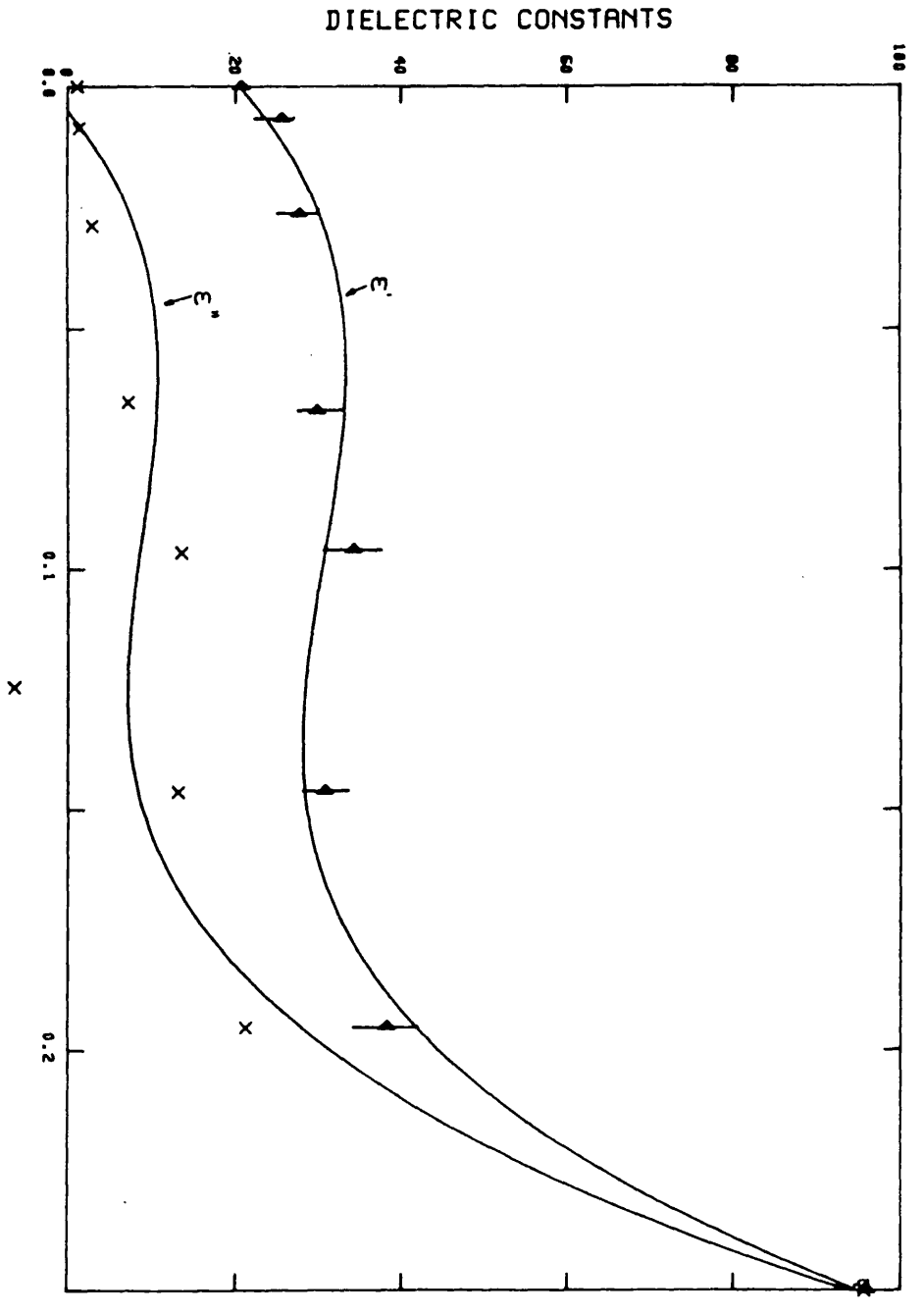

FIGURE 2.19

REAL AND IMAGINARY STATIC DIELECTRIC CONSTANTS OF URANIA, AT 293K, FOR SELECTED STOICHIOMETRIES, X IN UO_{2+x}, (TATENO 1984). THE SOLID LINES SERVE AS A GUIDE TO THE EYE.

TABLE 2.4 PUBLISHED VALUES OF THE DIELECTRIC CONSTANTS OF UO_2. ALL VALUES QUOTED AT 293K UNLESS OTHERWISE INDICATED.

SOURCE		STATIC DIELECTRIC CONSTANT	OPTIC DIELECTRIC CONSTANT
Ackermann	1959	------	5.3
Briggs	1964	23.6±1	-----
Woods	1964	20.4±1.5	-----
Iida	1965	165	36
Huntley*	1966	21.7±0.5	-----
Axe and Pettit	1966	21.3	5.51
Schoenes	1980	21.5	5
Tateno	1984	21	-----

* value obtained at 78K

have been derived from the enthalpy data by Szwarc (1969) and Kerrisk and Clifton (1972). Both analyses indicated that the heat capacity curves behaved like those of a traditional solid below 1400K, but above this temperature the heat capacity increased rapidly. This rise was interpreted by postulating the formation of oxygen Frenkel defects, which had been shown to exist in fluorite halides at elevated temperatures (section 2.21). The resulting heat capacity curves (figure 2.20) showed an exponential rise above 1500K; the defect formation energies obtained were 3.10 eV (Szwarc 1969) and 3.28 eV (Kerrisk and Clifton 1972). Bredig (1972) noted that the enthalpy analysis of Szwarc showed a linear temperature dependence (signifying a constant heat capacity) above 2700K and that deviations from the fitted curve showed a systematic trend about this temperature. This he interpreted as a cooperative lambda type transition at 2670K, similar to that observed in the fluorite halides (figure 2.3). Rand et al (1978) observed similar non-random deviations in the analysis of Kerrisk and Clifton -this supported Bredig's claim. Analysis of the enthalpy data of ThO_2 (Fischer et al, 1981) failed to identify an exponential thermally activated contribution in ThO_2, though further analysis (Fink et al, 1981) showed evidence of a transition at higher temperatures for both oxides (figure 2.20): T_c=2670K in UO_2 and 2950K in ThO_2.

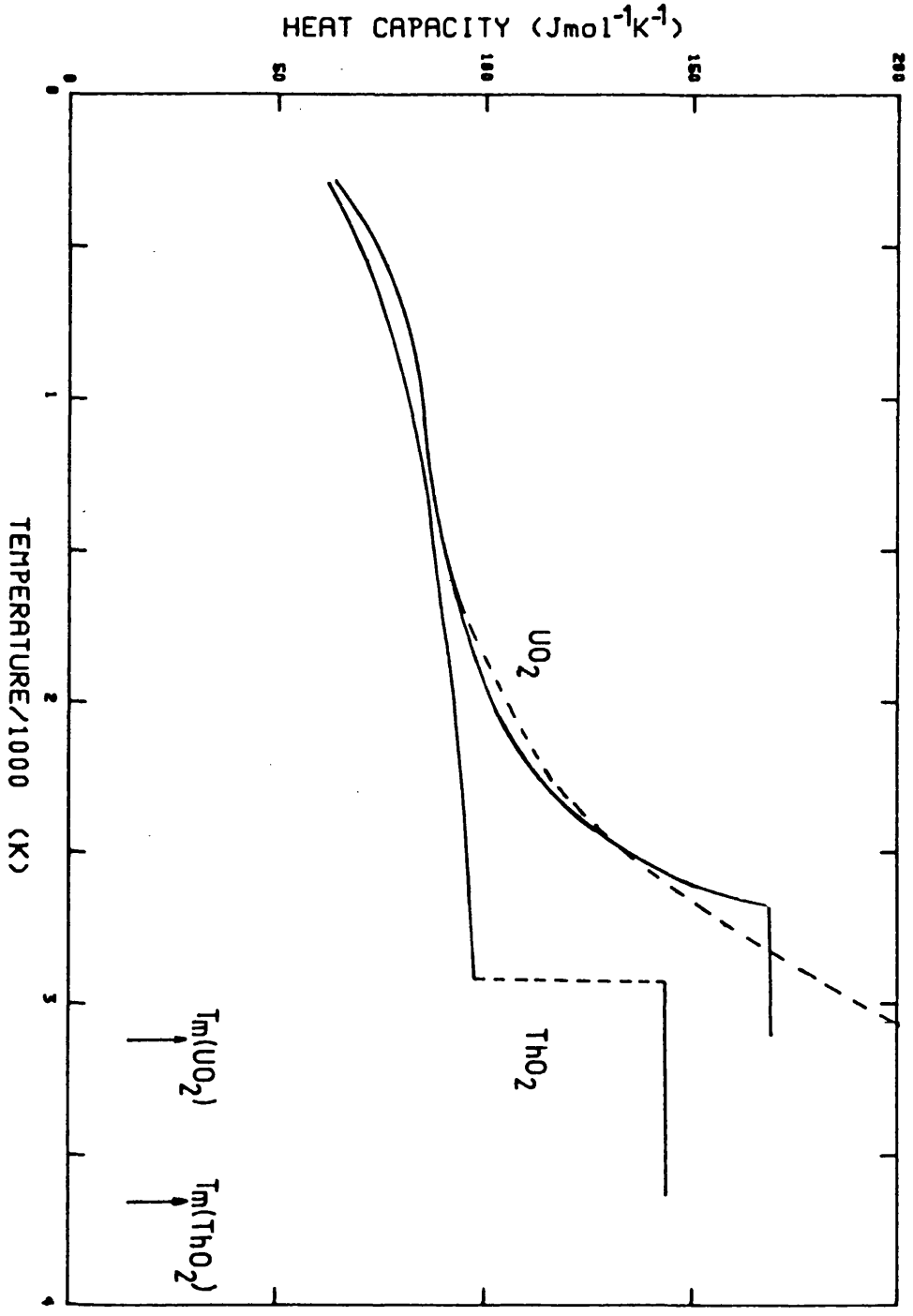

FIGURE 2.20

SPECIFIC HEATS OF URANIA AND THORIA CALCULATED FROM ENTHALPY DATA. SOLID LINES REPRESENT THE ANALYSIS OF FINK ET AL, 1981 (URANIA) AND FISCHER ET AL, 1981 (THORIA), WHILST THE BROKEN LINES REPRESENT THE ANALYSIS OF KERRISK AND CLIFTON, 1972.

MacInnes (1978, 1979) challenged the Frenkel defect model when he noted that the anomaly in UO_2 occurred at a lower fraction of the melting temperature than in other fluorite halides and that there was no evidence of similar, exponential, behaviour in ThO_2. MacInnes concluded that the disorder giving rise to the anomalous enthalpy above 1500K in urania, but not in thoria, was electronic in nature: thoria exhibits a single oxidation state whereas urania has a multiplicity of possible oxidation states. Further support for this approach has been obtained from calculations of the activation energies (table 2.5) for Frenkel defects and electronic disorder by Catlow (1977) and Harding et al (1980). The calculated values for electronic disorder were in better agreement with experimental values than values for Frenkel defect formation.

The contributions due to lattice vibrations, crystal field excitations and small polarons were estimated by Browning (1981); these have been shown to adequately account for the enthalpy data up to 2500K. However, above this temperature an unexplained increase was identified, possibly due to Frenkel defects. A similar theoretical approach was adopted by Hyland and Ralph (1983), where all of the existing transport and specific heat data on solid urania were analysed empirically. This analysis was carried out within the context of the high temperature conduction mechanism outlined in

TABLE 2.5 COMPARISON OF EXPERIMENTALLY DETERMINED ACTIVATION ENERGIES FOR UO_2 WITH VALUES CALCULATED FROM MODELS FOR FRENKEL DEFECT FORMATION AND FOR SMALL POLARON EXCITATION

REFERENCE	QUANTITY	E_a/eV
EXPERIMENTAL		
Bates et al (1967)	conductivity	1.15
Szwarc (1969)	enthalpy	1.55
Kerrisk and Clifton (1972)	enthalpy	1.64
Fink et al (1981)	enthalpy	1.88
CALCULATION		
Catlow (1977)	frenkel defect	2.7
Harding et al (1980)	frenkel defect	2.6
Catlow (1977)	small polaron	2
Harding et al (1980)	small polaron	1.7

section 2.27 1). The effects above 2500K were unaccounted for, though the analysis well represented the data below this temperature.

Neutron diffraction data, due to Clausen et al (1983, 1984), showed no direct evidence of Frenkel disorder below 2400K, whereas Frenkel defects were observed above this temperature. Macdonald (1984) reported that no evidence of electronic disorder was seen up to 2900K in UO_2, however this study used neutron diffraction techniques which could only, indirectly, probe for electronic disorder.

Section 2.5 THEORETICAL CALCULATIONS

In view of the difficulties that have been frequently found (section 2.4) in experimental studies of UO_2, particularly under the extreme conditions that are most frequently of interest to reactor technology, there has been a trend towards theoretical studies. There have been several investigations of the interatomic potential model for UO_2 (Catlow and Lidiard 1974, Catlow 1977 and 1978 and Jackson et al 1983) which have allowed calculation of many lattice properties. Indeed many of the potentials commonly used for ionic solids have been collated in one volume for easy use and reference (Stoneham 1981). In this section only a very brief outline of the techniques and potentials used will be

given, relevant results are detailed elsewhere in the text.

The potential between the ions, which are initially taken as point charges, is modelled by considering three interactions:-

1) Coulombic attraction - long range

2) van der Waals attraction - short range

3) short range repulsion - short range

The second and third terms are generally represented by:-

$$U=U_2+U_3=A\ \exp(B/r)\ -C/r^6 \qquad 2.10$$

The parameters A, B and C are determined either empirically from experimental data or directly from Hartree Fock calculations. It is more normal, where experimental data exists, to use the empirical approach.

The standard method is now to simulate the fluorite structure and allow the lattice to relax (at this stage "best guess" values are used for the potential parameters A, B and C). After this relaxation the internal energy is calculated (from the components 1), 2) and 3)), and other thermodynamic quantities are determined from the internal energy. The effects of external pressure or temperature are simulated by altering the lattice parameter. At this point a number of experimentally measurable quantities are calculated (eg dielectric constants, elastic constants and lattice parameter) and compared with experimental values. The

potential parameters (A, B and C) are adjusted iteratively to ensure the best possible match between the calculated and experimental values (table 2.6). The techniques so far described only allow for the calculation of perfect lattice properties; calculation of properties for a defective lattice requires that the method be amended.

The defect and the surrounding region of the lattice are simulated explicitly with the crystal outside this inner region being treated as a continuum. However, the assumption of point charges is no longer valid as polarization effects contribute. These are tackled by the use of the shell model, where the ion is regarded as a charged nucleus coupled to a charged electron shell by a spring. The spring constant and the shell charge are determined in an analogous way to that employed for the potential parameters. A set of interatomic potentials that are commonly used is given in table 2.7. As before the structure is allowed to relax and the internal energy calculated; the formatiom energy of the defect is the difference between the internal energies of the defective and perfect lattices. Care must be taken when applying these potentials as the calculations take no explicit account of thermal motions, and this can limit the accuracy at very high temperatures (Jackson et al 1985).

With the evolution of computer programs (HADES and

TABLE 2.6 CALCULATED AND EXPERIMENTAL LATTICE PROPERTIES AT 293K

PROPERTY	EXPERIMENTAL	CALCULATED
C_{11} (10^{10} NM^{-2})	38.93	40.06
C_{12} (10^{10} NM^{-2})	11.87	12.94
C_{44} (10^{10} NM^{-2})	5.97	5.78
ϵ_0	24	21
ϵ_∞	5.3	5.78

TABLE 2.7 PARAMETERS FOR A UO_2 POTENTIAL (JACKSON ET AL, 1984)

SHELL MODEL

	SHELL CHARGE/eV	SPRING CONSTANT/eVÅ^{-2}
URANIUM	6.54	94.24
OXYGEN	-4.4	296.2

SHORT RANGE POTENTIALS

(energies in eV and distances in Å)

$U_{(U-O)} = 1518.92 \exp(-r/0.38208) - 65.41/r^6$

$U_{(O-O)} = 11272.6 \exp(-r/0.1363)$ $r<1.2$

$= 5^{th}$ ORDER POLYNOMIAL $1.2<r<2.1$

$= 7^{th}$ ORDER POLYNOMIAL $2.1<r<2.6$

$= -134/r^6$ $2.6<r$

PLUTO) calculations on complicated defects in wide ranges of host lattices have been carried out. These results have been recognised as being important parts of the studies of fast ion conduction, charge transfer and oxidation, to name but a few applications.

CHAPTER 3 COMPLEX PLANE ANALYSIS

Section 3.1 INTRODUCTION

All networks consisting of resistive (R) and reactive (C,L) components can be reduced to an equivalent two component combination, irrespective of the network complexity. The resultant equivalent circuit may be comprised of either a series (R_sC_s) or a parallel combination (R_pC_p); each combination has its own advantages dependent on the initial network and the measurement device used. It is these reduced values that are returned by bridge techniques, utilising a four terminal pair configuration. Thus a method of analysis is required to retrieve the component information for the initial network from the measured values. This method exists and is termed complex plane analysis.

Section 3.2 SIMPLE NETWORKS

The initial network is transposed into a suitable equivalent by a consideration of the impedances of the network components, which may be obtained from the current or voltage resulting from the application of an ac voltage or current to purely resistive, capacitive and inductive loads such that

$$I(\omega)=V(\omega)/R \quad \text{resistive} \qquad 3.1$$

$$I(\omega)=-V(\omega)j\omega C \quad \text{capacitive} \qquad 3.2$$

$$I(\omega)=V(\omega)/j\omega L \quad \text{inductive} \qquad 3.3$$

These equations have the general form

$$I(\omega)=V(\omega)/Z(\omega)$$

where $Z(\omega)$ is the complex impedance of the element. The electrical impedance behaves, mathematically, in a similar manner to the electrical resistance:

$$Z_{TOT}=\sum Z_i \quad \text{series circuit} \qquad 3.4$$

$$Z_{TOT}=1/\sum 1/Z_i \quad \text{parallel circuit} \qquad 3.5$$

There are several other complex electrical quantities that are related to the electrical impedance

$$Y^*=1/Z^* \quad \text{admittance} \qquad 3.6(a)$$

$$C^*=1/j\omega Z^* \quad \text{capacitance} \qquad 3.6(b)$$

$$M^*=j\omega Z^* \quad \text{modulus} \qquad 3.6(c)$$

It is normal to describe the ac response of an electrical network in terms of rotating vectors, representing the field and current, in the complex plane. The complex impedance may physically be best understood in terms of the vector sum of the voltage resulting from the flow of a fixed reference current (figure 3.1), in a series RC circuit (figure 3.2) for which we may write

$$V(\omega)=(R+1/j\omega C)I(\omega)$$

$$=Z(\omega)I(\omega) \qquad 3.7$$

An equal importance must be afforded to the reciprocal of the impedance, the admittance, as this

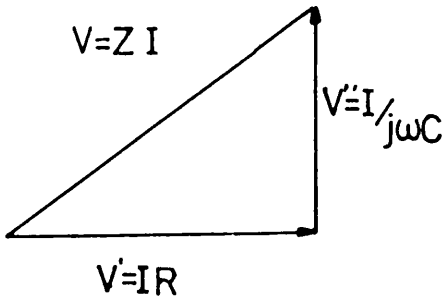

FIGURE 3.1
THE VECTOR DIAGRAM FOR A SIMPLE, SERIES, R/C CIRCUIT SUPPLIED WITH A FIXED REFERENCE CURRENT.

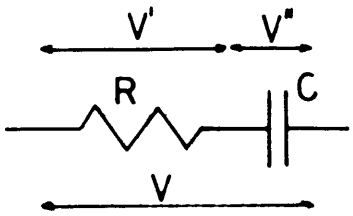

FIGURE 3.2
A SIMPLE, SERIES, R/C CIRCUIT.

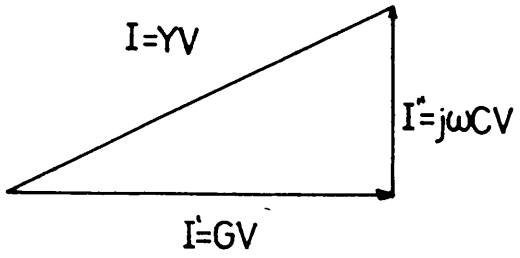

FIGURE 3.3
THE VECTOR DIAGRAM FOR A SIMPLE, PARALLEL, R/C CIRCUIT SUPPLIED WITH A FIXED REFERENCE VOLTAGE.

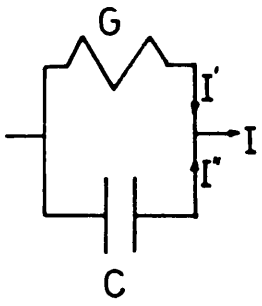

FIGURE 3.4
A SIMPLE, PARALLEL, G/C CIRCUIT.

represents the physical situation of a current flowing from the application of a fixed reference voltage (figure 3.3) to a parallel combination of G(=1/R) and C (figure 3.4)

$$I(\omega) = (G + j\omega C)V(\omega)$$
$$= Y(\omega)V(\omega) \qquad 3.8$$

It can be seen that the impedance or admittance as defined are complex quantities of the general form:

$$Z^* = Z' + jZ'' \text{ and } Y^* = Y' + jY''.$$

The real and imaginary parts of these quantities are generally frequency dependent and may be plotted against each other as a frequency dispersion. The resulting, ideal, dispersions for the circuits of figures 3.2 and 3.4 are given in figure 3.5(a) and 3.5(b) respectively.

The admittance is defined as the inverse of the impedance and may be transformed from the impedance representation by graphical or analytical means, so that the straight line of the impedance plot inverts to a semicircle of diameter 1/R (figure 3.5(c)). The reverse transformation applies for the admittance profiles.

Each of the complex representations used are derived from the same raw data though it is clear that each type of representation has it's own advantages in certain circumstances. The straight line profiles best identify the resistive component of the circuit and the circuit type. However the straight line plots provide minimal information on the reactive circuit components. In

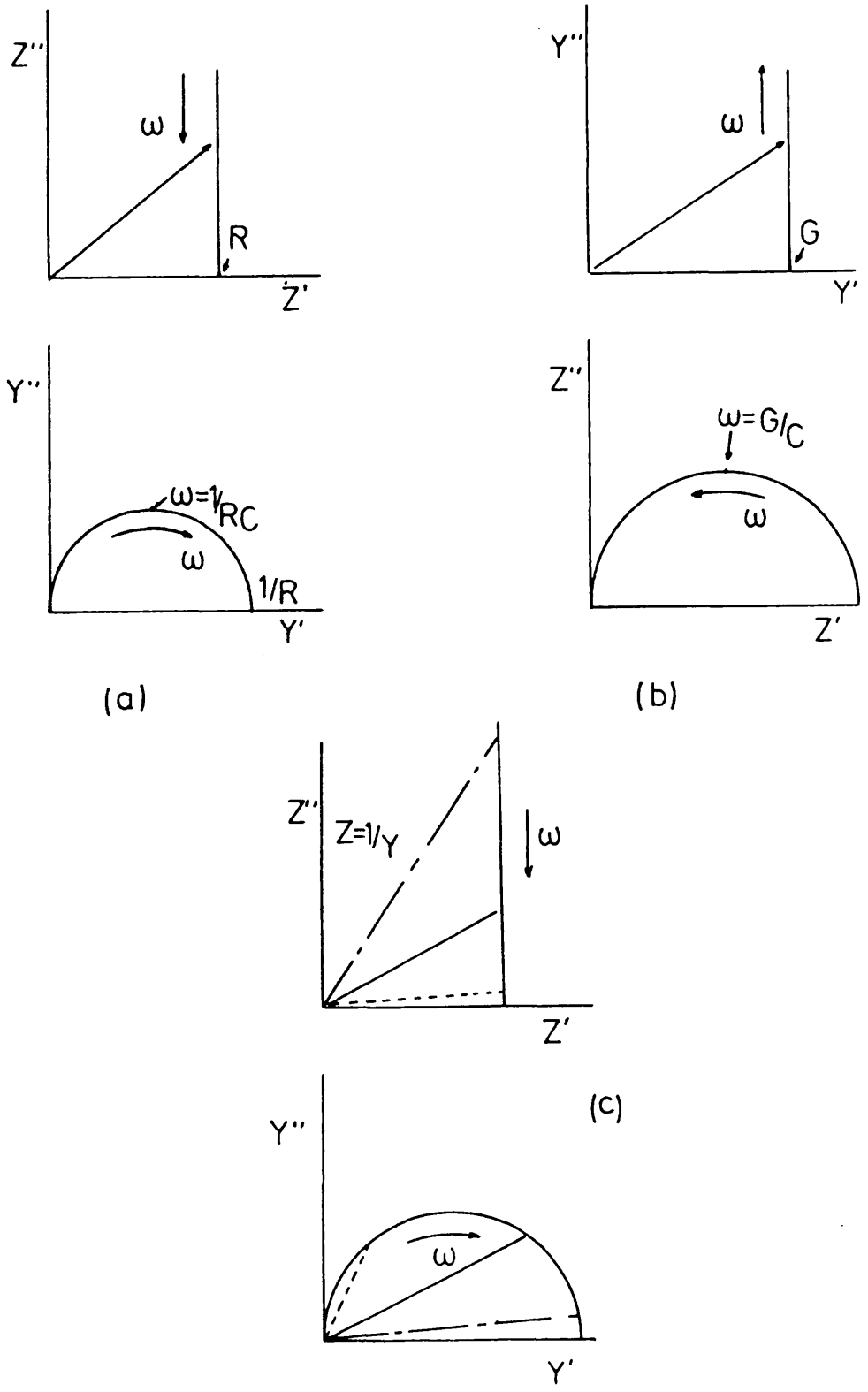

FIGURE 3.5
THE COMPLEX ADMITTANCE AND IMPEDANCE PROFILES FOR, (a) SERIES R/C CIRCUIT (FIGURE 3.2), (b) PARALLEL G/C CIRCUIT (FIGURE 3.4) AND (c) THE INVERSION FROM ONE COMPLEX PLANE TO ANOTHER

addition, for the semicircular profiles, the impedance representation provides better low frequency information whereas high frequency discrimination is best achieved with the admittance representation.

Section 3.3 PROFILES FOR SELECTED NETWORKS

The simple networks previously discussed provide the building blocks for more complicated networks and the complexity of the profiles increases in a similar block-like manner. Figure 3.6 shows a selection of more complicated networks, of increasing complexity, with the corresponding complex profiles.

The closest descendent of the simple parallel circuit is shown in figure 3.6(a) and is a resistance in series with a parallel circuit. This addition results in a shift of the impedance profile along the real axis by a value r. Alternatively a capacitance might be substituted for the resistance, providing the circuit of figure 3.6(b). The resulting admittance profile does not exhibit a shift along the real axis, though a spur is developed at the low frequency end of the profile. The addition of a capacitance or resistance in shunt with the series circuit gives the profiles shown in figures 3.6(c) and 3.6(d). These increases in circuit complexity result in the adaptions of the complex profiles as outlined.

A further increase in complexity is represented by

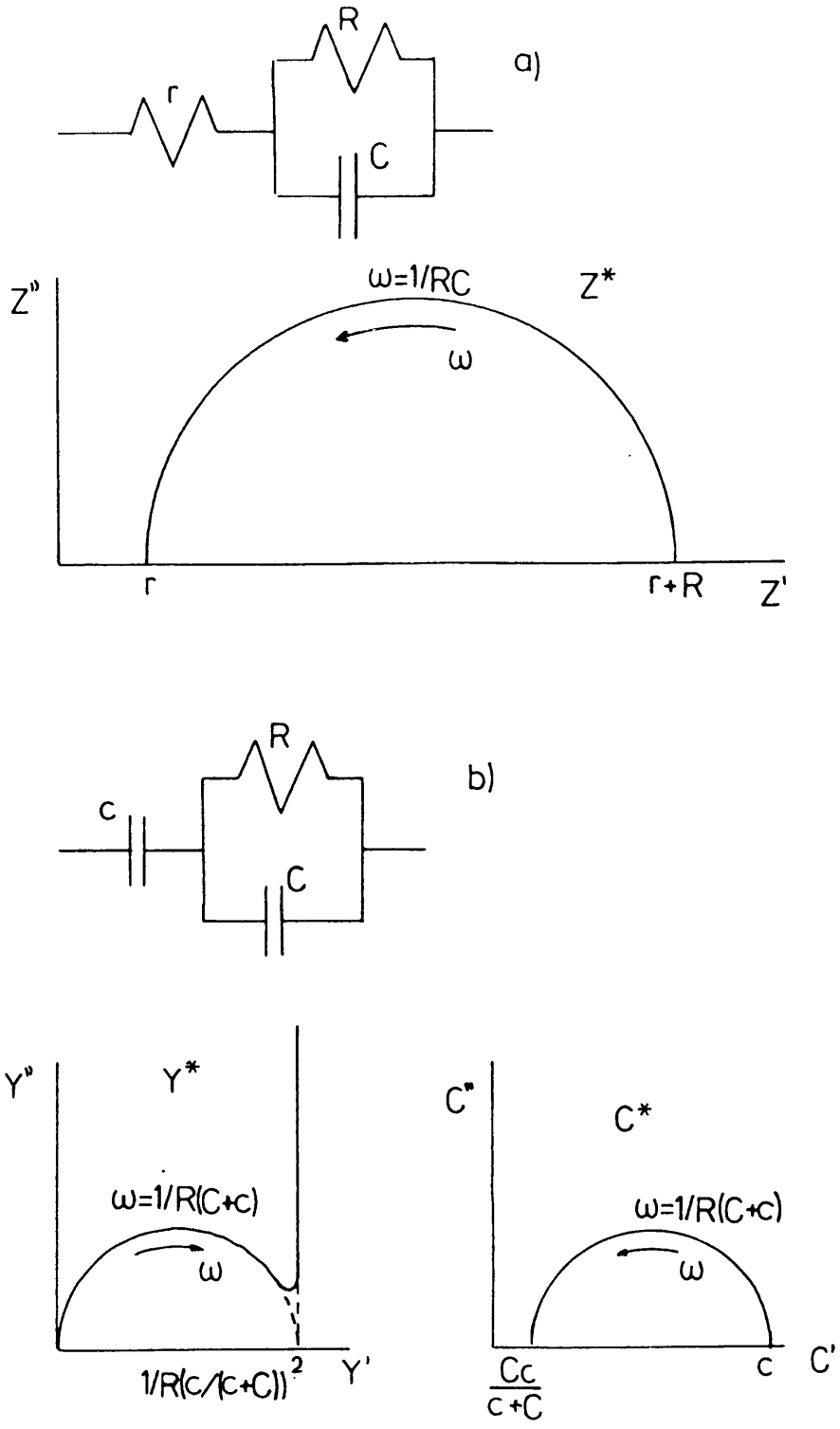

FIGURE 3.6 a) & b)
COMPLEX PLANE PROFILES OF SELECTED NETWORKS WITH ADDED SERIES ELEMENTS

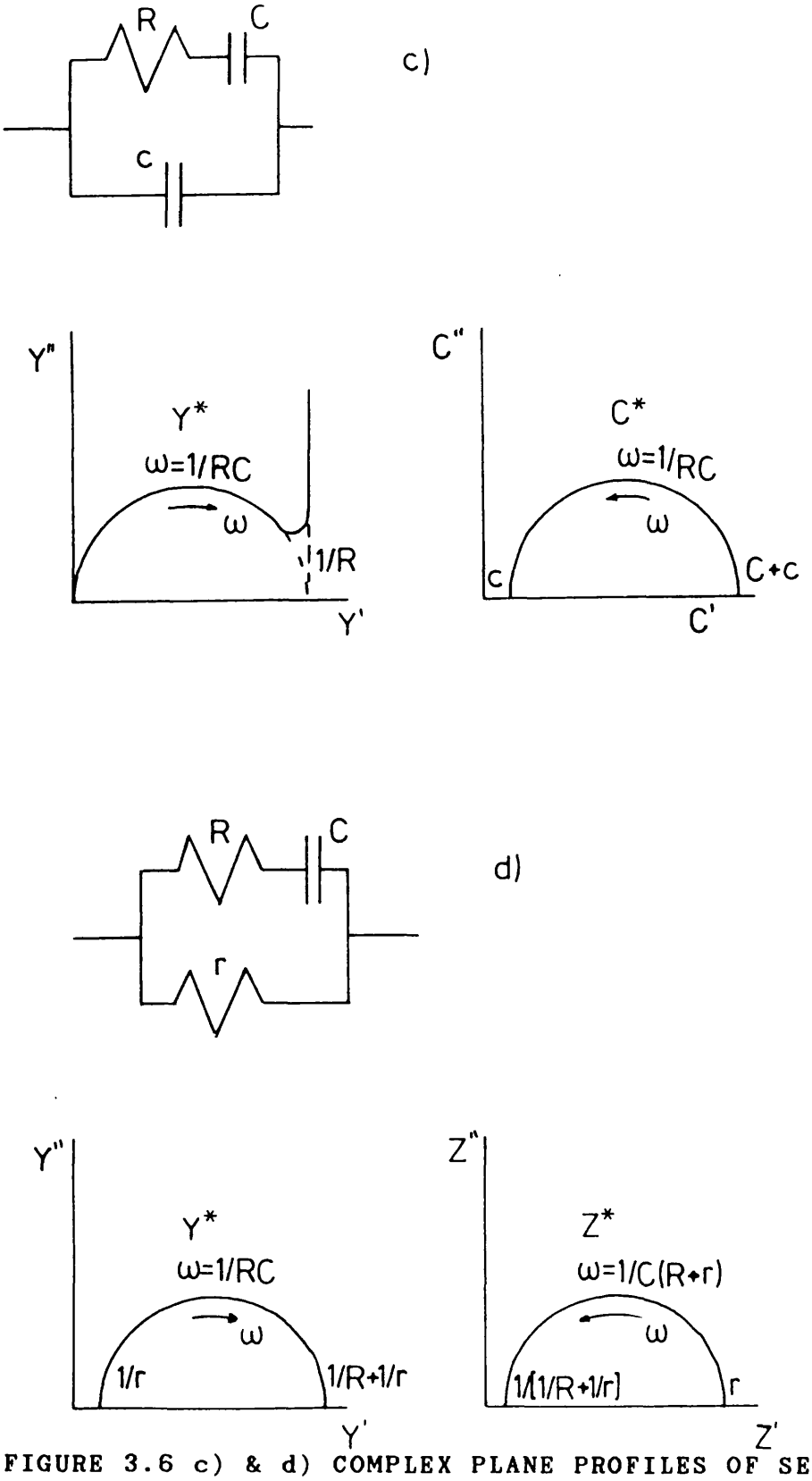

FIGURE 3.6 c) & d) COMPLEX PLANE PROFILES OF SELECTED NETWORKS WITH ADDED PARALLEL ELEMENTS

two parallel circuits connected in series (figure 3.7). The resultant profile is built up of a superposition of the two component profiles.

Section 3.4 SOME CAUTIONARY REMARKS ON ANALYSIS USING COMPLEX PROFILES

Throughout the previous discussion it will have become obvious that any one profile will not, necessarily, allow the identification of all of the network components. This is clearly shown in figure 3.6(b) where the admittance plot gives the component values as two combinations, whilst the permittivity, or complex capacitance, plot will provide all the necessary information. It should also be noted that the profiles shown are idealized, in that there is an infinite frequency range available, whilst this is not the case in any practical situation. The consequence of this may be easily visualised with respect to the permittivity plot of figure 3.6(b) where a finite frequency range may not allow enough of the profile to be traversed to estimate the high frequency C' intercept. These potential problems detailed may be solved by the use of two, or more, profiles consecutivaly.

A further complication, namely the degree of overlap of the features of the profile, may be inherent within the network itself. An illustration of this is given by the impedance profile, due to the circuit of figure

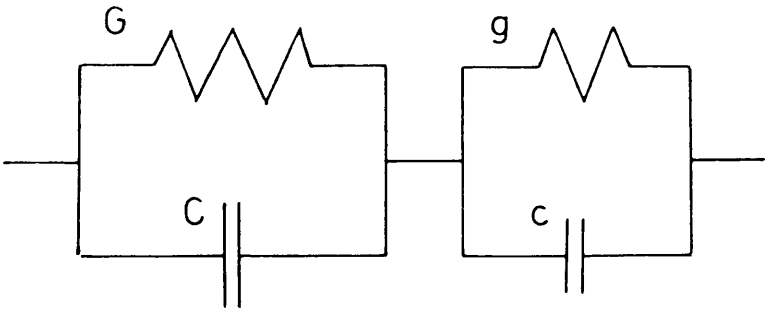

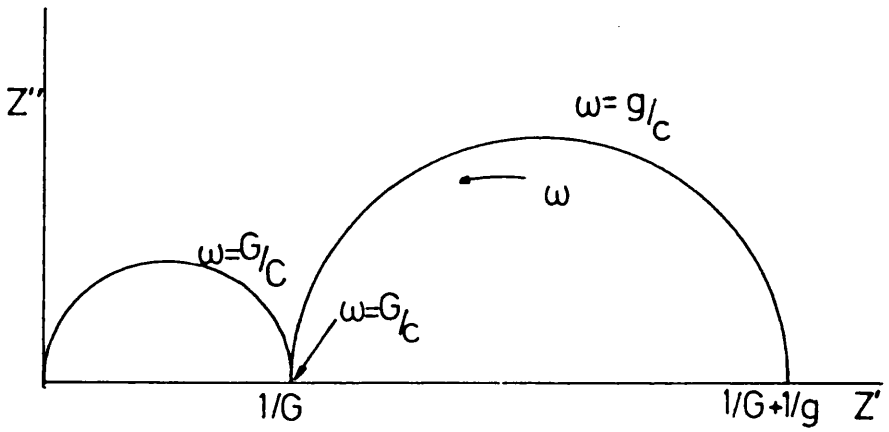

FIGURE 3.7
COMPLEX IMPEDANCE PROFILE FOR A SERIES COMBINATION OF TWO PARALLEL G/C CIRCUITS.

3.6(b), which may be seen redrawn appropriately in figure 3.8. The basic profile can be altered, sometimes out of all recognition, by the values of the components. A large difference between capacitances (figure 3.6(b)) provides a well-defined profile, but loss of definition takes place as the capacitances become more similar in magnitude. Should a large distortion of the profile occur, then identification of the circuit and the extraction of the component values would become more difficult. Thus a consideration of more than one complex profile will become necessary to identify and perform the full analysis of the circuit. This problem is highlighted by the circuits of figures 3.7 and 3.9; in the event of an overlap distortion the impedance profiles of these two radically different circuits become indistinguishible.

Finally it should be noted that with increasing network complexity the complex profiles, in general, become more similar in nature, thus enhancing the problems due to the overlap errors previously discussed.

Section 3.5 LOGARITHMIC REPRESENTATION OF COMPLEX PROFILES

Modern measurement devices make wide ranges of frequencies available when conducting electrical measurements, and as a consequence it is common for the measured values to encompass a large range. Thus when

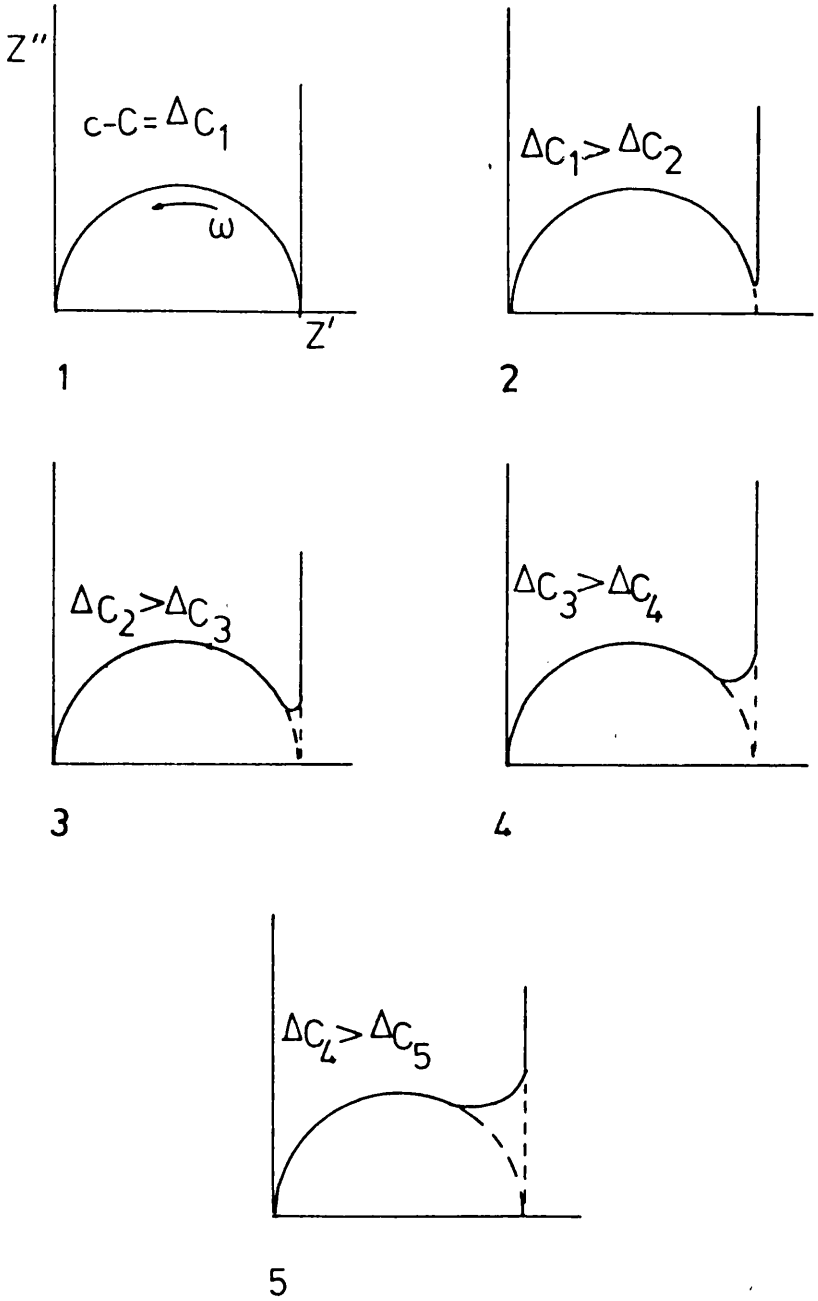

FIGURE 3.8
THE DISTORTION OF THE IMPEDANCE PROFILE CAUSED BY INCREASINGLY SIMILAR VALUES OF CAPACITANCES FOR THE CIRCUIT SHOWN IN FIGURE 3.6(b).

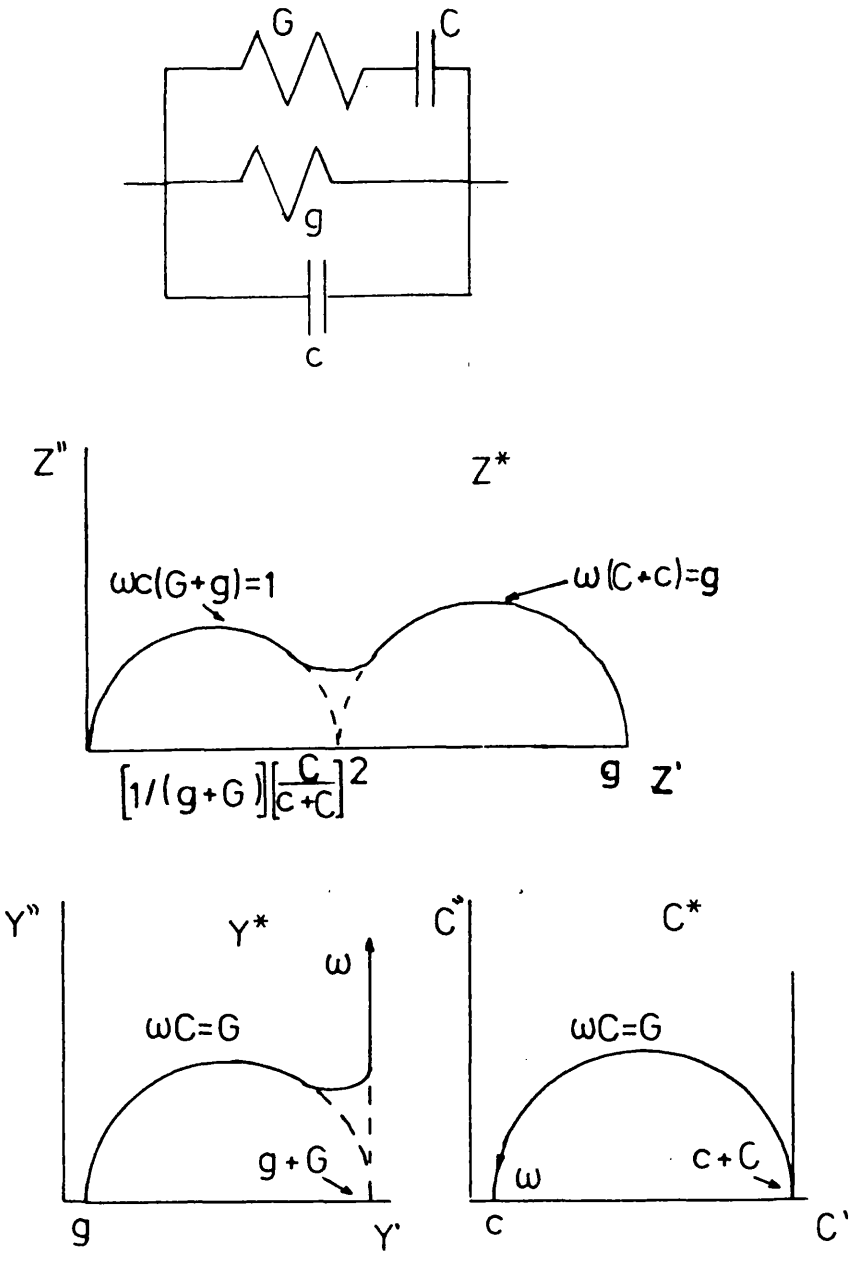

FIGURE 3.9
A COMPLEX CIRCUIT CONTAINING CAPACITANCES AND CONDUCTANCES, WITH THE ASSOCIATED COMPLEX PLANE PROFILES.

producing frequency plots a logarithmic representation is commonly used to display the entire information.

A logarithmic representation may be utilised in impedance and admittance profiles to express the whole range of the data. For instance the dual impedance semicircles of figure 3.7 may be in a ratio of many powers of ten and it would be completely impractical to express them on a linear scale. However, profiles plotted logarithmically will not have the same form as when plotted conventionally. This may be seen when the most important contour, the circular arc, is considered.

We may write the equation of an arc of diameter b as

$$x^2+y^2-2bx=0$$

In the region of the origin the equation may be approximated by

$$y=(2bx)^{0.5}$$

which logarithmically gives

$$\log(y)=0.5\log(x) + \text{constant}$$

Applying this to the circular arcs, represented linearly, in figure 3.10(a) the corresponding logarithmic representation is given in figure 3.10(b). The advantages of this type of representation are immediately obvious. The part of the arc adjacent to the origin is represented, logarithmically, by a straight line of slope 1/2, as the point (0,0) has the logarithmic coordinates $(-\infty,-\infty)$. Whereas the point (b,0) has logarithmic coordinates $(\log(b),-\infty)$. Thus a

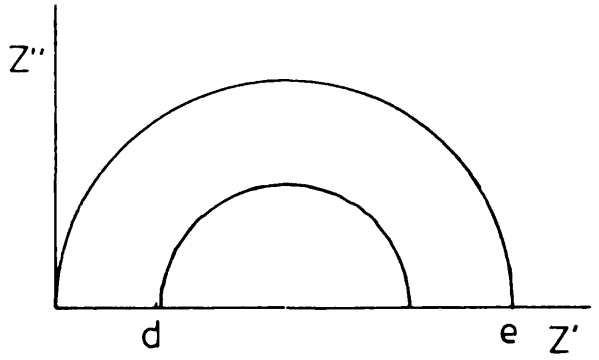

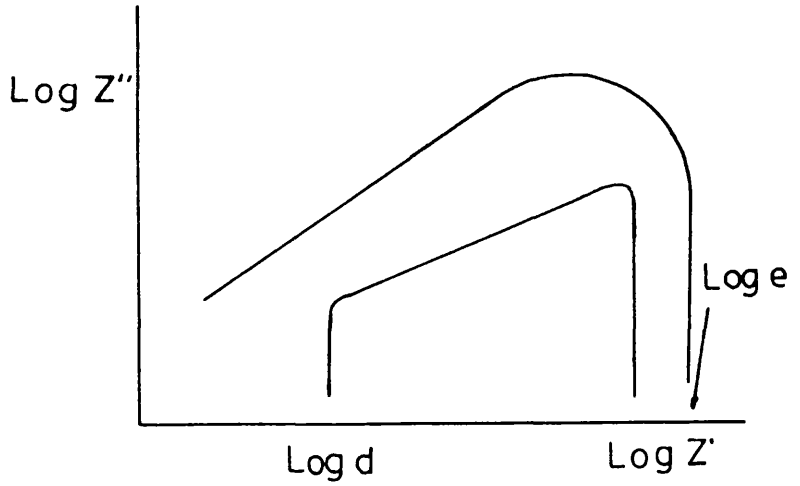

FIGURE 3.10
IMPEDANCE ARCS EXPRESSED, a) LINEARLY (TOP) AND b) LOGARITHMICALLY (BOTTOM).

logarithmic representation will allow small displacements of the arc from the origin, or arcs of a similar diameter, to be resolved more easily. Therefore it is evident that the impedance profile of figure 3.7 will be represented logarithmically by a combination of the profiles of figure 3.10(b). An actual example of this type of response is shown in figure 3.11, the data refers to a film of sputtered STAG glass with aluminium electrodes (Jonscher 1983). Here the ratio of the diameters of the impedance arcs is approximately 1000, yet each region is clearly resolved.

Section 3.6 THE PHYSICAL SIGNIFICANCE OF THE ELECTRICAL NETWORKS

The networks that have been considered so far are idealized, in that the components of the network are ideal (ie. single valued and hence parasitic free). Physically this will not be the case, because, for example, a capacitance will always have a finite conductance associated with it, causing an associated dielectric loss. Similarily a real resistor will always have some finite inductance, the converse being also true.

The circuit of figure 3.4 may be considered, initially (see section 3.7), as the equivalent representation for a real capacitor; here the loss current (due to G) is much smaller than the displacement current (due to C) ie $G \ll \omega C$. An alternative method of

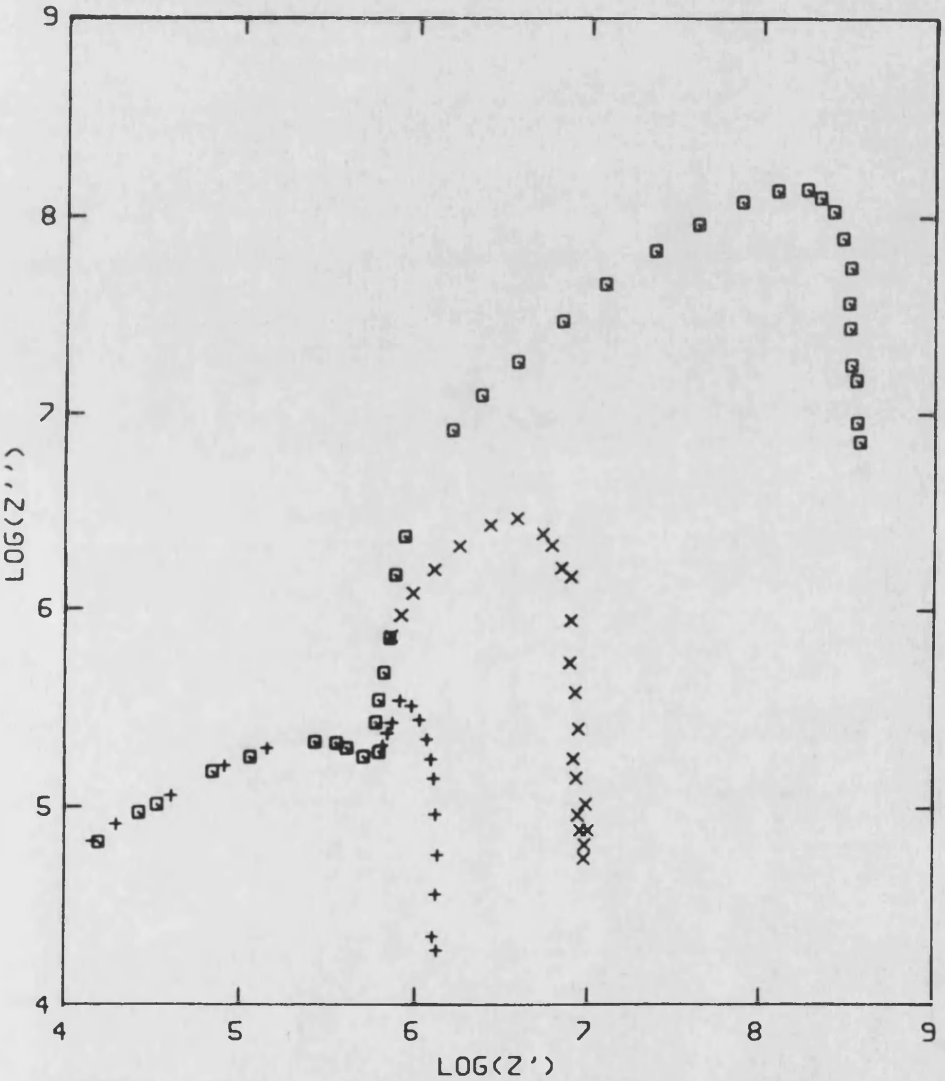

FIGURE 3.11
COMPLEX IMPEDANCE PROFILE OF A SPUTTERED FILM OF S.T.A.G. GLASS WITH ALUMINIUM ELECTRODES FOR SELECTED TEST VOLTAGE LEVELS (+ 4V, × 1V AND □ 0.2V), JONSCHER (1983).

expressing this mathematically for a real capacitor is to define the capacitance as a frequency dependent complex quantity $C^*=C'(\omega)+jC''(\omega)$, with C' representing the capacitive and C" the resistive (loss) components respectively. It then follows that the current flowing the system will be given by

$$I(\omega)=j\omega C^*(\omega)V(\omega) \qquad (3.9)$$

Should the loss current become comparable to, or greater than, the displacement current then the circuit cannot be considered to represent a capacitor. In such a case this circuit may be taken to represent a finite dc conduction mechanism in paralllel with some dielectric polarisation.

A similar representation may be ascribed to the circuit of figure 3.2, that of two physically different regions existing in series so that the same reference current causes separate voltage drops. Such a series combination will be present in systems where a bulk conducting or semiconducting region is adjacent to a barrier region; the barrier will be characterised by a capacitance as it is a region that is depleted of charge carriers.

A resistance in series with a R/C parallel combination, figure 3.6(a), is a common situation in that it may be taken to represent a barrier, with a finite conductance across it, placed in series with a

bulk conducting region. A dc conduction path is now present over the whole frequency: it is also possible to analyse the response by considering the effective conductance G*, in a similar manner to the capacitance C*. G" represents the dielectric properties of the circuit. A somewhat analogous situation to this is that of a non-conductive region (characterised by a capacitance) bordering a region of bulk conduction (the R/C parallel combination, figure 3.6(b)). The dimensions of the situation indicate that the bulk capacitance be much smaller than the barrier value, which acts only over a small width of the sample. Hence the impedance ($1/\omega C$) of the bulk predominates and the series capacitance merely perturbs the profile. This situation is important as it represents the case of an ideal (nonconductive) barrier. A real barrier may be represented by the series combination of parallel circuits shown in figure 3.7.

Thus the technique of complex plane analysis may be used to identify and analyse a great number of physical situations, as well as an abstract network of resistive and reactive components.

Section 3.7 REAL COMPONENTS - OR THE 'UNIVERSAL' RESPONSE

The discussion so far, even for physical situations, has been based on the conduction processes being

characterised by ideal (frequency independent) values for the resistive and reactive components. The dielectric properties of the medium, which determine the capacitance of the barrier, may be frequency dependent; the possible frequency dependences are detailed elsewhere (Zaky, 1970 and Frôhlich, 1958). The frequency dependent properties of a dielectric are shown schematically in figure 3.12. However there is a dilemma that must be faced: the frequency dispersion is used as a tool to unravel the complexities of the network, whilst the components of the network may be inherently frequency dependent.

This problem may be addressed in many ways though all of them require return to the basic circuits. The simple circuit for a capacitor (figure 3.4) may, by substituting a frequency dependent capacitor, be redrawn as figure 3.13. This shows a parallel combination due to the finite conductance, present in any dielectric, the high frequency dielectric constant, C_∞ , and a frequency dependent capacitance ($C_n(\omega)$) which encompasses dielectric relaxation and resonant absorption effects. It has been shown, by examining a large quantity of experimental data (Jonscher 1978, 1983), that $C_n(\omega)$ has a general form

$$C_n(\omega)=B(j\omega)^{n-1}$$

$$=B(\sin(n\pi/2)-j\cos(n\pi/2))\omega^{n-1} \qquad 3.10$$

From equation 3.8 the admittance of the circuit may be

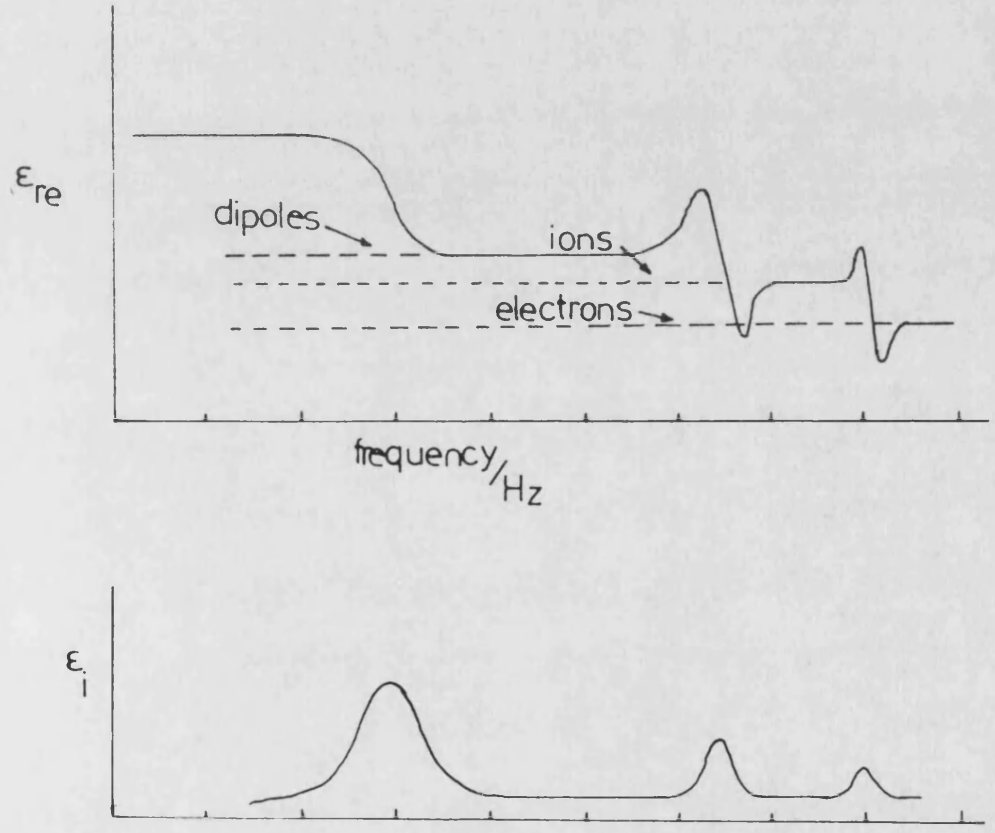

FIGURE 3.12
SCHEMATIC REPRESENTATION OF POSSIBLE DIELECTRIC RELAXATION PHENOMENA.

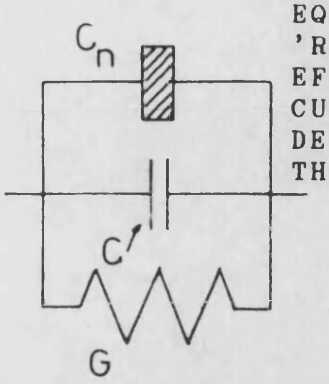

FIGURE 3.13
EQUIVALENT CIRCUIT FOR A 'REAL' CAPACITOR INCLUDING EFFECTS DUE TO A FINITE LOSS CURRENT (G) A FREQUENCY DEPENDENT DIELECTRIC (C_n) AND THE REFRACTIVE INDEX (C_∞).

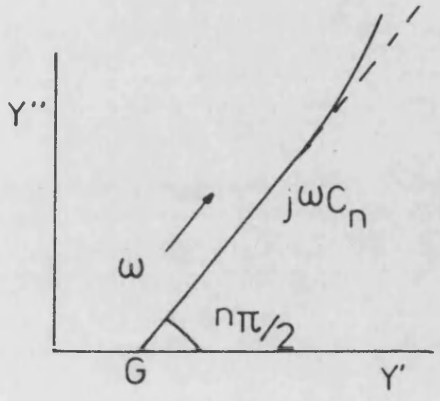

FIGURE 3.14
THE ADMITTANCE PROFILE DUE TO THE 'REAL' CAPACITOR DEPICTED IN FIGURE 3.13

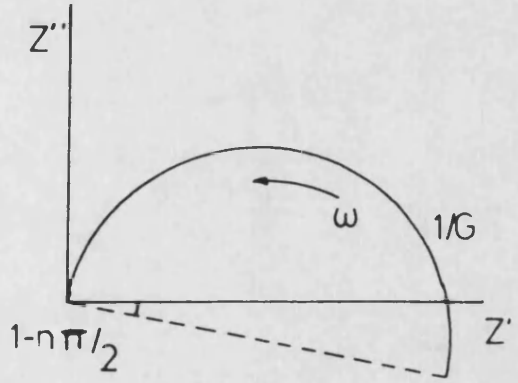

FIGURE 3.15
THE IMPEDANCE PROFILE DUE TO THE 'REAL' CAPACITOR DEPICTED IN FIGURE 3.13.

expressed as

$$Y(\omega)=G_o+ B(j\omega)^n+j\omega C_\infty$$

$$=G_o+B(\cos(n\pi/2) +j\sin(n\pi/2))\omega^n+j\omega C_\infty \quad 3.11$$

The exponent n defines the frequency dependence and must satisfy the inequality

$$0<n<1$$

This form of response has been termed 'universal' though in fact it has only been shown to hold for a vast number of cases. This form of the admittance is shown schematically in figure 3.14, in a linear format. The graphical representation corresponds, at low frequencies, to a straight line displaced along the real axis by G and inclined to it by an angle of $n\pi/2$; it is only at high frequencies, when dielectric losses no longer contribute, that the effect of the refractive index becomes important. Thus, in the limit of low frequencies, the admittance may be written as

$$Y=G_o+B(j\omega)^n$$

$$=G_o(1+(js)) \quad 3.12$$

where $s=\omega(B/G_o)^{1/n}$. From this form of the admittance the transformation to the impedance plane (figure 3.15), can be seen to result in a semicircle (figure 3.16), though the profile is now inclined at an angle of $(1-n)\pi/2$ to the real axis. To illustrate the different character of this 'universal' response the logarithmic representation of the impedance profile for this system is shown in figure 3.17, together with various other

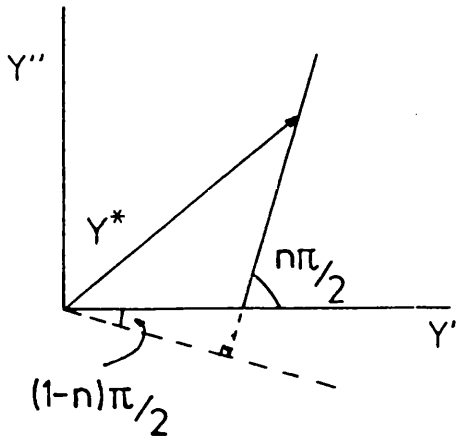

FIGURE 3.16
SCHEMATIC TRANSFORMATION FROM THE ADMITTANCE PLANE (FIGURE 3.14) TO THE IMPEDANCE PLANE (FIGURE 3.15) FOR A 'REAL' CAPACITOR.

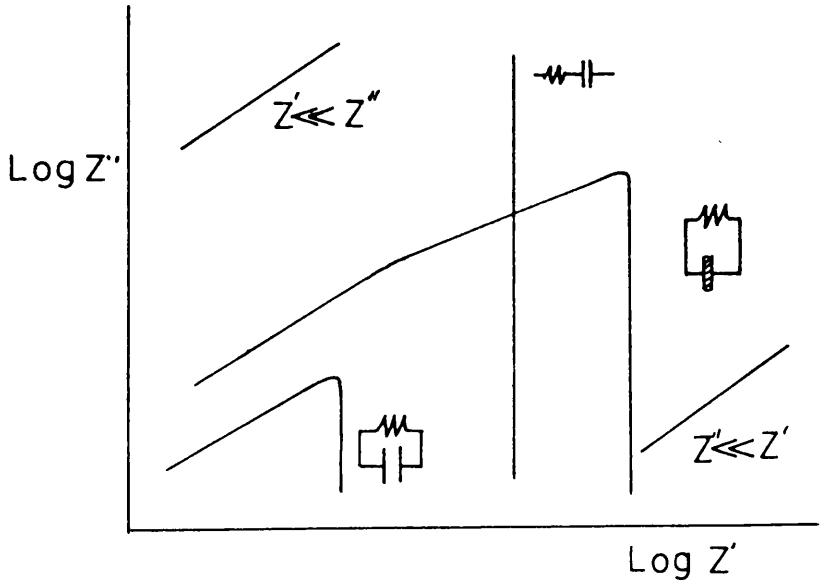

FIGURE 3.17
SCHEMATIC REPRESENTATION OF THE LOGARITHMIC IMPEDANCE PROFILE DUE TO A SIMPLE PARALLEL COMBINATION OF A FINITE CONDUCTANCE IN PARALLEL WITH A REAL CAPACITOR. LOGARITHMIC PROFILES DUE TO OTHER SIMPLE CIRCUITS ARE INCLUDED FOR COMPARISON.

types of dielectric response . The same perturbation of the profiles will apply for the more complicated networks, should they include a frequency dependent capacitance (ie an added series resistance will displace the profile along the real axis).

The method of fingerprinting the profiles may be used to provide the parameters of interest, with the identification of such frequency dependent behaviour relying on detecting an inclination of the admittance or impedance profiles. This may not always be possible if there is an insufficient frequency range to fully traverse the profile. An alternative route forward is to examine the frequency dependence of another complex quantity, examples of this are detailed elsewhere (Jonscher 1983). The distortions that can result from frequency dependent resistances, and the methods of analysis that are available, have been discussed by Almond and West (1984). It should be stressed that great care must be taken when applying complex plane methods to frequency dependent systems.

Chapter 4 EXPERIMENTAL TECHNIQUES

Section 4.1 SAMPLE PREPARATION

All of the samples used were supplied and prepared by AERE Harwell, the single crystal material being obtained from two sources, Degussa of West Germany and Norton Research of Canada. Samples were cut from these melt grown crystal, as they were received; after cutting, the samples were reduced to a nominal stoichiometry by heat treatment at 1400°C in dry hydrogen for more than 12 hours. Techniques for the analysis of the sample stoichiometry were not available for this work, though Norton crystals which had been treated in this manner have been analysed previously and found to be essentially stoichiometric ($UO_{2.00x}$).

The polycrystalline samples used were of uncertain origin though it is assumed that sintered material was prepared by heat treatment of stoichiometric powder. Chemical analysis of the stoichiometry was not carried out on these, or any other similar polycrystalline specimens.

All sample faces were machined flat and mutually perpendicular. To enable impedance measurements to be made opposing faces of the samples were coated with a conductor. Aluminium and platinum coatings were used initially; these coatings were found to give identical results when compared with coatings of silver conducting

paint. Thus coatings of paint and aluminium were used interchangebly depending on experimental convenience.

Section 4.2 ATTAINMENT OF LOW TEMPERATURES

Section 4.21 GLASS CRYOSTAT

Measurements in the temperature range 4.2K to 300K are accomplished using a conventional glass dewar system (figure 4.1) comprised of two double walled glass dewars, employing liquid nitrogen and helium refrigerents.

Electrical measurements between 80K and 300K can be taken both on cooling and warming using a method of controlled temperature drift. The magnitude of the temperature drift within the cryostat is determined, primarily, by the quality of the inner and interspace vacuums. A typical cooling / warming time, for the temperature range 80K to 300K, is approximately 6 hours.

Refrigeration of the system below 80K is achieved by the steady transfer of cold helium gas, with a final temperature of 4.2K being reached by the injection of a small amount of liquid helium. Within this low temperature regime measurements are taken primarily on warming: the cooling rate was much faster than the warming rate.

The sample holder used for this work (figure 4.2) is constructed from thin walled stainless steel tubing to reduce the conduction of heat into the dewar. The leads

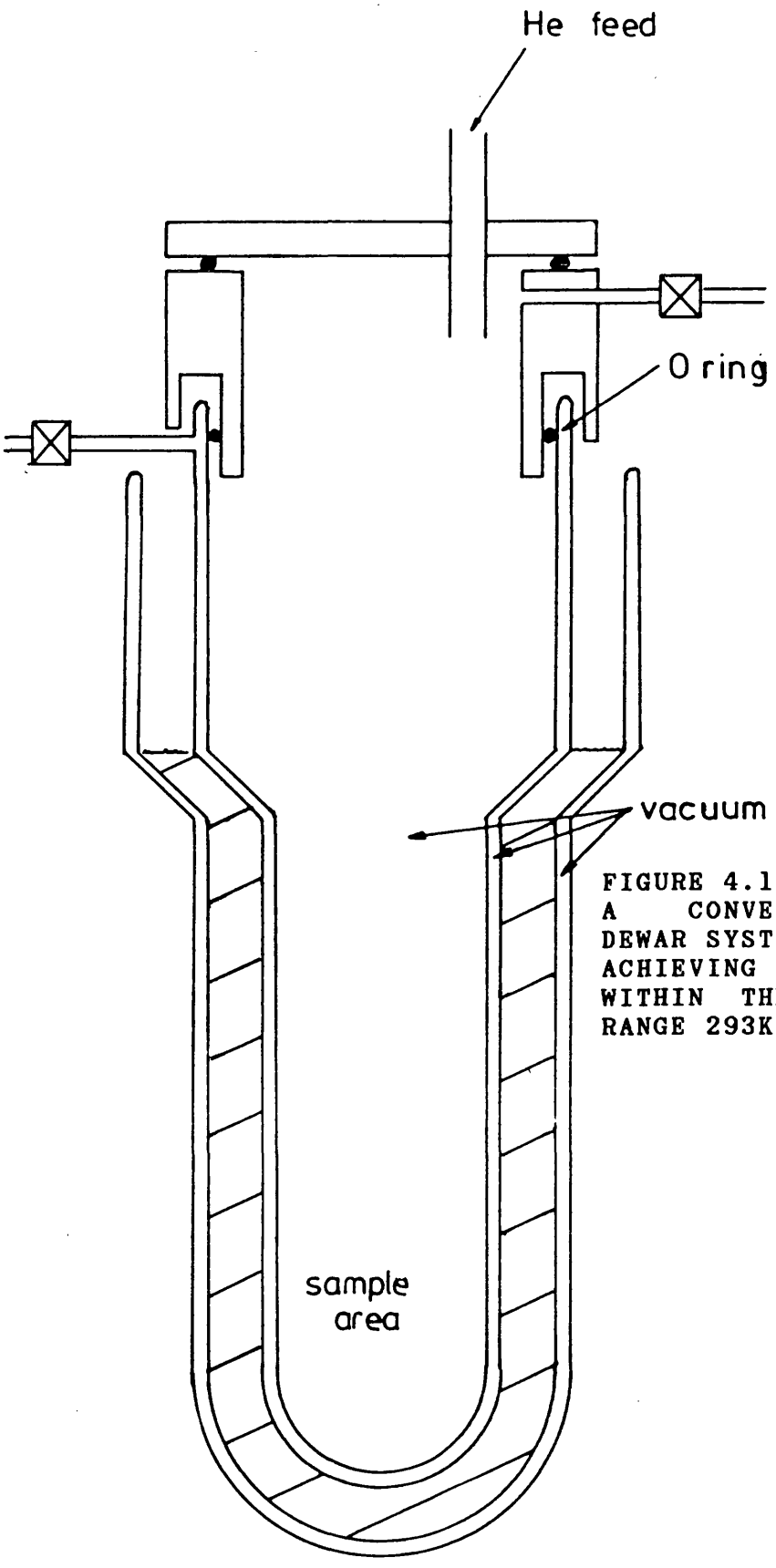

FIGURE 4.1
A CONVENTIONAL GLASS DEWAR SYSTEM, CAPABLE OF ACHIEVING TEMPERATURES WITHIN THE TEMPERATURE RANGE 293K TO 4.2K.

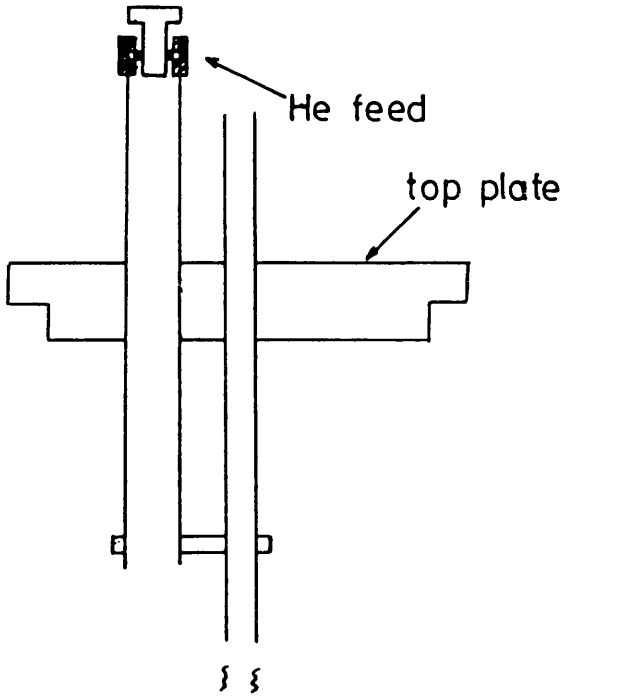

FIGURE 4.2
THE SAMPLE HOLDER USED IN CONJUNCTION WITH THE GLASS DEWAR SYSTEM.

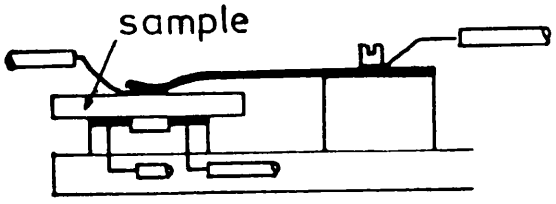

FIGURE 4.3
THE CONTACT SET ATTACHED TO THE SAMPLE HOLDER.

for electrical and temperature measurement are contained within the steel tubing and are taken out through vacuum seals constructed fron silicone rubber adhesive. Electrical connections to the sample are made by a specially constructed contact set (figure 4.3), onto which the sample is secured by the light pressure exerted by a phosphor bronze spring.

Section 4.22 NITROGEN FLOW VARISTAT

The nitrogen flow varistat (Thor C600) has a temperature range of 80-500K and is capable of maintaining any temperature within this range for up to 4 hours. The varistat (figure 4.4) consists of a stainless steel top plate rubber O ring sealed to an aluminium body. The top plate supports the vacuum control valves together with the electrical leadthroughs. Below the top plate is the sample mount support, inside which is housed the nitrogen reservoir which is connected to the sample block by a small diameter delivery tube. This tube connects to a secondary reservoir in the sample block, from which the exhaust line is connected to the exhaust valve.

The vacuum space between the outer case and the sample block is connected, via the vacuum separation valve to the inner vacuum space surrounding the nitrogen reservoir. The inner vacuum is improved by an absorbent material which is attached to the bottom of the nitrogen reservoir.

The exhaust valve controls the supply of liquid nitrogen to the sample block by restricting the exhaust gas flow. The temperature of the sample block can be maintained between 80K and 500K by balancing the nitrogen flow with the power supplied to the heaters, which are housed in the sample block. By adjusting the nitrogen flow to the minimum level the temperature is held just below that required, and the heaters are used to achieve finally the desired temperature. The heater power can be controlled manually or with a suitable temperature controller; a Thor E3010 is used in this work.

The varistat maintains the temperature at the cold face of the sample block, as it is below this that the control thermocouple is situated. Thus it is essential that the sample holder employed achieves good thermal contact with the controlled face, whilst retaining electrical isolation. This is achieved by the use of two spring loaded contact sets (figure 4.5), the upper being sprung more strongly than the lower. With the sample clamped, the upper central contact retreats more readily into its housing than the bottom (figure 4.6); this ensures thermal contact around the sample edge at the top only! The centre portions make electrical contact both on the top and the bottom.

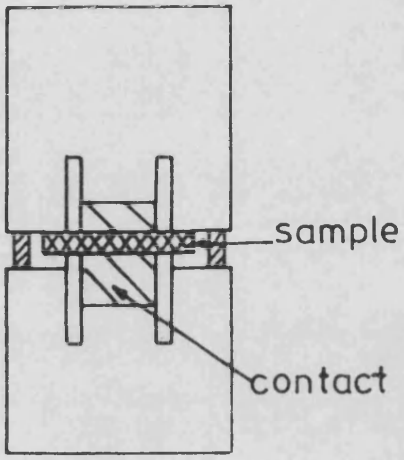

FIGURE 4.5
A FULL SET OF VARISTAT CONTACTS LOADED WITH A SAMPLE; THE TOP SET IS FIXED TO THE COLD FACE.

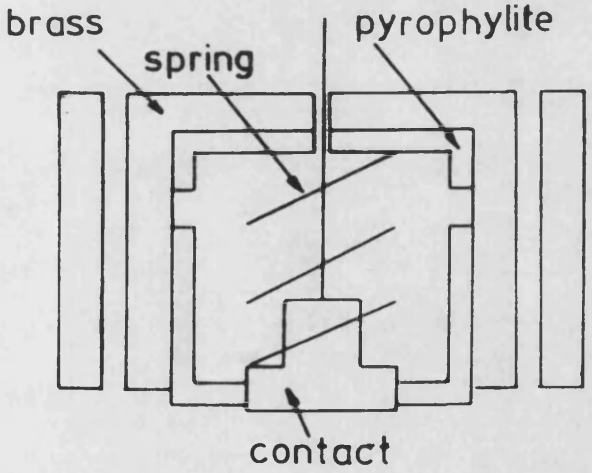

FIGURE 4.6
A CROSSECTION THROUGH ONE OF THE CONTACT SETS THAT ARE USED WITH THE NITROGEN FLOW VARISTAT.

Section 4.3 TEMPERATURE MEASUREMENT

Temperatures in the range 80K to 300K are measured by either copper constantan or gold-iron chromel thermocouples; temperatures between 4.2K to 80K are measured by gold-iron chromel thermocouples. Thermocouple junctions are produced by spark welding techniques, electrical isolation and some mechanical strength is provided by heat shrinkable insulation. The thermocouple voltages are compensated by electronic reference units, eliminating the need for reference junctions. A Comark thermocouple cold junction (type CJ/T) is used for the copper constantan junctions and an Ancom DTG 1000 for the gold-iron chromel thermocouples. The reference units produce reference voltages, equivalent to 273K, that are accurate to 0.5K within an ambient temperature range of -10°C to 50°C. The Ancom reference unit, (gold-iron chromel thermocouples) produces a linearised analogue output of 0.3mV/°C, this is in addition to acting as a reference cold junction. The Comark unit, used with the copper constantan thermocouple, acts only as a reference junction. Thus the temperature, for the copper constantan thermocouple, is calculated using a quadratic expression

$$V=3.95*10^{-5}T + 5.5*10^{-8}T^2$$

where T is the temperature difference and V is the thermocouple voltage.

Section 4.4 HIGH PRESSURES

High, hydrostatic pressures, are normally achieved in a piston and cylinder system (figure 4.7) with either a) a suitable oil as the pressure transmitting medium or b) a gas pressure medium. Gas systems involve large amounts of stored energy, and failure of these systems can sometimes lead to dramatic consequences. Thus it is more common for an oil filled piston and cylinder system to be used, though this does have some disadvantages. The pressure sealing of an oil system is achieved with O rings, generally constructed of rubber, and this limits the maximum pressure of the system to a few kilobars, typically 3Kbar. Such a system can be improved by increasing the sealing of the pistons to the cylinder by using more robust sealing rings eg viton or phosphor bronze. These techniques can increase the maximum pressures to typical values of 10Kbar, pressures in excess of this value are limited by other factors such as the bursting or deformation of the cylinder.
Increased pressures can be reached by certain adaptations of the basic principles using more mechanically favourable materials. The high pressures for this work have been achieved using the facilities that currently exist at the SERC High Pressure Facility of STL Harlow (Bridgman and Tetrahedral Anvils).

Section 4.41 BRIDGMAN ANVIL APPARATUS

The Bridgman anvil apparatus produces nominally

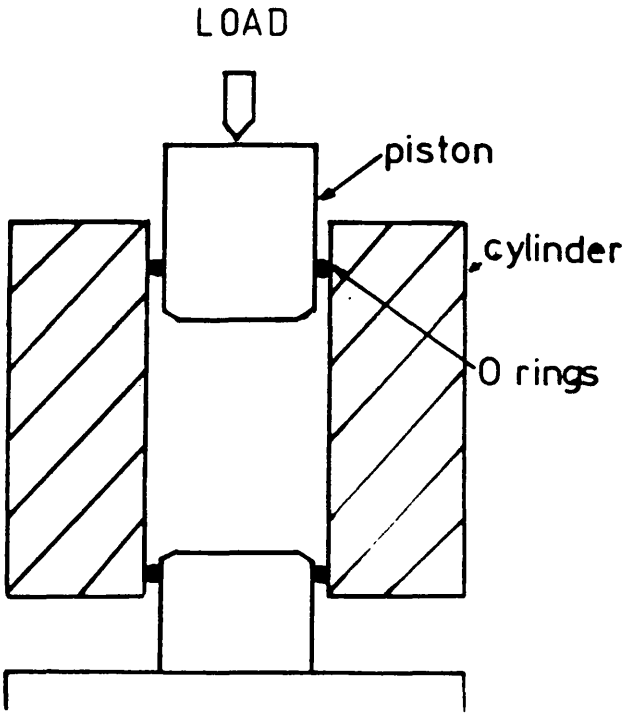

FIGURE 4.7
A TYPICAL PISTON AND CYLINDER APPARATUS FOR THE PRODUCTION OF HYDROSTATIC PRESSURES.

hydrostatic pressures within the pressure range 25Kbar to 120Kbar. This is done by squeezing the sample assembly (figure 4.8) between two tungsten carbide anvils. At low loads (1 to 5 tons) the magnesium oxide (MgO) loaded epoxy outer and the central epoxy portions deform until the outer hardens under the increasing load (>15 tons). The hardened outer section restricts the deformation of the central portion such that at loads in excess of 25 tons the central epoxy portion becomes an effective pressure transmitting medium.

Such a system would produce truly hydrostatic conditions only in the absence of shear components to the load as it is applied to the sample assembly. In addition large shear components would cause the sample assembly to be ejected from between the anvils, this is a major cause of experimental failure. The failure aspect can be inhibited by coating the anvil faces with jewelers rouge to achieve increased adhesion. Whereas shear components themselves can be reduced by ensuring good alignment of the components of the system, this is effected by assembling the anvils in a high precision die set (figure 4.9). The load is applied to the top of the die set which is located on ball bearing races such that these will take up most of the remaining shear components without transferring them to the sample assembly.

The die set location within the press is shown in

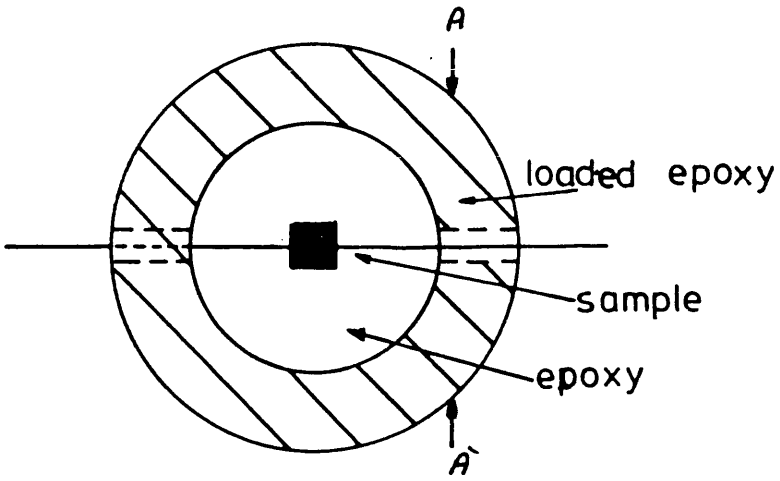

SECTION THROUGH AA'

FIGURE 4.8
THE SAMPLE ASSEMBLY USED TO ENCAPSULATE SAMPLES WITHIN THE BRIDGEMAN ANVIL APPARATUS.

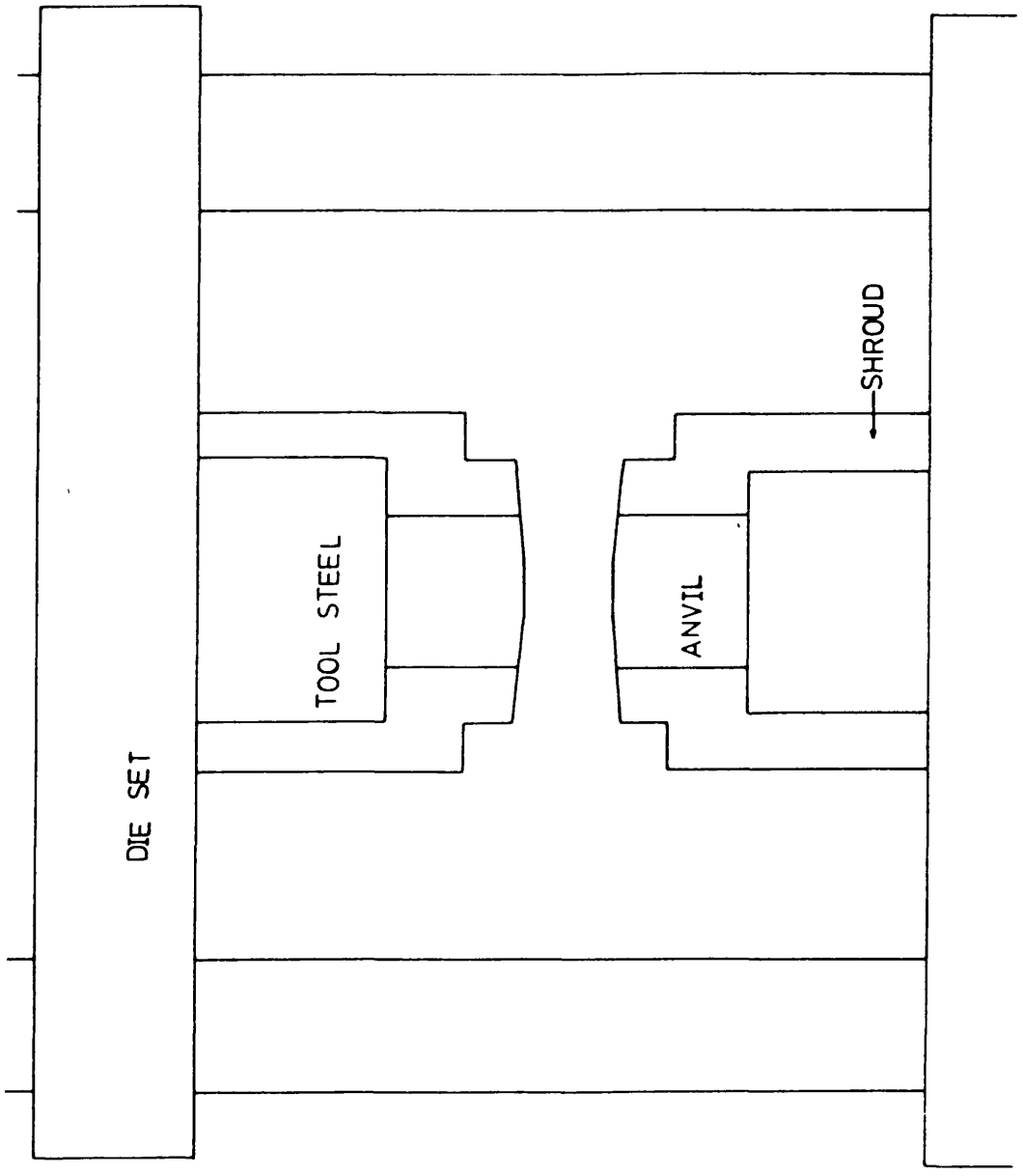

FIGURE 4.9
THE LOCATION OF THE BRIDGMAN ANVILS WITHIN THE PRECISION DIE SET

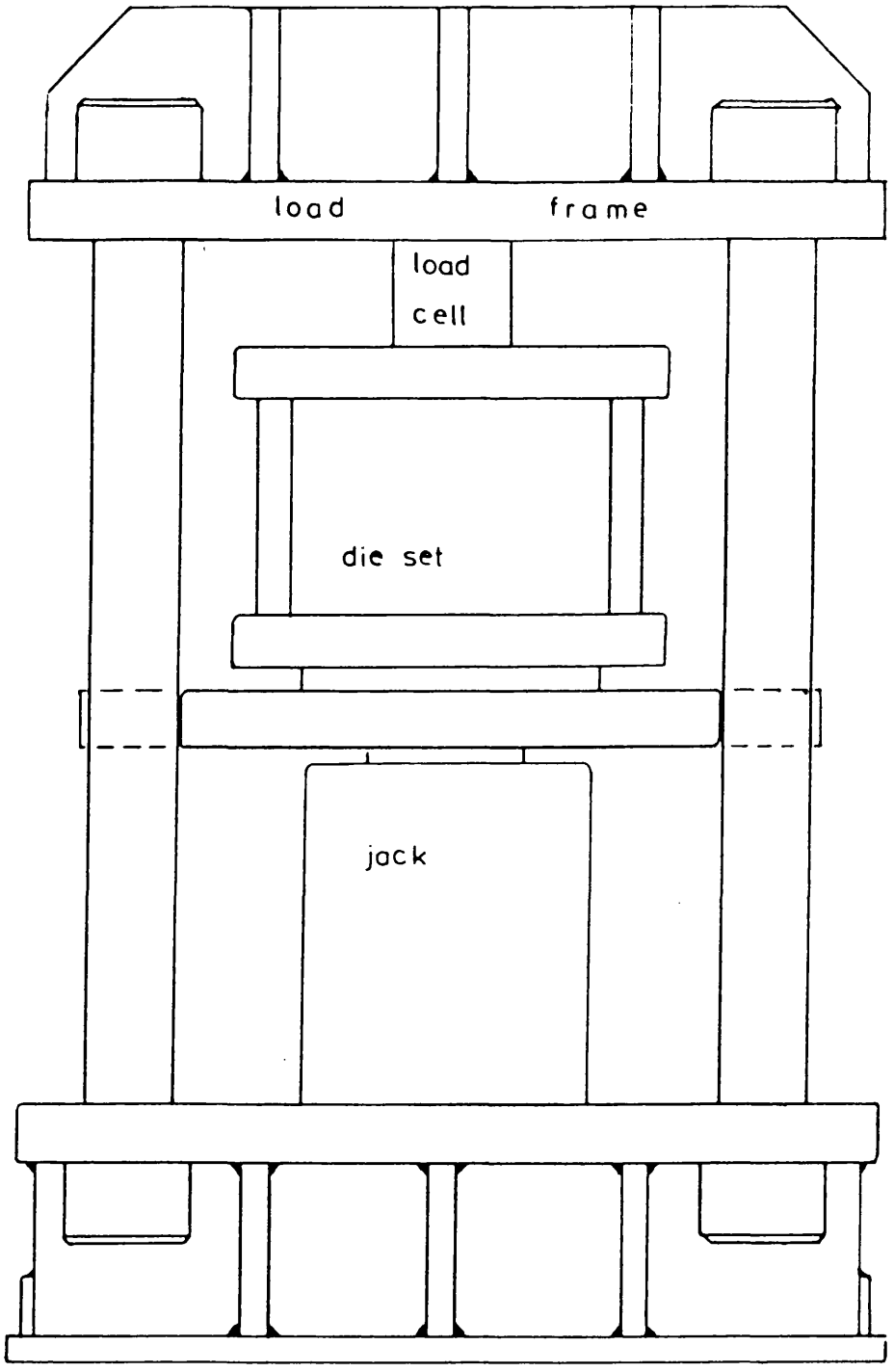

FIGURE 4.10
THE LOCATION OF THE DIE SET IN THE LOAD BEARING FRAME, SHOWING THE RELATIVE POSITIONS OF THE LOADING JACK, DIE SET AND THE LOAD CELL.

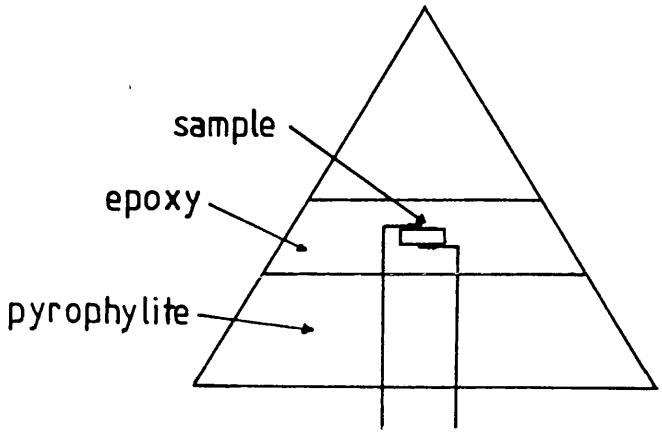

FIGURE 4.11
THE SAMPLE ASSEMBLY USED IN THE TETRAHEDRAL ANVIL APPARATUS FOR AMBIENT TEMPERATURE MEASUREMENTS.

FIGURE 4.12
THE LOCATION OF THE TETRAHEDRAL ANVILS WITHIN THE RETAINING COLLAR.

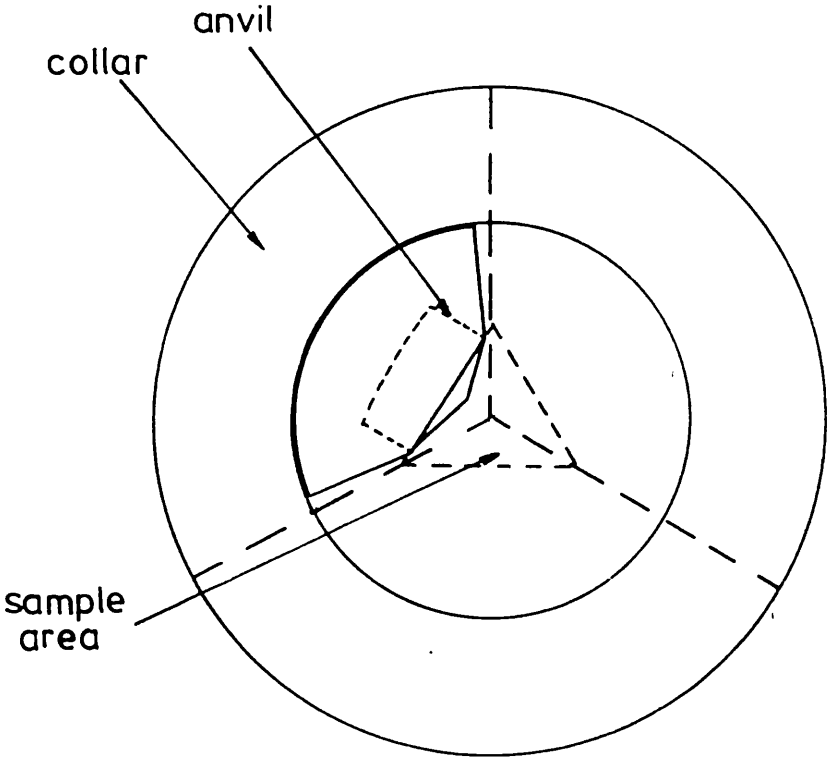

into the press.

At low loads the pyrophylite deforms and is extruded through the edges of the anvils; this leads to a contraction in the volume of the sample assembly. The geometry of the collar and anvils allows each anvil to settle equally into the collar to take up the sample assembly contraction. At loads in excess of 25 tons the extruded pyrophylite hardens forming a seal. The restrained epoxy resin at these loads becomes a pressure transmitting medium with the encapsulated sample being subjected to a hydrostatic pressure. Hydrostatic pressures are only attained when the extruded pyrophylite has hardened; the load required for this sets the lower pressure limit, typically 20Kbar; below this pressure the calibration curve is ill-defined and highly non-linear (figure 4.13). Due to the equal loading of the four anvils a sample in the tetrahedral apparatus is less prone, than one in a Bridgman apparatus, to shear components of the load, and hence experimental failure. The pressure exerted on the sample is determined from the load exerted by the press through a calibration curve (figure 4.13).

Elevated temperatures within the high pressure cell can be attained by two methods: 1) with nichrome windings for temperatures up to 120°C, 2) carbon resistance heating for temperatures up to 1500°C. Despite the limited temperatures achievable, nichrome

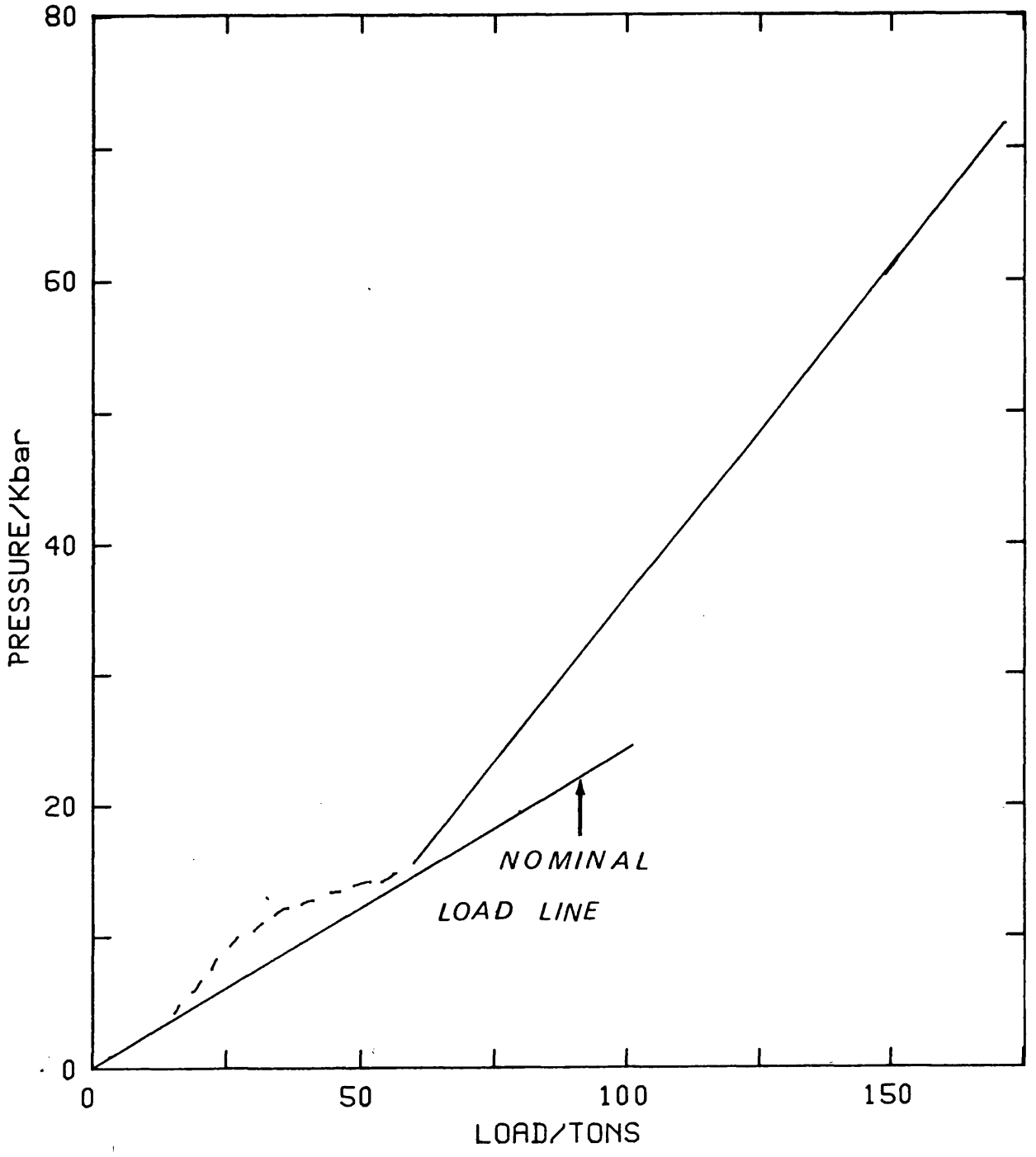

FIGURE 4.13

THE PRESSURE CALIBRATION CURVE FOR THE TETRAHEDRAL ANVIL APPARATUS.

windings have the distinct advantage of allowing repeated, independent, variations of the pressure and temperature. The limitations of this technique are discussed later (section 4.43(d)). Incorporation of a carbon heater increases the temperature range though it only allows temperature variation at one fixed pressure per sample assembly, the reasons for this are discussed in the following section (4.43(e)).

Section 4.43 SAMPLE ASSEMBLY PREPARATION

a) ELECTRICAL CONNECTIONS

The opposing faces of the small plate samples (1mm*1mm*1/2mm) used for this work are coated with evaporated aluminium, electrical connections are made to the coated faces by attaching thin stainless steel wire hooks with small ammounts of silver conducting paint. The mechanical strength of such a bond is poor and is supplemented by the application of a small ammount of epoxy resin to the hooks.

b) BRIDGMAN APPARATUS

The integral part of the sample assembly used on the Bridgman apparatus is the washer of magnesium oxide (MgO) loaded epoxy resin within which the sample is encapsulated (figure 4.8). The washer is cast from a PTFE mould into which dry MgO powder is compressed. The powder is uniformly impregnated with epoxy resin by initially pouring the resin over it, the mould is then heated to about 50°. After heating the mould is placed

in a vacuum desiccator, whilst still hot, to encourage the penetration of the resin and to inhibit the formation of voids. This procedure of heating and evacuation is repeated numerous times over a period of 8 hours, after which the washer is cured at 60°C for 48 hours.

The strengthened sample (section 4.43(a)) is fitted into the central portion of the washer with the wires lying in the prepared channels (figure 4.8). The sample and wires are secured with epoxy resin which is added dropwise to fill all the available spaces, thus avoiding the formation of cavities. The sample assembly is stabilised by a further curing of the epoxy resin at 50°C for four hours.

c) TETRAHEDRAL APPARATUS

The central component of the sample assembly, as used in the tetrahedral anvil apparatus, is the pyrophylite tetrahedron (figure 4.9), which is fabricated by compressing dry pyrophylite powder in a heated mould. Two holes are drilled in the tetrahedron to accept the encapsulated sample (section 4.43(a)) and a chromel alumel thermocouple. These are secured by filling the holes dropwise with epoxy resin.

d) TETRAHEDRAL APPARATUS INCORPORATING NICHROME WINDINGS

The sample assembly incorporating the nichrome windings is very similar to the standard assembly (section 4.43(c)) except that a larger tetrahedron is

used to accommodate the sample and windings. Power is supplied to the windings via wires which are taken out through the edge of the tetrahedron. It is the increased size of the tetrahedron that contributes to the increased number of experimental failures for this sample assembly - the increased size results in an increased extrusion of material and this causes the fracture of either the measurement, thermocouple or heater leads. The upper temperature limit that this type of sample assembly can reach is set by the mechanical properties of the encapsulation material, which degrade rapidly at temperatures in excess of 130°C.

Section e) TETRAHEDRAL APPARATUS INCORPORATING CARBON RESISTIVE HEATING

Temperatures greater than 130°C can be attained by utilising a ceramic encapsulation material with a carbon resistance heater. The tetrahedron used for high temperarures is the same size as that used for the ambient temperature procedure of section 4.43(c). The ceramic encapsulated sample is fitted into the resistance heater with ceramic adhesive (Cerastil C10), which is an interference fit with the sample hole of the tetrahedron (figure 4.14). The current for the heater is supplied through two of the lower anvils, which are electrically insulated by sheets of mica and PTFE (primarily to reduce the friction of the anvil with the

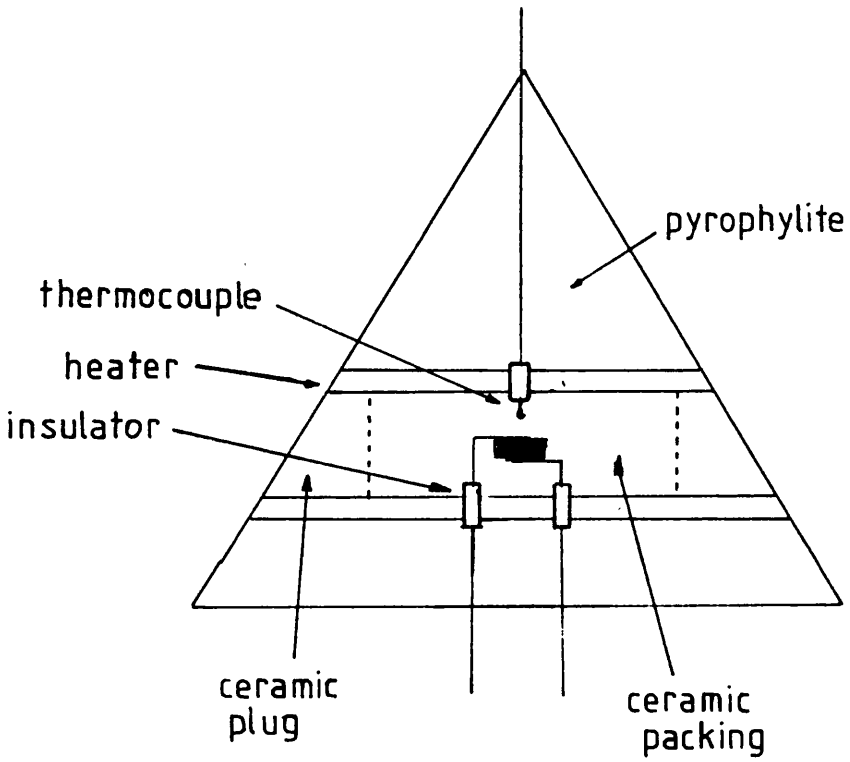

FIGURE 4.14
THE SAMPLE ASSEMBLY USED IN THE TETRAHEDRAL ANVIL APPARATUS FOR TEMPERATURES UP TO 1700K, USING AN INCORPORATED CARBON HEATER.

collar). The thermocouple used for these measurements is platinum platinum-13% rhodium.

The electrical connections employed for temperatures in excess of 130°C differ substantially from those used for lower temperatures. The electrodes are formed by flattening the ends of 0.5mm diameter platinum wire which are trimmed to form 1mm*1mm electrodes. The electrodes are stuck to the opposing sample faces by an amyl nitrate adhesive. The sample assembly is encapsulated in a small amount of ceramic adhesive, thus lending some degree of mechanical support. The ceramic is dried slowly from the outside causing a crust to form which, in turn, exerts a small pressure on the electrodes. With the electrodes held in position the temperature is then raised causing evaporation of the amyl nitrate adhesive, which percolates out of the assembly. When the ceramic has fully hardened, the electrodes are firmly clamped by the ceramic giving good ohmic contact with the sample faces.

There are two main causes of experimental failure for this assembly and they are fracture of thermocouple leads (they have a greater length within the pyrophylite than the measurement leads) and crumbling of the resistance heater at the point of contact with the anvils, due to the large temperature gradient. Both of these faults are not as serious as they seem at first sight; the degradation of the heater merely reduces the

maximum temperature that may be reached and rarely occurs below 1300°C. Fracture of the thermocouple leads does not result in a total lack of information on the sample temperature as this may be determined from a calibration curve of heater current against sample temperature (figure 4.15).

Section 4.50 MEASUREMENTS AT HIGH TEMPERATURES

Measurements in the temperature range 300K to 1700K at atmospheric pressure were made, at CEGB Berkeley Nuclear Laboratories, using a Metals Research PCA 10 furnace (figure 4.16). The furnace utilises the resistive heating of tungsten windings, which are situated between two silica tubes through which is passed hydrogen as a reducing gas. The sample is supported inside the inner tube on a platform of ceramic tubes and spacers. A separate hydrogen flow is supplied to the sample to prevent it's oxidation. Electrical connections are made by four spring loaded tungsten hooks running inside of the ceramic tubes; the spring loading allows for adequate mechanical contact at the elevated temperatures used for this work and allows for thermal expansion.

The furnace is linked to a Eurotherm temperature controller using a tungsten tungsten-13%rhenium thermocouple, to measure the winding temperature. The controller is able to achieve stable temperatures,

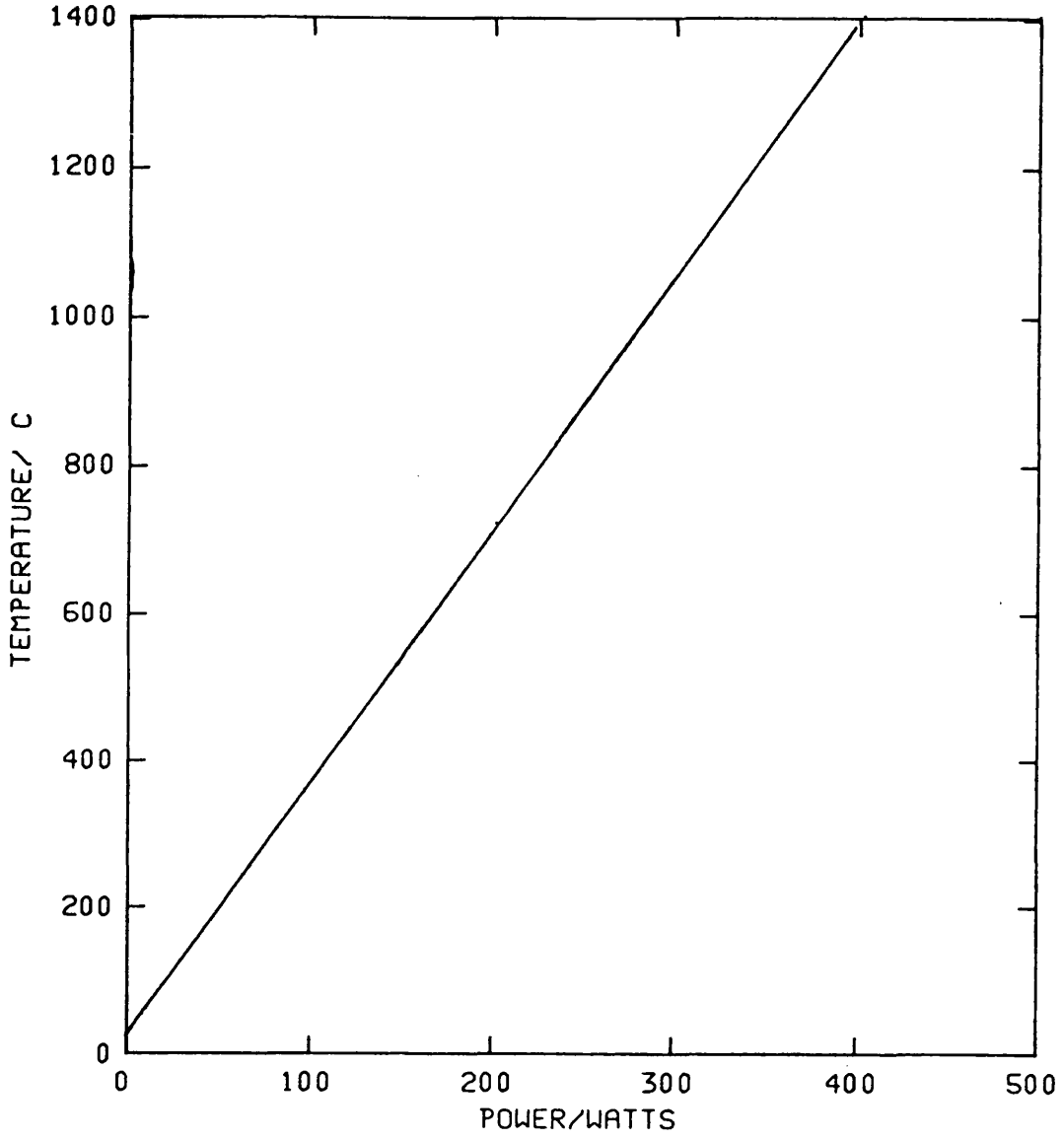

FIGURE 4.15

THE TEMPERATURE - HEATER POWER CALIBRATION CURVE FOR A TETRAHEDRAL ANVIL SAMPLE ASSEMBLY, USING A CARBON HEATER.

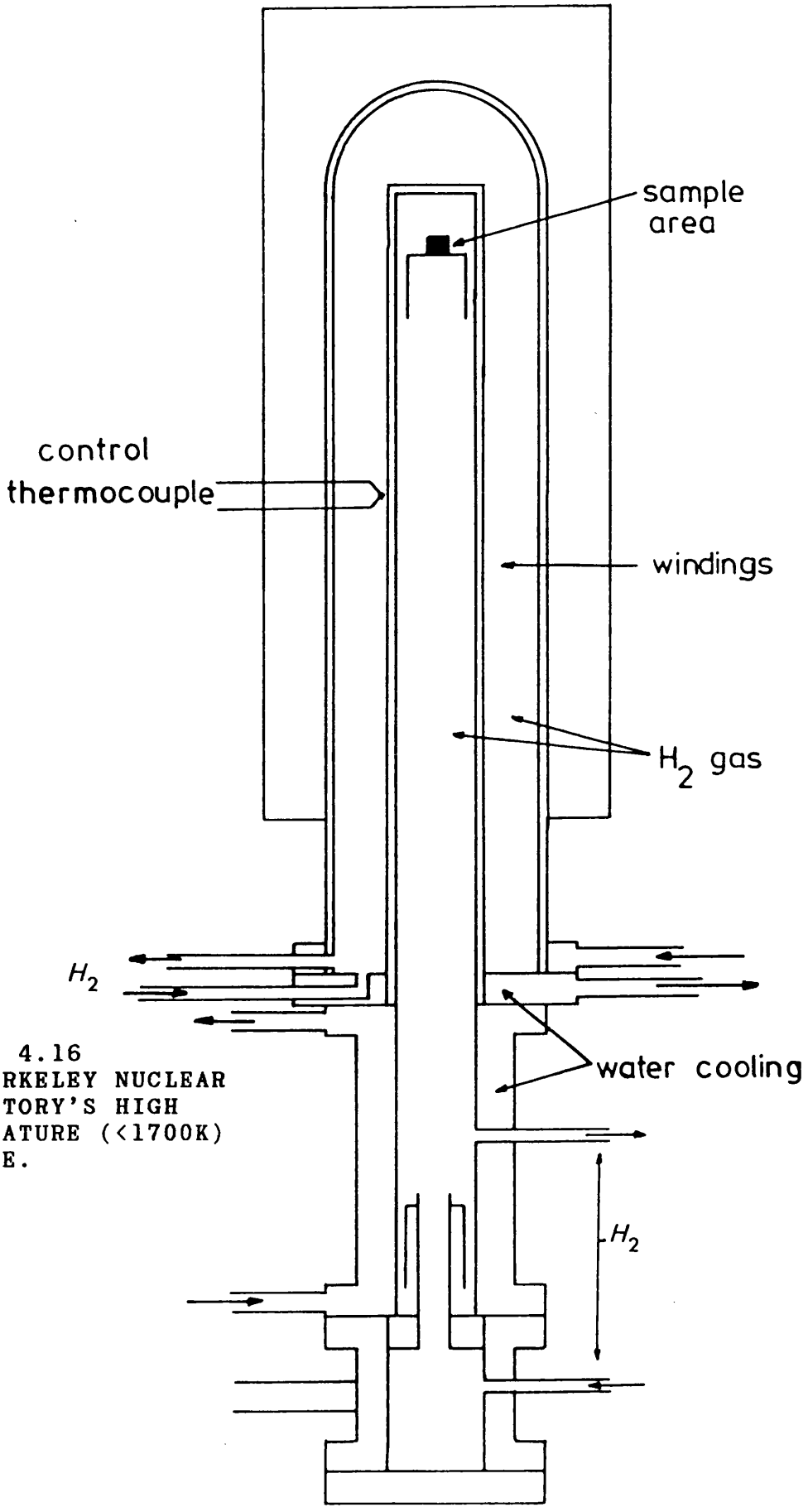

FIGURE 4.16
THE BERKELEY NUCLEAR LABORATORY'S HIGH TEMPERATURE (<1700K) FURNACE.

within the range of the furnace, with a variation of approximately 3K in the sample temperature. The temperature of the sample is considerably higher (about 70-100K) than that measured at the windings; thus it is measured by a tungsten-5%rhenium tungsten-13%rhenium thermocouple, located directly underneath the sample support. Using this arrangement it is possible to make measurements both on heating and cooling.

Section 4.6 MEASUREMENT SYSTEM

A fully automated system for making ac measurements over a maximum frequency range of 5Hz to 13MHz under a variety of physical conditions has been constructed. The system is based around the Hewlett Packard Low Frequency 4193A Impedance Analyser which is controlled by a Commodore PET 8040 mini computer, through the IEEE interface facility. The mini computer allows software control of the frequency range, frequency increment and test voltage in addition to providing a data storage facility. The system could allow either single frequency measurements or multi-frequency, impedance profile, measurements to be made.

Data acquisition for the temperature controlled devices is straight forward with a number of frequency runs at selected test voltages being easily achieved at each temperature. The method employed for data acquisition over a range of temperatures, using the

glass cryostat (section 4.2), is that of a controlled temperature drift. Control of the drift is essential due to the finite time that is required to accumulate the frequency data, typically 60-90 seconds. The measurement time is mainly dependent upon the settling of the instrument after the parameters have been changed and the software averaging of the measured values. A large temperature drift results in the temperature change within the measurement time becoming too large. The most satisfactory method to ensure an acceptable match between the temperature drift and the measurement time is to set a suitable drift using the cryostat vacuums and then to fine tune the measurement time, by adjustment of the settling time and software averaging, to achieve the requirement. At no time were these values reduced below those necessary to ensure measurement accuracy. The system took account of the finite drift during the measurement cycle by measuring the temperature at the start and end of the cycle, a difference of typically 0.5K to 0.75K being measured. The drift within the measurement cycle was assumed to be linear, thus enabling a temperature correction to be made to all the data.

Section 4.7 TWO AND FOUR TERMINAL TECHNIQUES

When a two terminal device is used to take measurements of an unknown impedance, a perturbation of the circuit due to the leads (figure 4.17) results. The

lead impedance (R+j L) and the contact resistance r are in series with the unknown impedance and cause additive measurement errors. The stray capacitance C has negligible effect on the measurement if the unknown (Z) has a low value of impedance, between 10^{-3} and 100 . However, a low value of the impedance will enhance the errors due to the lead and contact impedances. The measurement errors that are introduced with the two terminal technique can almost completely be eliminated by using a four terminal configuration (figure 4.18).

The four terminal configuration has the voltage monitor connected directly across the unknown impedance, thus eliminating the contributions due to the lead and contact impedances caused by the current, I, supplied. The lead and contact impedances connected between the voltage sensing terminals have negligible effects because the input impedance of the voltage monitor is very much greater than that of the unknown; consequently the current, i, drawn through these impedances is very small. Though this method can be used over a large impedance range, especially low impedances of 10Ω or less, it has two inherent disadvantages:-

1) Mutual inductance effects between the current and voltage leads (M in figure 4.18)
2) Sensitivity to externally generated noise, which is especially significant in high

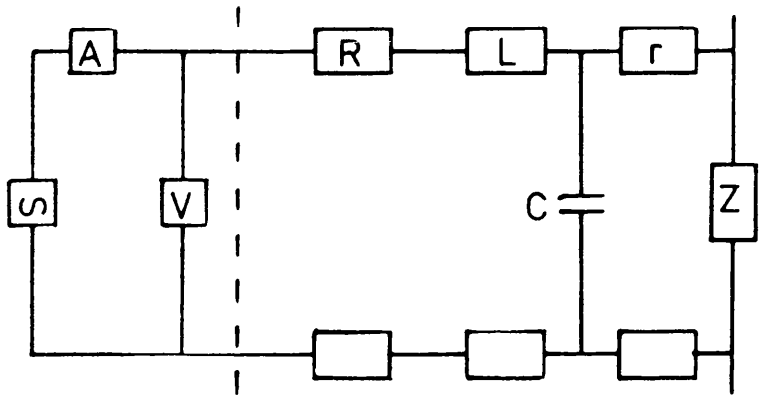

FIGURE 4.17
PROBABLE LEAD IMPEDANCES RESULTING FROM TWO TERMINAL ELECTRICAL MEASUREMENTS.

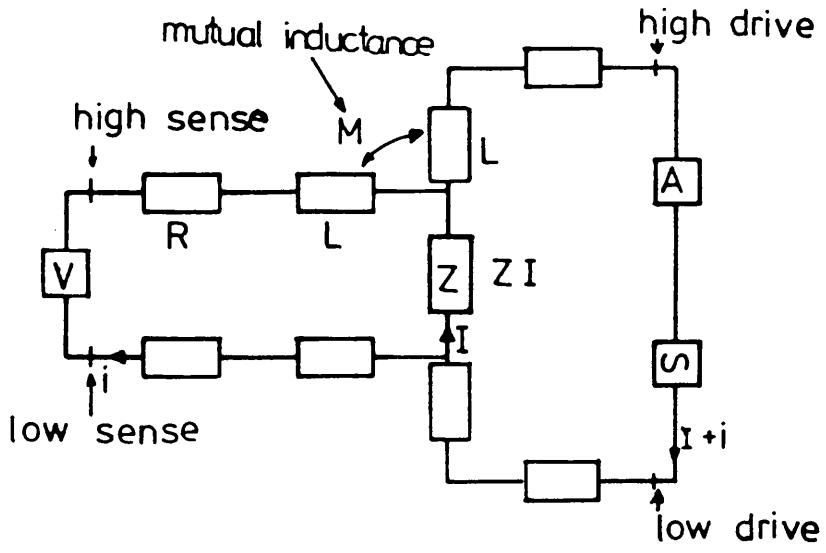

FIGURE 4.18
THE LEAD IMPEDANCES INHERENT IN THE FOUR TERMINAL METHOD, INCLUDING THE MUTUAL INDUCTANCE EFFECTS.

frequency measurements.

The mutual inductance will effect the measurement accuracy when the unknown impedance is very low (less than 10Ω), and when the test signal frequency is high. This error may be reduced if the drive and sense leads can be twisted together, though this still leaves the system prone to externally generated noise. Both of the disadvantages that are associated with the four terminal method are eliminated by using coaxial cables as the measurement leads, termed a four terminal pair. Current is supplied through the inner conductor and returns through the outer, thus avoiding the generation of a magnetic field around the cables and negating the concern for mutually induced EMF's. The cables outer conductor also acts as a shield, reducing the sensitivity to externally generated noise.

The four terminal pair must at some point revert to a two terminal configuration if the unknown impedance has a two terminal format. The four terminal pair technique has been used here in the Hewlett Packard 4192 impedance analyser which forms the central component of the measurement system (section 4.6).

CHAPTER 5 RESULTS AND ANALYSIS

Section 5.1 INTRODUCTION

The data presented in this thesis were obtained using two different bridge techniques: a) single frequency measurements (historically the first investigation, using a Wayne Kerr Bridge), b) multi frequency measurements to obtain a complex impedance profile. These two techniques have been employed to measure the electrical properties of uranium dioxide under a wide range of experimental conditions: temperatures from 1700K to 4.2K, pressures between 25Kbar and 70Kbar. The results of these measurements will be introduced and analysed in this chapter.

NOTE All conductivities quoted in this chapter are quoted in $\Omega^{-1}m^{-1}$.

Section 5.2 LOW TEMPERATURE MEASUREMENTS BETWEEN 293K AND 77K

Section 5.21 SINGLE FREQUENCY MEASUREMENTS

Single frequency measurements were made on both single crystal and polycrystalline material, using the Wayne Kerr bridge (section 4.21). Figures 5.1 and 5.2 show the temperature dependences of the conductivity and

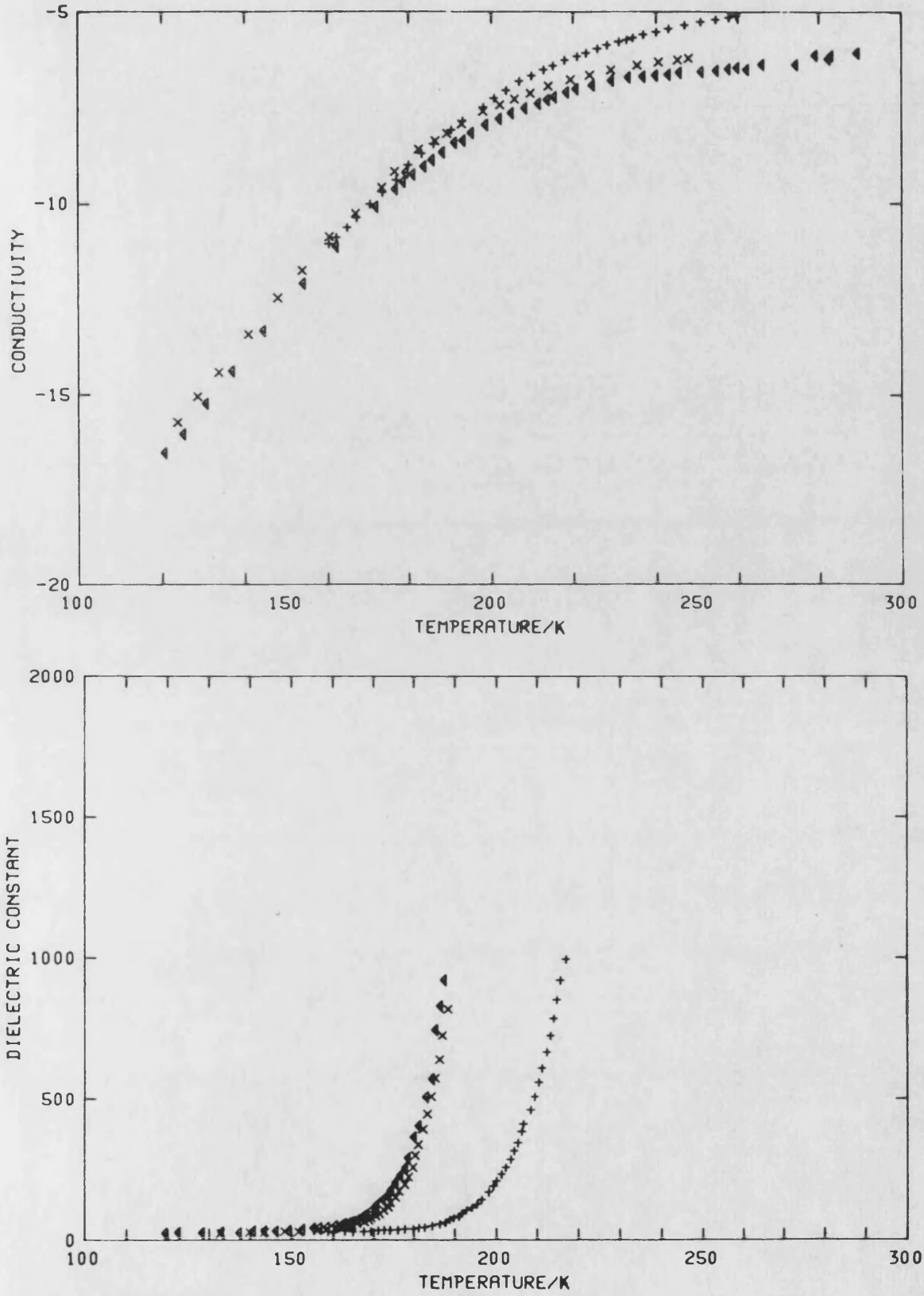

FIGURE 5.1
ELECTRICAL CONDUCTIVITY (TOP) AND DIELECTRIC CONSTANT (BOTTOM) AS A FUNCTION OF TEMPERATURE FOR SELECTED MEASUREMENT FREQUENCIES (+ 10KHz, × 2KHz AND ◁ 1KHz) FOR SINGLE CRYSTAL MATERIAL.

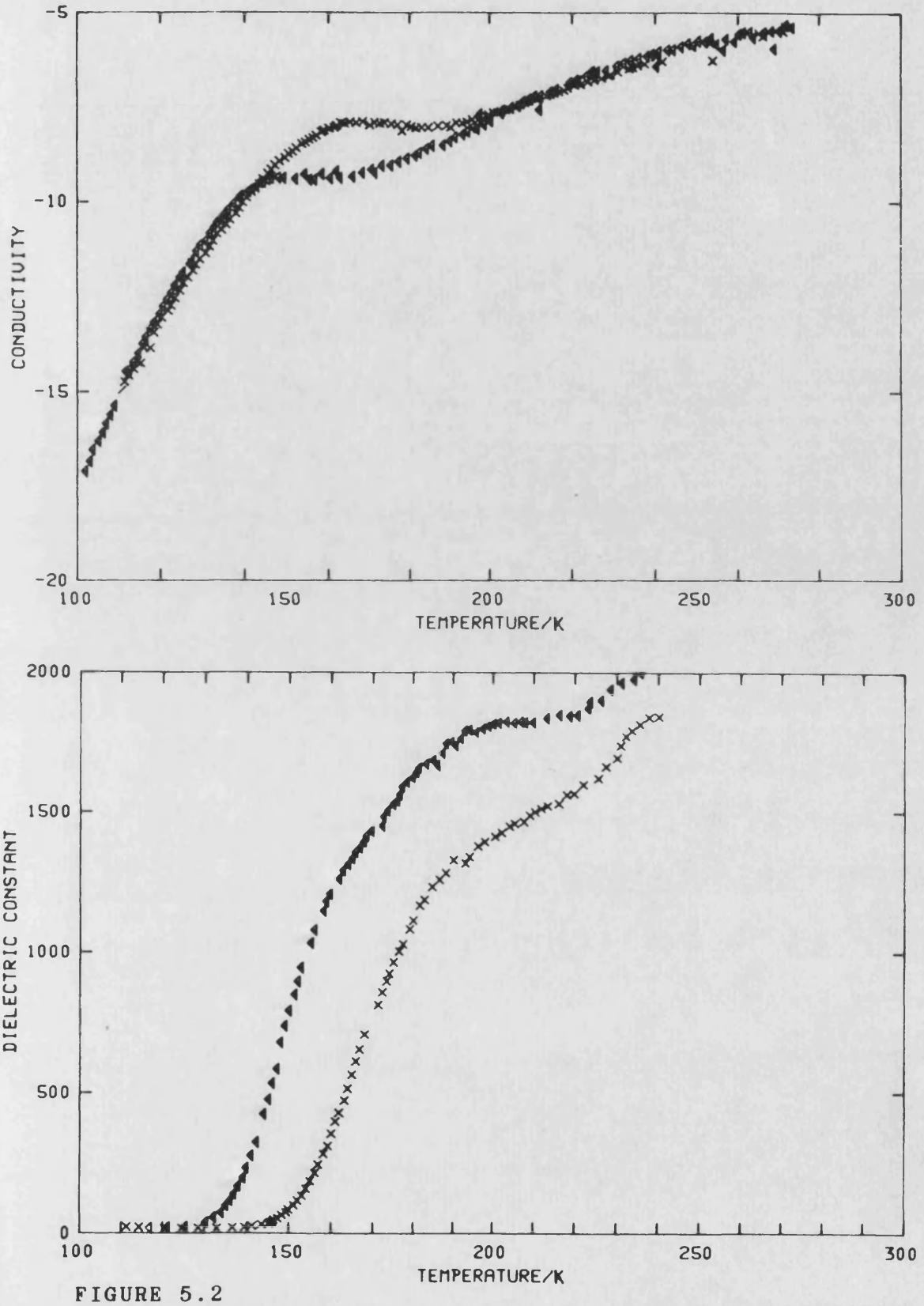

FIGURE 5.2
ELECTRICAL CONDUCTIVITY (TOP) AND DIELECTRIC CONSTANT (BOTTOM) AS A FUNCTION OF TEMPERATURE FOR SELECTED MEASUREMENT FREQUENCIES (× 10KHz AND ◁ 2KHz) FOR POLYCRYSTALLINE MATERIAL.

dielectric constant obtained for both material types. The conductivity and dielectric constant data for polycrystalline material both exhibited a 'hump' at approximately the same temperature (190K to 140K), which was not present in the single crystal data. The shape and temperature of this feature was dependent upon the measurement frequency; unfortunately it was difficult to assess precisely the temperature at which this feature occurred from the conductity plots.

It has been common practice to analyse conductivity data for uranium dioxide using Arrhenius plots ($\log_e \sigma$ vs 1/T : band conduction model), thus allowing an activation energy to be calculated. An alternative approach on the basis of a small polaron model, used a similar representation ($\log_e \sigma T$ vs 1/T) to calculate an activation energy. Both types of Arrhenius plots were compared (figure 5.3) to assess whether one of the models was more applicable than the other. In fact no marked differences in linearity were found in the plots. Hence this conductivity data could not be used to distinguish between the applicability of either model to uranium dioxide. Activation energies were obtained from the linear portions of the curves, for a band conduction model (table 5.1). These activation energies were found to be independent of the frequency of measurement. The Arrhenius plots obtained for polycrystalline material clearly showed two linear regions above and below the

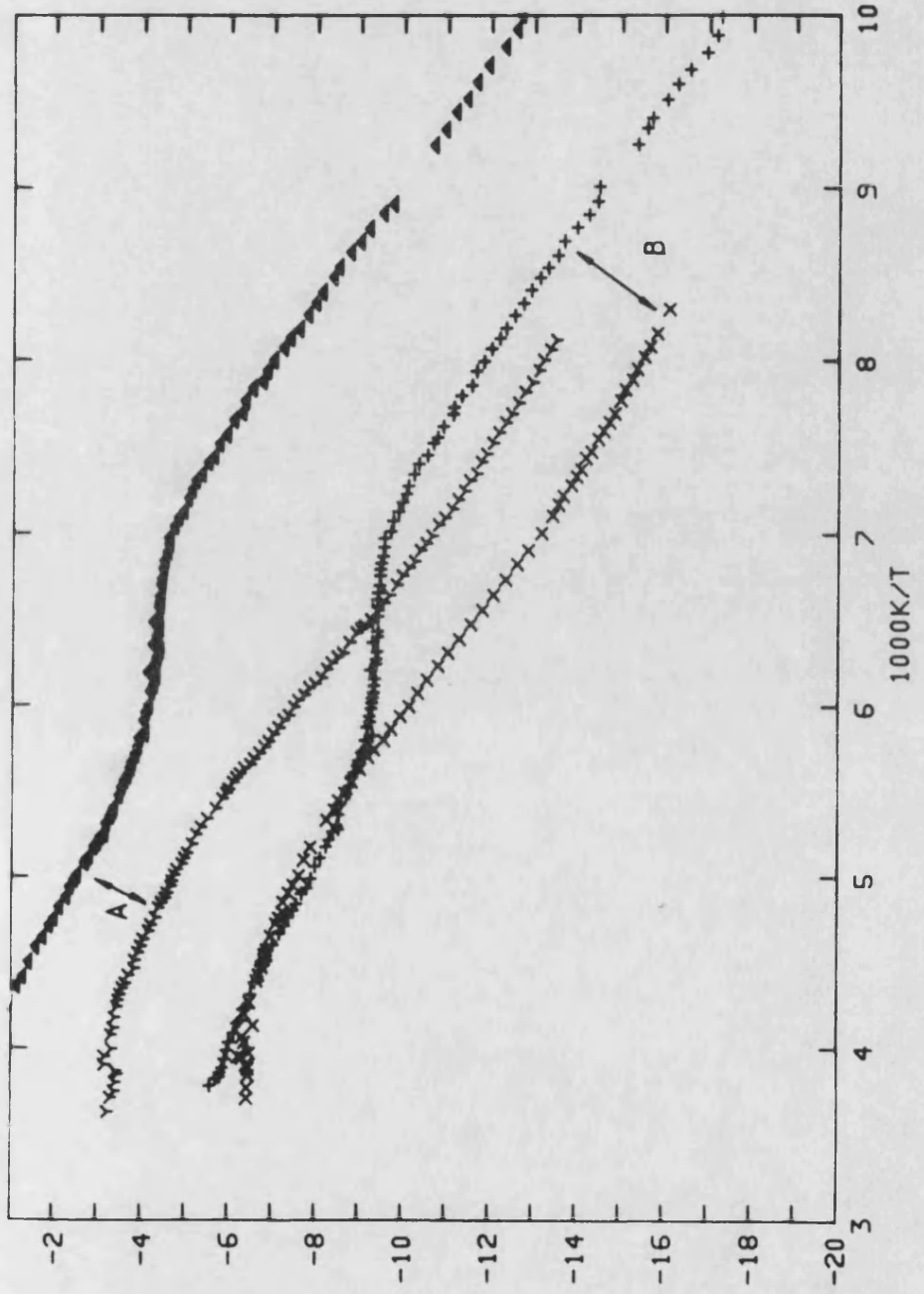

FIGURE 5.3

ARRHENIUS PLOTS OF THE CONDUCTIVITY (A LN(σT) vs 1/T AND B LN(σ) vs 1/T) FOR MONOCRYSTALLINE ($\triangle$ AND Y) AND POLYCRYSTALLINE ($\times$ AND +) MATERIAL. THE DATA HAD BEEN CALCULATED FROM THE 2KHz SINGLE FREQUENCY DATA (FIGURES 5.1 AND 5.2).

TABLE 5.1 ACTIVATION ENERGIES FOR POLYCRYSTALLINE AND SINGLE CRYSTAL URANIA CALCULATED FROM SINGLE FREQUENCY MEASUREMENTS ON THE BASIS OF A BAND CONDUCTION MODEL.

SINGLE CRYSTAL MATERIAL		POLYCRYSTALLINE MATERIAL	
ACTIVATION ENERGY/eV	PRE-FACTOR $/\Omega^{-1}m^{-1}$	ACTIVATION ENERGY/eV	PRE-FACTOR $/\Omega^{-1}m^{-1}$
0.22	123	# 0.18	13
		$ 0.22	4770

REGION ABOVE THE HUMP

$ REGION BELOW THE HUMP

hump. The Arrhenius plots allowed the hump temperature to be estimated in a more satisfactory manner than was possible directly from figure 5.2. This enabled the frequency dependence of the hump to be assessed (figure 5.4); an activation energy (E_p=0.16 eV) for the process responsible was then calculated using

$$f_p = f_o \exp(-E_p/kT) \qquad 5.1$$

The activation energies for conduction of the single crystal material and for polycrystalline material in the region below the hump were the same within experimental error. Both of these energies were slightly larger than the activation energy for the region above the hump obtained for polycrystalline material.

The capacitance measured at high temperatures (293K) was found to be extraordinarily large and implied a dielectric constant of 2000: approximately 100 times too big. However the measured capacitance decreased rapidly with temperature; limiting values of the dielectric constant, independent of frequency up to 10KHz, were reached for all samples when the temperature was reduced below about 130K (figures 5.1 and 5.2). The limiting values were 25.5 and 22.8 for single crystal and polycrystalline material respectively at 120K; these values were consistent with static dielectric constants obtained by other workers (table 2.4). The temperatures at which the limiting values were obtained increased with measurement frequency and were generally lower for

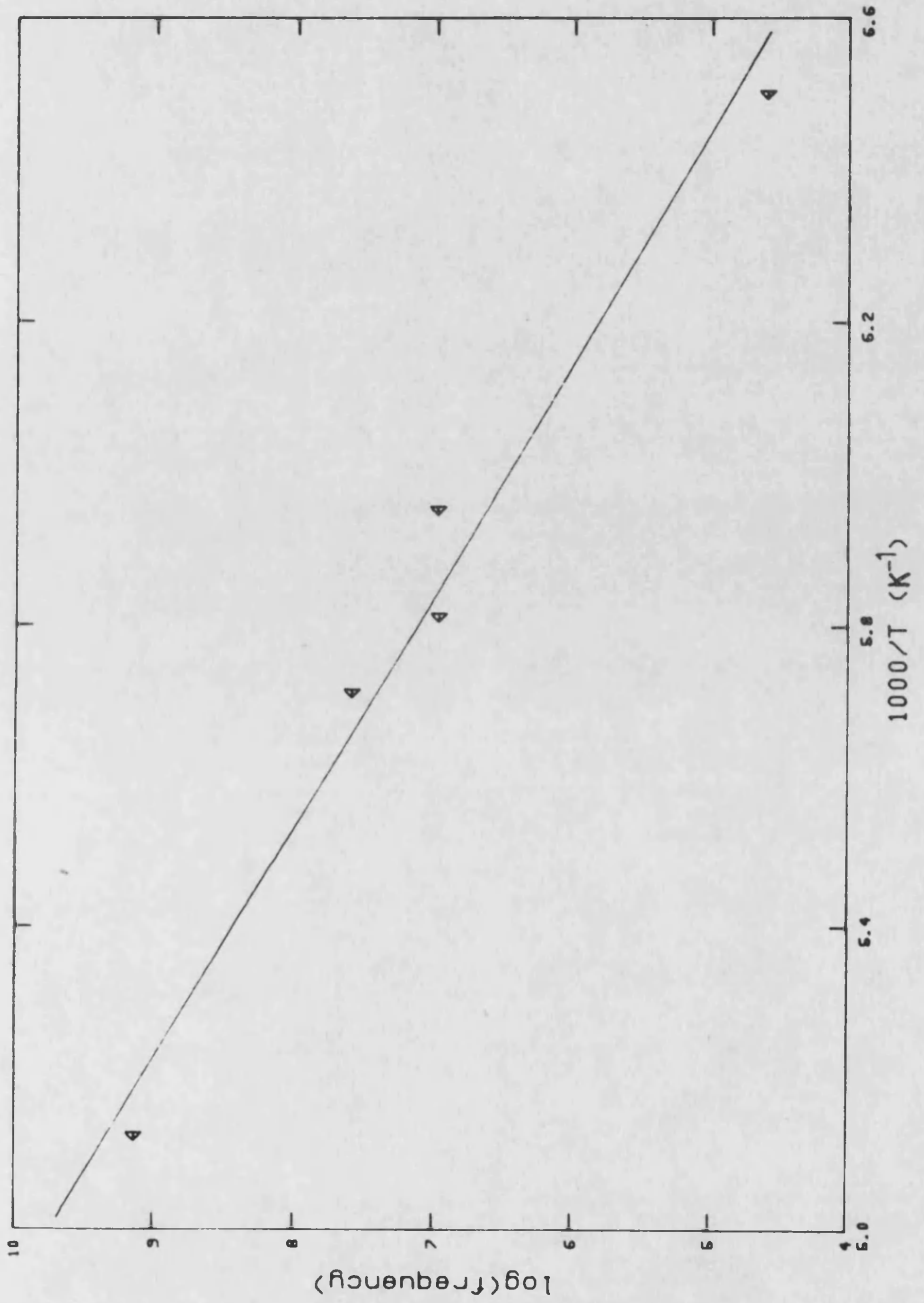

FIGURE 5.4

PLOT OF THE MEASUREMENT FREQUENCY VERSUS INVERSE PEAK TEMPERATURE CALCULATED FROM THE CONDUCTIVITY DATA FOR POLYCRYSTALLINE MATERIAL (FIGURE 5.2).

polycrystalline material. The smaller value of the polycrystalline dielectric constant could not be ascribed definitively to the sample porosity (section 2.3) as this quantity was not known for this material. However using the data of Huntley (figure 2.18) the amount of porosity that would account for the observed dielectric constant difference (25.5-22.8) was estimated at 10%: the density of the polycrystalline samples was approximately 5% lower than for the single crystal (Degussa) sample.

Section 5.22 IMPEDANCE PROFILE MEASUREMENTS

a) SINGLE CRYSTAL MATERIAL

Multi-frequency measurements, over the same temperature range as that used in section 5.21, were made on single crystal material. Impedance profiles (figure 5.5) were obtained from these measurements at selected measurement temperatures. The data clearly showed that the frequency range available was not sufficient to traverse fully the impedance profile. However, thermal activation of the network components altered the characteristic frequencies of the network sufficiently to enable different portions of the profile to be traversed at different temperatures. This procedure allowed the whole of the profile to be identified as two connected semicircular arcs (figure

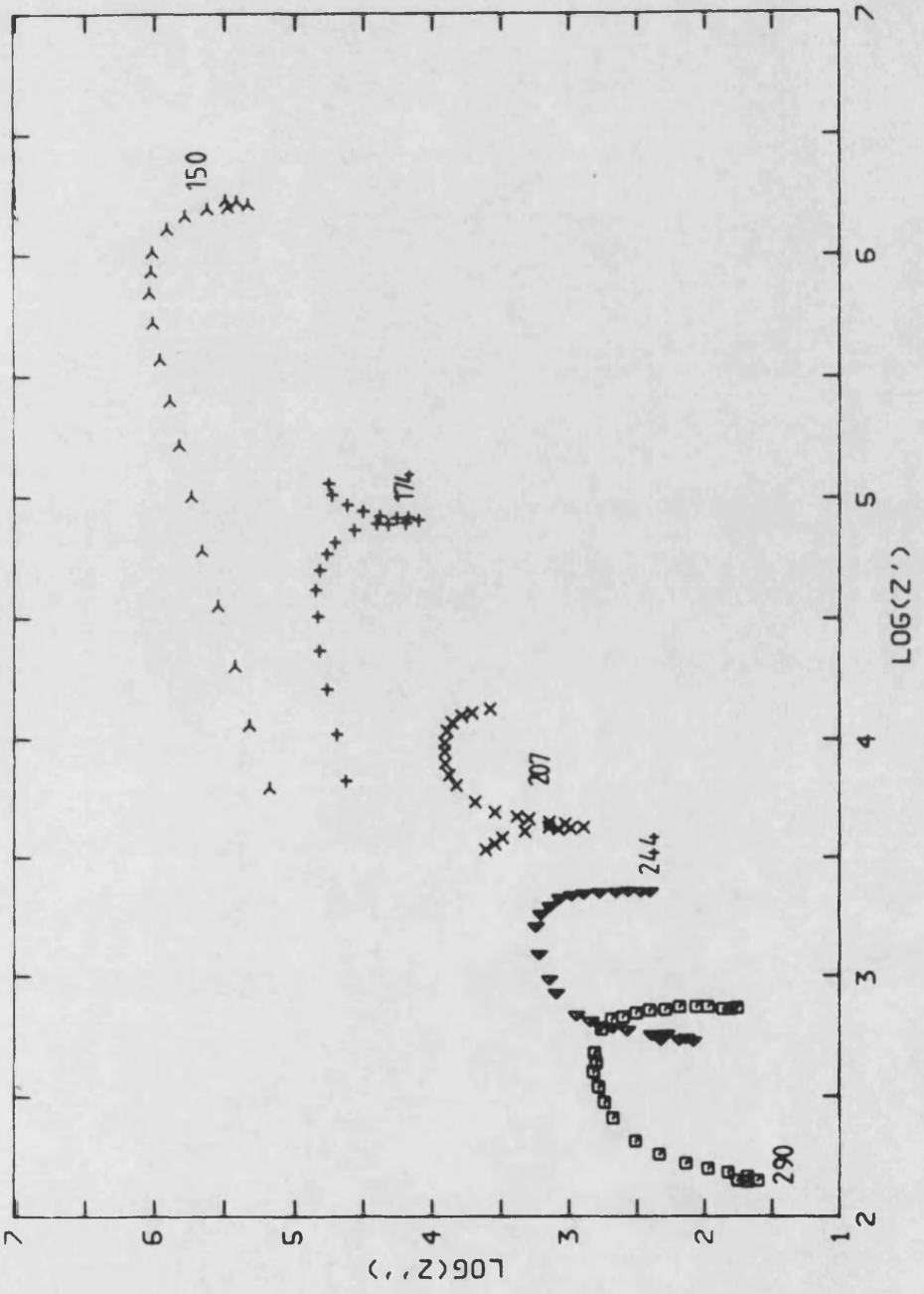

FIGURE 5.5

IMPEDANCE PROFILES FOR SINGLE CRYSTAL MATERIAL, WITHIN THE FREQUENCY RANGE (10Hz TO 10MHz), AT SELECTED MEASUREMENT TEMPERATURES (□ 290K, ◁ 244K, × 207K, + 174K AND ≻ 150K).

3.7) in the complex impedance plane. Impedance data obtained in this way, at several selected constant voltages, identified a voltage dependence that was associated with the low frequency data but was not present in the high frequency data. In addition inversion of the data into the complex admittance plane produced straight line profiles (following the procedure of Jonscher and Reau 1978), thus confirming that the components were connected in parallel. The most probable equivalent circuit responsible for the impedance profiles was identified as two parallel combinations of conductances (G=1/R) and capacitances (C) connected in series (section 3.3). Such an equivalent circuit has been shown to represent the physical situation of a narrow boundary layer existing in conjunction with a bulk conducting region (Jonscher 1983). The electrical properties of such a boundary region have commonly been found to be voltage dependent. Identification of this equivalent circuit enabled for the extraction of the individual circuit components (figure 3.7). The temperature dependences of the components were established (figure 5.6) by analysing the profiles that were obtained at different temperatures.

The conductances of the two regions have been analysed by an Arrhenius technique and both show linearity over the whole temperature range for which

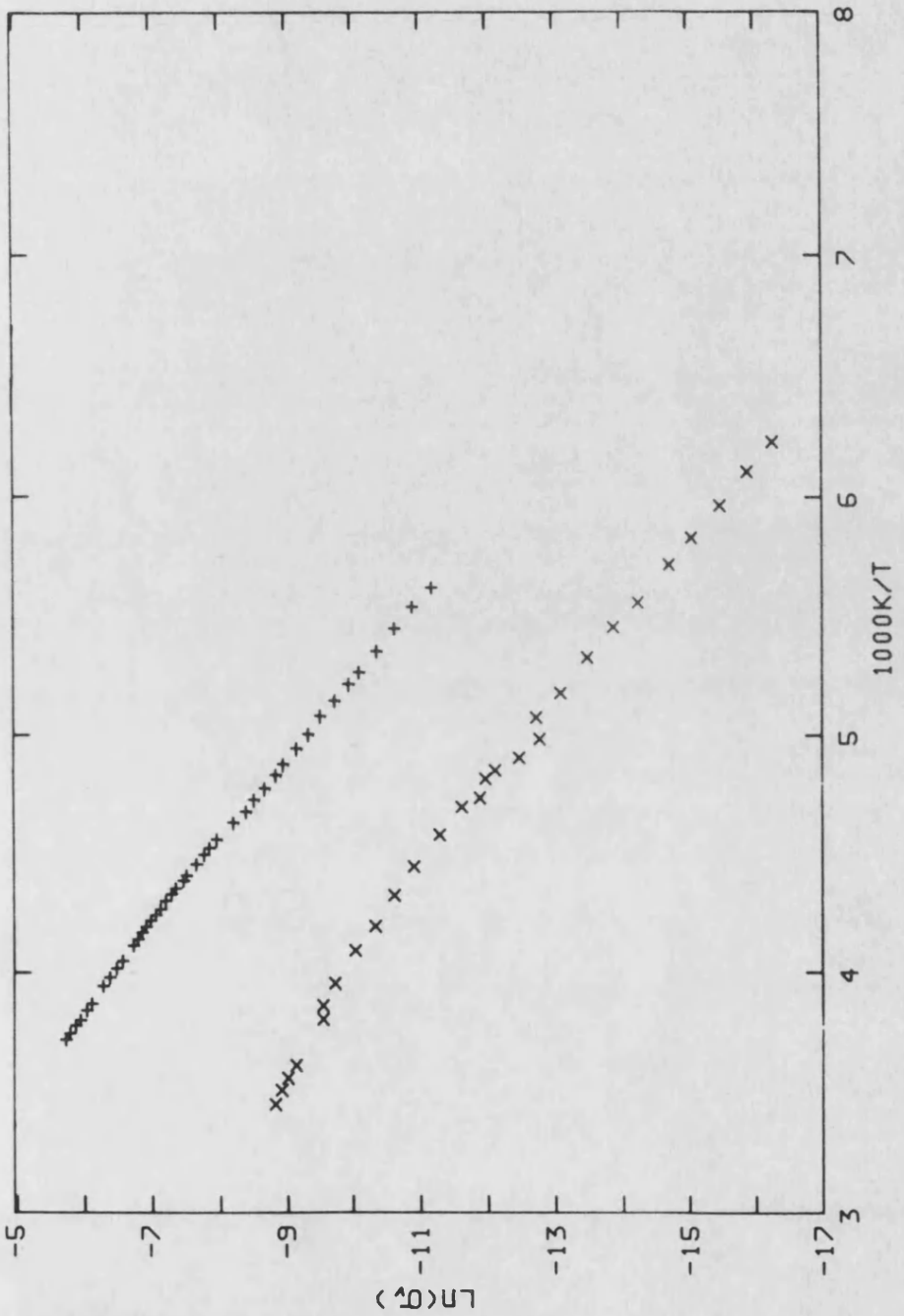

FIGURE 5.6 A)

VOLUME CONDUCTIVITY OF SINGLE CRYSTAL MATERIAL (+ NORTON AND × DEGUSSA), CALCULATED FROM THE IMPEDANCE PROFILES IN ARRHENIUS FORMAT.

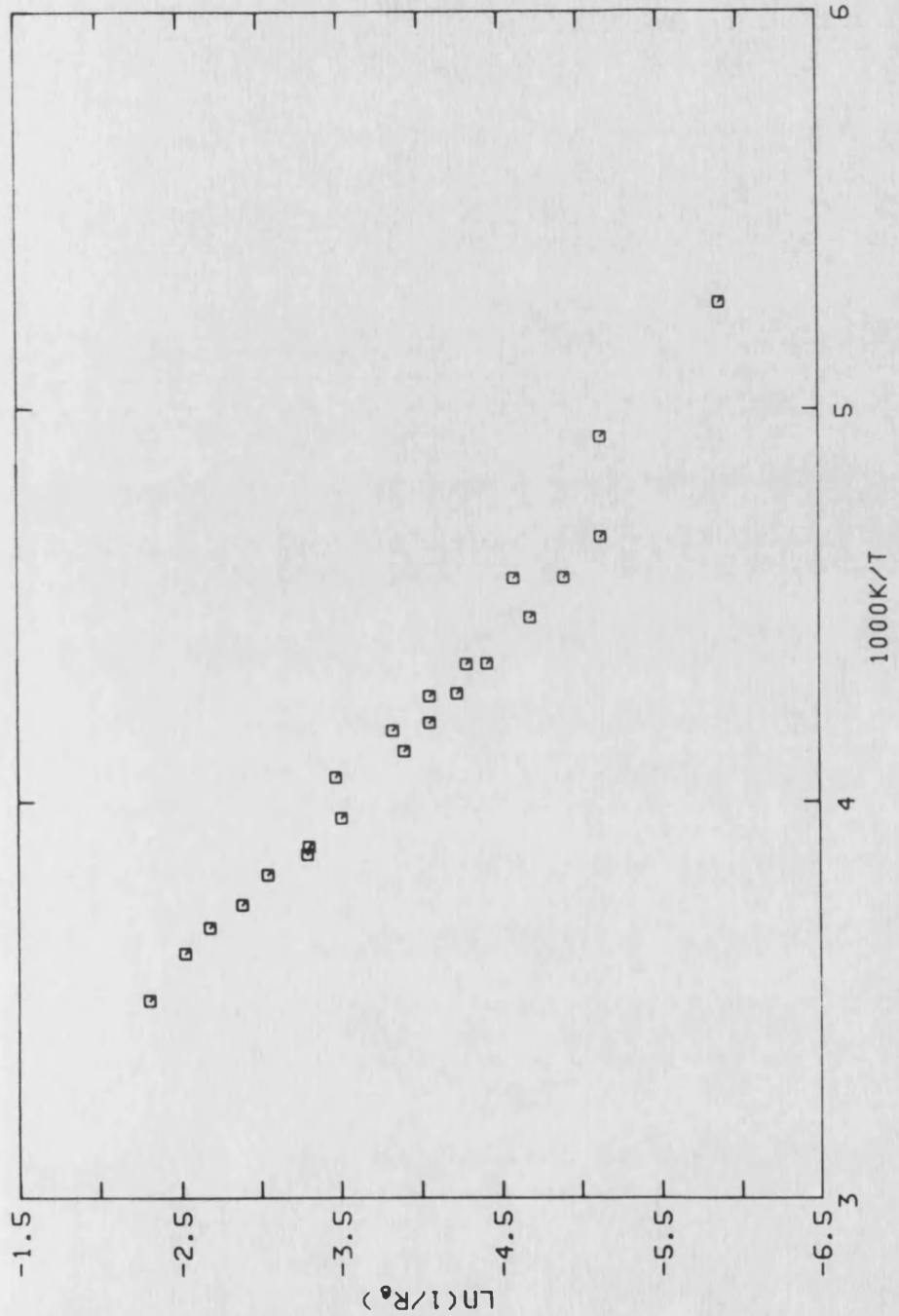

FIGURE 5.6 B)

THE RECIPROCAL OF THE BOUNDARY LAYER RESISTANCE IN ARRHENIUS FORMAT FOR SINGLE CRYSTAL MATERIAL (SUPPLIED BY NORTON RESEARCH), AT AN APPLIED VOLTAGE OF 1V.

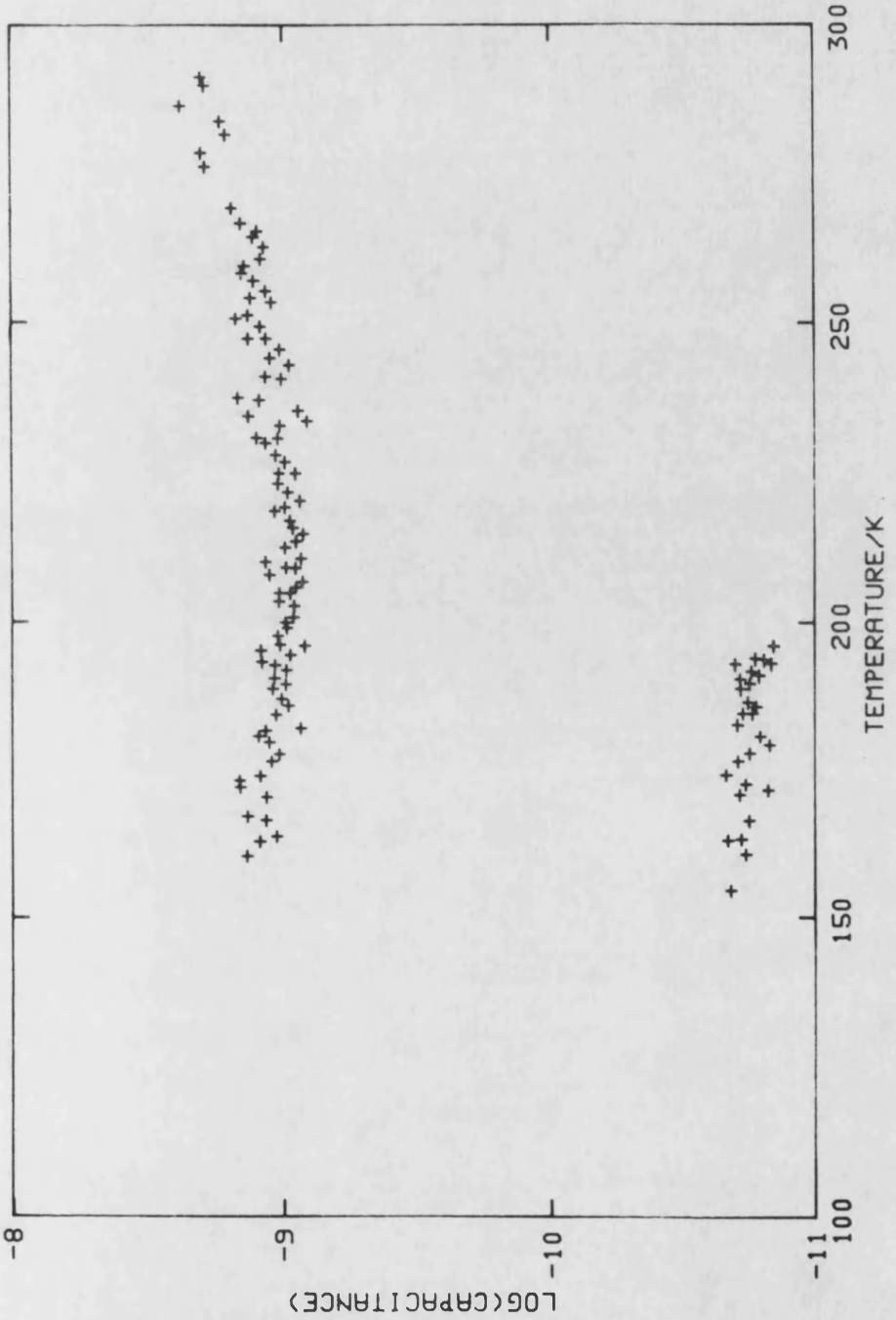

FIGURE 5.6 C)

THE TEMPERATURE DEPENDENCE OF THE BULK CAPACITANCE (LOW VALUES) AND THE BOUNDARY CAPACITANCE (HIGH VALUES) OF SINGLE CRYSTAL (DEGUSSA) MATERIAL, AT AN APPLIED VOLTAGE OF 1V.

impedance data was available. The activation energies, for both regions, were calculated on the basis of band conduction and small polaron models, table 5.2. The activation energy for the bulk region was the same as those (table 5.1) calculated, from single frequency measurements, for single crystal and polycrystalline (below the hump) material. The boundary activation energy was the same as the activation energy previously calculated above the hump for polycrystalline material. A conductivity prefactor was calculated for the bulk region; whereas a single prefactor was not calculated for the boundary layer as the conductivity prefactors in this layer were voltage dependent, thus a prefactor ($1/R_o$) was calculated at a voltage of 1V for the boundary layer (the activation energies for the boundary layer were voltage independent). Table 5.2 shows that the conductivity prefactor for the crystals manufactured by Norton Research was approximately a factor of ten larger than the prefactor for the samples from Degussa. This enhanced conductivity was attributed to a more defective nature of the Norton material rather than any stoichiometric effects. The supposition of a more defective structure was supported by the poor mechanical properties of the these Norton samples.

The capacitance data (figure 5.6(c)) was found to be clearly divided into two regions: I) high (boundary) capacitance at high temperatures, II) low (bulk)

TABLE 5.2 ACTIVATION PARAMETERS FOR SINGLE CRYSTAL URANIA CALCULATED FROM IMPEDANCE PROFILE DATA, ON THE BASIS OF BOTH BAND CONDUCTION AND SMALL POLARON MODELS.

MODEL		PRE-FACTOR	ACTIVATION ENERGY/eV
		BULK CRYSTAL	
#BAND	*	34.6±4.6	0.228±0.003
CONDUCTION	+	2.85±0.14	0.244±0.001
$SMALL	*	6844±881	0.246±0.003
POLARON	+	572±40	0.262±0.002
		BOUNDARY LAYER	
##BAND	*	5.499±0.324	0.178±0.05
CONDUCTION	+	1.127±0.05	0.192±0.019
$$SMALL	*	3492±206	0.196±0.005
POLARON	+	698±31	0.212±0.021

* CRYSTALS SUPPLIED BY NORTON RESEARCH: A/l=0.21214m

+ CRYSTALS SUPPLIED BY DEGUSSA: A/l=6.115*10^{-2}m

PREFACTOR DIMENSIONS $\Omega^{-1}m^{-1}$, $ PREFACTOR DIMENSIONS $\Omega^{-1}m^{-1}K$

PREFACTOR DIMENSIONS Ω^{-1}, $$ PREFACTOR DIMENSIONS $\Omega^{-1}K$

NOTE:- BOUNDARY LAYER PREFACTORS ARE CONDUCTANCES NOT CONDUCTIVITIES

capacitance at low temperatures. The data indicated that, within the frequency range of the instrument, a large value of the capacitance for example was measured at high temperatures (figure 5.2). In the temperature region where both boundary and bulk values were exhibited, the predominant capacitance depended upon the frequency of measurement ie a low capacitance would be measured at high frequencies. Dielectric constants were calculated using the physical dimensions of the sample; the low (bulk) capacitance values produced dielectric constants of approximately 36. However the large (boundary) values of capacitance indicated extremely large dielectric constant values, similar to those given at high temperatures by single frequency measurements. The high capacitance values were associated with the narrow boundary adjacent to a bulk conducting region, thus it was clear that the sample dimensions were not the correct ones to use when evaluating the dielectric constant associated with the large capacitance values. Further support for this explanation was provided by the ratios of the boundary to bulk capacitances and the room temperature to low temperature dielectric constants; each of these ratios was the same, being approximately 100.

The thickness of rectifying barriers on reduced rutile (TiO_2) were measured by English and Gossick (1963), by examination of the voltage dependence of the

barrier capacitance. The procedure was to plot the reciprocal of the square of the capacitance per unit area against the voltage applied to the boundary layer. The intercepts of this plot with the capacitance and voltage axes were used to calculate the barrier voltage and thickness, according to a postulated model for the barrier. Unfortunately this method only worked well for data with a linear capacitance against voltage profile. The capacitance-voltage profile for uranium dioxide was not linear. An alternative procedure was to plot the donor concentration ($(2/\epsilon q)dV/dC^{-2}$), calculated from the local curvature of the capacitance-voltage plot, against the depth from the boundary (ϵ/C). In the region of the boundary edge the donor concentration should change rapidly and thus allow the determination of the boundary layer thickness. This procedure was adopted here to examine the voltage dependence of the boundary layer capacitance of single crystal material (figure 5.7). These measurements were only made at an ambient temperature of 293K; the temperature dependence of the boundary layer was not investigated due to problems of temperature stability during the large number of measurements that were necessary (1600 per voltage point, approximately). The thickness of the boundary layer was estimated as 600Å; this dimension allowed the boundary layer dielectric constant to be calculated as approximately 33, and its conductivity as $4*10^{-5}\ \Omega^{-1}m^{-1}$.

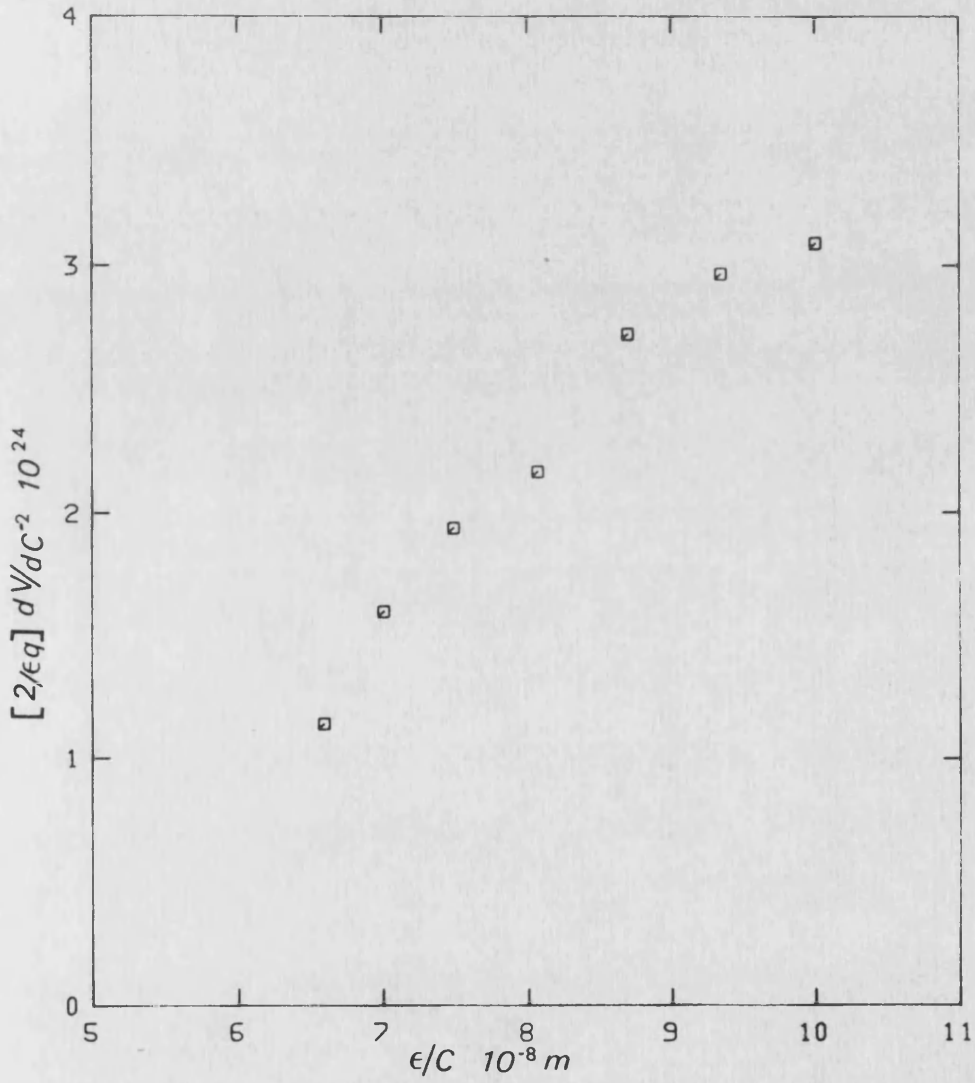

FIGURE 5.7

THE GRADIENT OF THE CAPACITANCE VERSUS VOLTAGE PLOT AGAINST ϵ/C FOR SINGLE CRYSTAL (DEGUSSA) MATERIAL, ENABLING THE BOUNDARY LAYER WIDTH TO BE ASSESSED AS 600Å.

The values of dielectric constant calculated for the bulk and boundary regions (36 and 33) were somewhat larger than the previously accepted values (table 2.4) and those quoted in sections 5.21 and 5.31. The difference (36-25.5=10.5) between the values obtained for the Degussa single crystal was possibly due to dipole effects which arose from increased non-stoichiometry. The magnitude of this dielectric constant difference was analysed on the basis of the Clausius-Mossotti approach (Frohlich 1958), including a local field correction, for dipoles comprised of a hole and an oxygen interstitial.

$$9\Delta\epsilon kT=(\epsilon_\infty+2)4\pi Np^2 \qquad 5.2$$

where p is the assumed dipole moment and N the concentration of dipoles contributing. The measured dielectric constant difference could be accounted for with a deviation from stoichiometry of 0.005. This deviation from stoichiometry was somewhat smaller than that (0.05) indicated by the data of Tateno, 1984, (figure 2.19). A deviation of this magnitude (between 0.005 and 0.05) was well within the limits of the possible excess oxygen concentration in the crystals used to make these measurements. The increased non-stoichiometry was probably due to the time (18 months approximately) between the single frequency measurements and the production of the impedance

profiles: reduction facilities were not routinely available for this work.

b) POLYCRYSTALLINE MATERIAL

Multi-frequency measurements were also carried out on polycrystalline material. The impedance profiles produced were somewhat complicated (figure 5.8) and very sensitive to the measurement temperature, despite the measurements being carried out in the temperature controlled cryostat (section 4.22). The data suffered extensively from the problems of overlapping features (section 3.4), which made the identification of the individual features difficult. The impedance profile was composed of three regions, which were tentatively attributed to a boundary layer, grain boundaries and a bulk region. This assumption was supported by the single frequency dielectric constant work (figure 5.2) which indicated three regions: one more than the single crystal investigations. No definitive voltage dependence of the profiles was observed. Unfortunately it was not possible for the equivalent circuit of these profiles to be positively identified. This was due in part to the large number of possible equivalent circuits and in part to the inconclusive voltage dependence. However one simplistic approach assumed that an extra parallel combination was added to the equivalent circuit that had been identified for the single crystal material. The extra parallel combination was assumed to

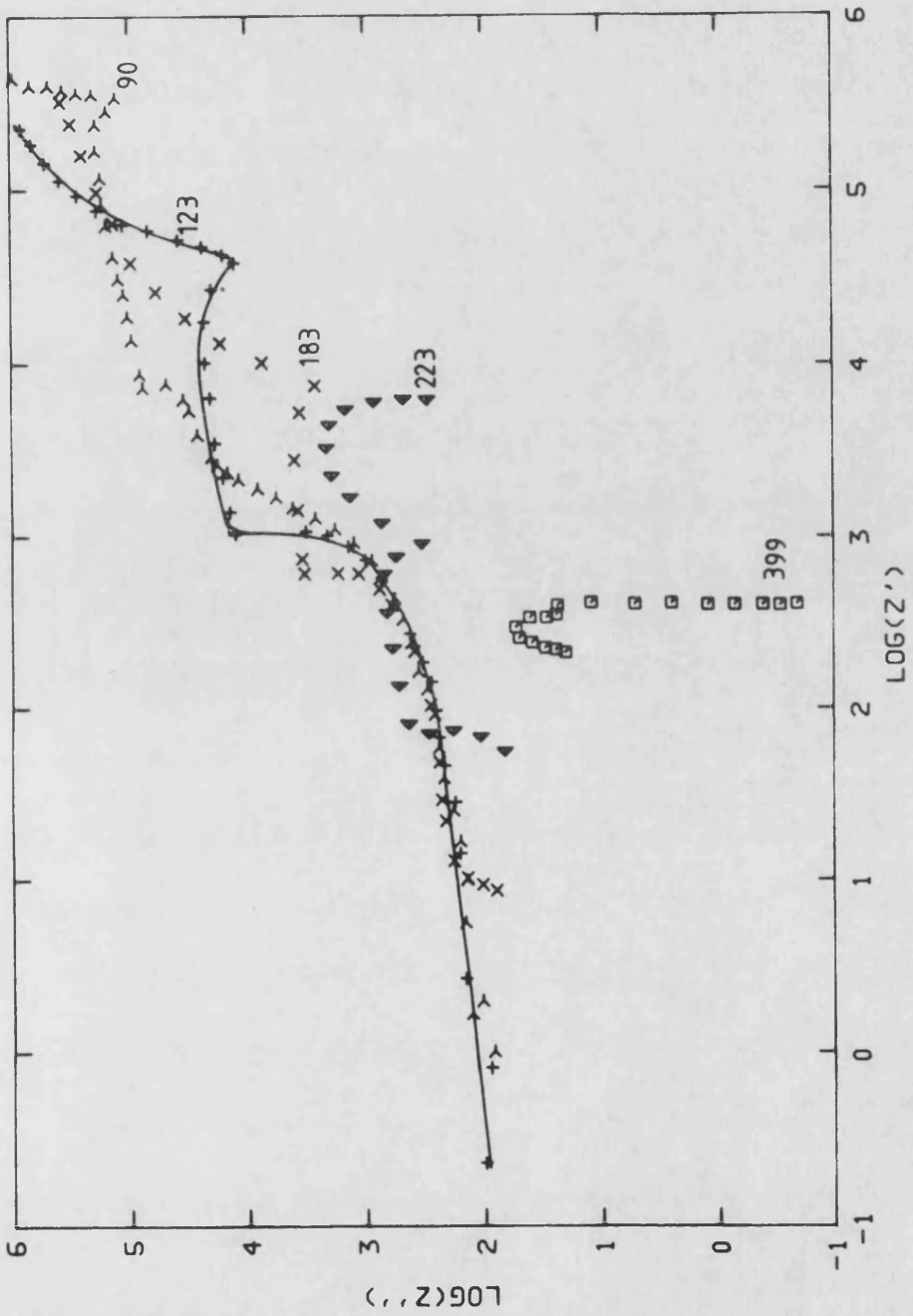

FIGURE 5.8

IMPEDANCE PROFILES FOR POLYCRYSTALLINE MATERIAL AT SELECTED MEASUREMENT TEMPERATURES (□ 399K, ◁ 223K, × 183K, + 123K AND ≻ 90K). THE SOLID LINE SERVES AS A GUIDE TO THE EYE FOR THE DATA OBTAINED AT 123K.

represent the electrical properties of the grain boundaries, in a similar manner to work on scandia stabilized tantala (Stratton et al 1980) and stabilized zirconia (Winnubst et al 1984). Thus the high frequency region was ascribed to the bulk properties, the low frequency region to the boundary layer and the intermediate region to the grain boundaries. The data (figure 5.8) was analysed on the basis of this equivalent circuit; only a few conductances were obtained for each region as the amount of data available was limited (by sample fracture). The conductance data allowed activation energies to be tentatively estimated for two of the three regions: 0.03eV (bulk), 0.07eV (grain boundaries).

Section 5.3 DIELECTRIC CONSTANT STUDIES BELOW 77K

An attempt was made to use multi-frequency techniques to examine the electrical properties of single crystal material at temperatures below the boiling point of liquid nitrogen. However at these temperatures the conductivity of the material was too low to be reliably evaluated: the crystal was effectively an insulator and thus the impedance profile could not be constructed. As an alternative the capacitance of the material (dielectric constant), which could be reliably evaluated, was examined. The data obtained (figure 5.9) showed a very small dependence of the capacitance upon

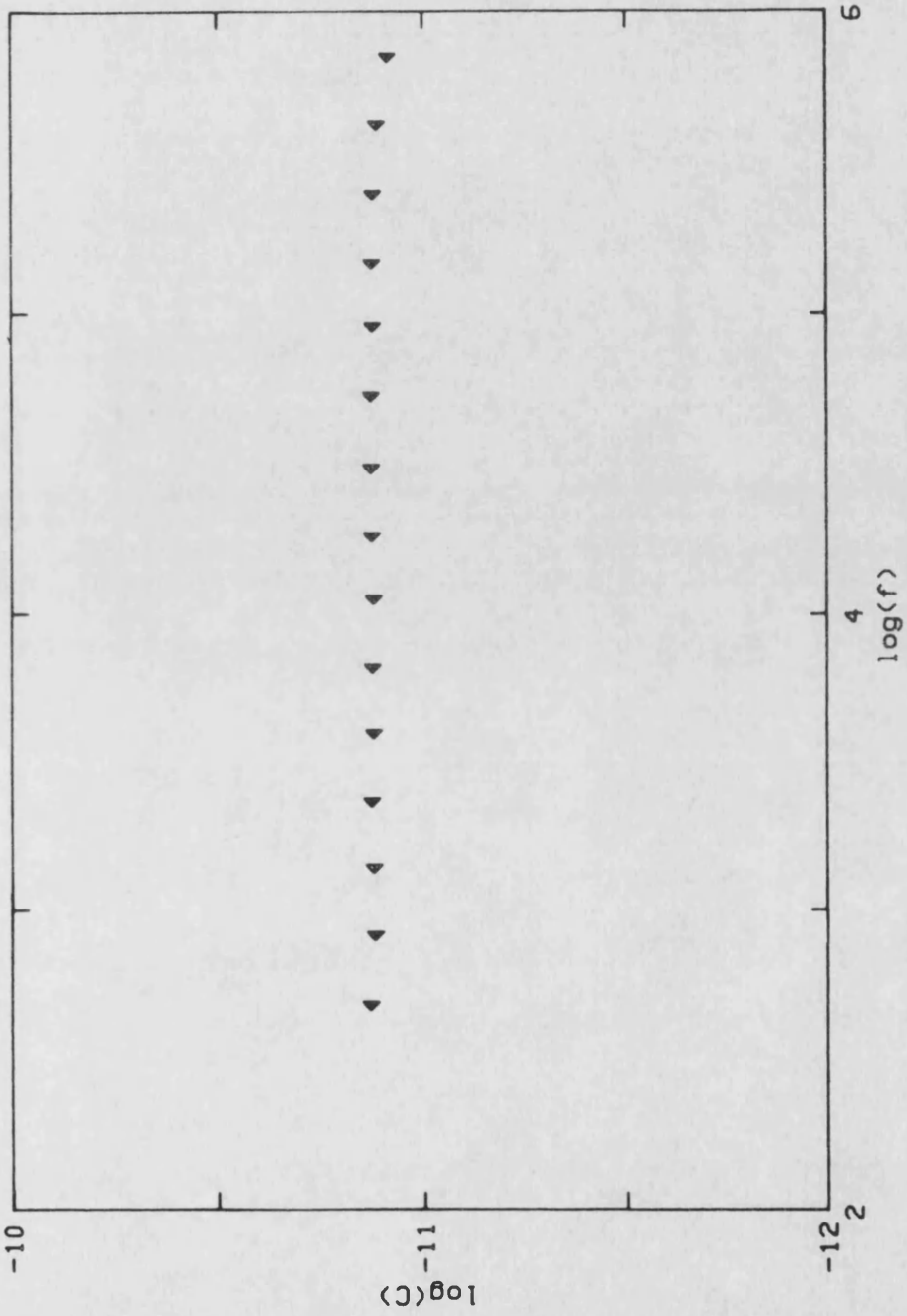

FIGURE 5.9

THE BULK CAPACITANCE AS A FUNCTION OF MEASUREMENT FREQUENCY FOR SINGLE CRYSTAL (DEGUSSA) MATERIAL AT 43K.

the measurement frequency (dC/dF $-3*10^{-19}FHz^{-1}$); this data was used to establish a zero frequency capacitance. The zero frequency capacitance was attributed wholly to the bulk portion of the full equivalent circuit of the material. This assumption was validated in two ways, firstly by calculating the characteristic frequency that would be expected for the bulk region: $79*10^{-3}Hz$ (measurement frequencies were always in excess of this value); secondly by examining the voltage dependence of the data; the data failed to show any such dependence. The dielectric constant of the bulk crystal (calculated from the zero frequency capacitance and the sample dimensions) was obtained at selected temperatures (figure 5.10), both on cooling and on warming. At first sight it seems that there was a certain amount of hysteresis; however this was an experimental artefact because the temperature drifts on cooling and on warming were different, and the larger uncertainty in the temperature on cooling adequately accounted for the apparent hysteresis: the temperature uncertainty on cooling was approximately $\pm$1K, whereas on warming it was $\pm$0.5K.

The prime aim of this particular part of the work was to establish the behaviour of the dielectric constant in the low temperature, antiferromagnetic phase and in the vicinity of the magnetic phase transition. The value of the static dielectric constant within the low

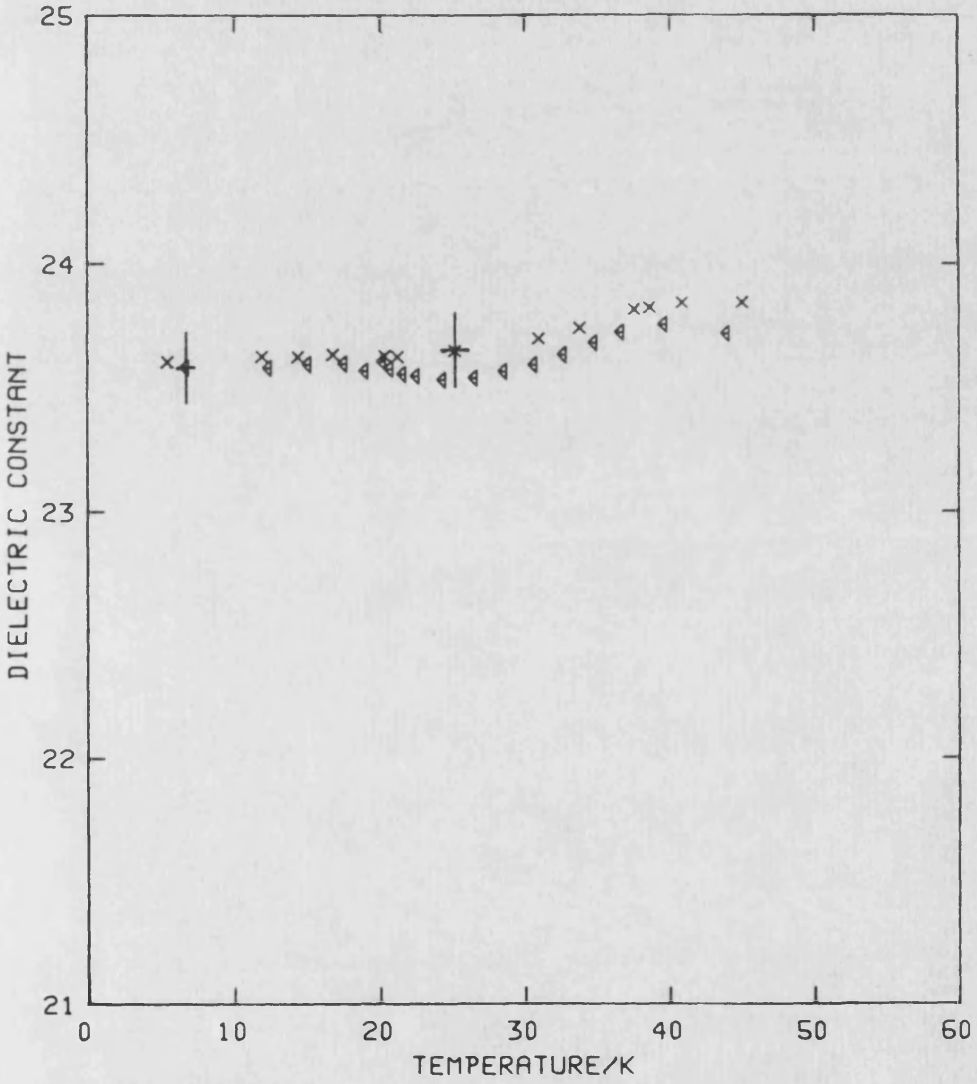

FIGURE 5.10

THE DIELECTRIC CONSTANT, CALCULATED FROM THE ZERO FREQUENCY CAPACITANCE AND THE SAMPLE DIMENSIONS, AS A FUNCTION OF TEMPERATURE (× COOLING AND ◁ WARMING).

temperature phase was determined as 23.6. A value of 23.8 was measured for the low temperature paramagnetic phase (45K).

Thus the effect of the phase transition on the dielectric constant was small but identifiable; the dielectric constant decreased by approximately 0.8% as the sample temperature was reduced. The errors, due to the extrapolation procedure, in the absolute values of the zero frequency dielectric constant were approximately 1%; however the average values of the capacitances ($\bar{C}$), calculated from the data (figure 5.9) over the whole frequency range, displayed a decrease of approximately 0.9%, on cooling through the phase transition. This suggested that the errors on extrapolation only effected the absolute values of the dielectric constant, and that they did not effect the relative change in the dielectric constant at the phase transition: the relative changes in the original and extrapolated values were essentialy the same. The decrease in the dielectric constant was characterised by a broad ransition within the temperature range 37K to 29K; other properties that have been measured through the transition temperature are characterised by a sharp transition temperature (section 2.1).

Section 5.31 THEORETICAL CONSIDERATIONS

The changm in the dielectric constant that would be due to the experimentally observed lattice shear

(section 2.1) was calculated by JH Harding (private communication): the ionic contribution to the dielectric constant was expected to be large as the difference between the static and optic dielectric constants is large (18). These calculations were based on a shell model for UO_2 (Catlow 1977) and used the Harwell PLUTO code (Catlow and Norgett 1976). This enabled the three components of the static dielectric constant (figure 5.11) and the optic dielectric constant to be calculated as functions of the lattice shear (Q). Average values of the three components were then calculated as the sample was anticipated to consist of randomly orientated domains. The averages were for low values of Q ($Q<0.02$), adequately fitted by:-

$$\Delta\epsilon_o/\epsilon_o = 21.6\ Q^2 \qquad 5.3$$

$$\Delta\epsilon_\infty/\epsilon_\infty = 3.85\ Q^2 \qquad 5.4$$

Contributions of this nature indicated that an 0.8% increase in the dielectric constant would occur on cooling through the transition for a displacement of the planes of oxygen atoms of 0.053Å: this was somewhat larger than the observed shear, 0.014Å, (Erdos and Robinson 1983). These calculations clearly predicted a smaller dielectric constant in the paramagnetic phase than in the antiferromagnetic phase, yet the increase was observed when the displacement vanished! A plausible explanation for this would be that the structural phase transition was inhibiting a

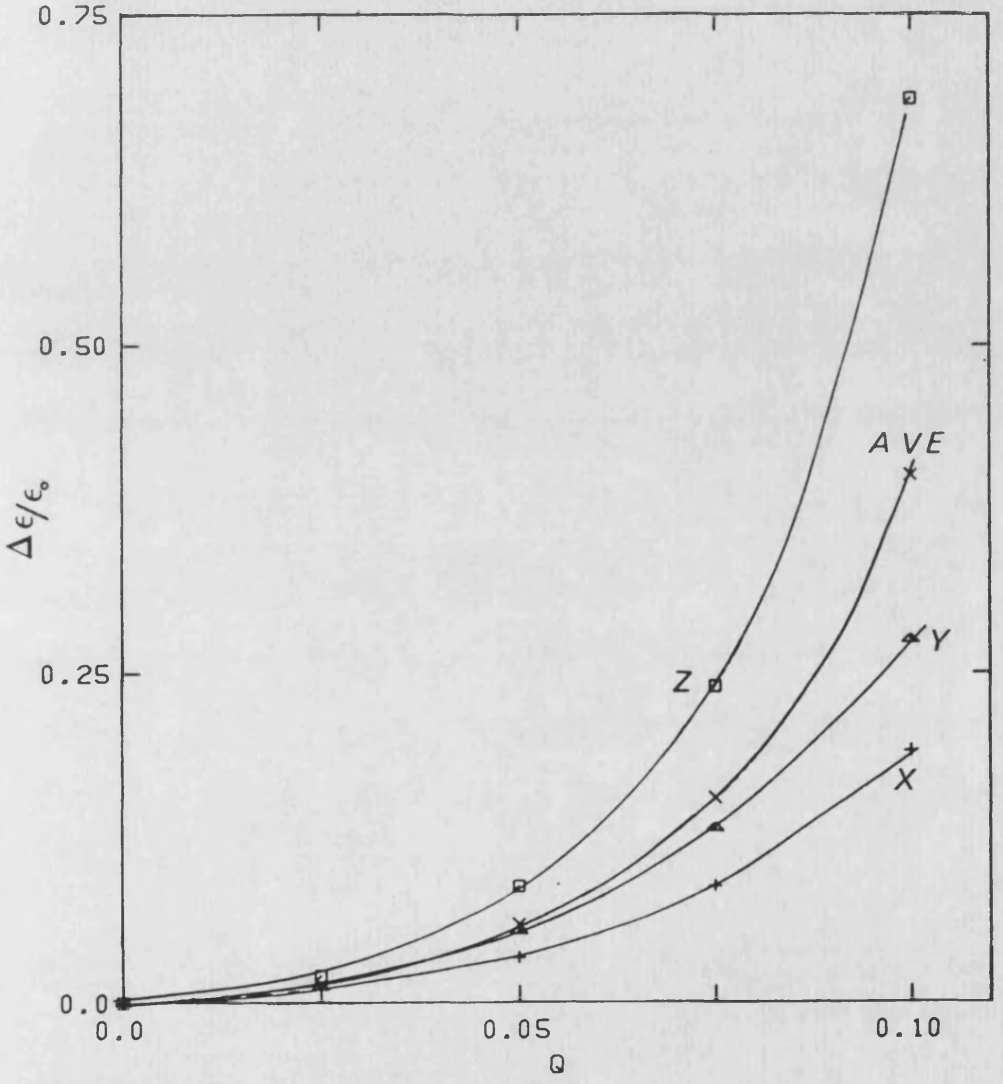

FIGURE 5.11

THE COMPONENTS OF THE STATIC DIELECTRIC CONSTANT, CALCULATED AS A FUNCTION OF THE MAGNITUDE OF THE OXYGEN SHEAR (Q IN UNITS OF THE O-O DISTANCE, 2.7341A) DUE TO HARDING (PRIVATE COMMUNICATION). ORIENTATION OF THE COMPONENTS REFERS TO FIGURE 2.1.

contribution to the dielectric constant. The nature of the contribution was not identified, but it could have been related to the enhanced dielectric constant observed at higher temperatures (section 5.22) which was associated with small deviations from stoichiometry: calculations would not take the effects of these interstitial oxygens into account.

Section 5.4 ELECTRICAL PROPERTIES UNDER HIGH PRESSURES

Electrical impedance measurements were made on small samples of single crystals of UO_2 (section 4.43(a)) using the ac techniques described in chapter 3 and section 4.6. Typical data that were obtained are shown in figure 5.12. Previous electrical measurements on plate geometry samples of UO_2 (section 5.22(a)) had established the presence of a boundary layer. This manifested itself in the equivalent electrical circuit (figure 3.7). The samples used in this work were, of necessity, small (1mm x 1mm x 0.5mm); the earlier work had suggested that for samples of this size and geometry the volume effects would not become wholly dominant until the measurement frequency was in excess of 40MHz (well above that available). Hence the boundary properties dominated the admittance data for frequencies up to 2kHz; thus the equivalent circuit was comprised only of a single parallel combination of capacitance and conductance due to the boundary layer alone.

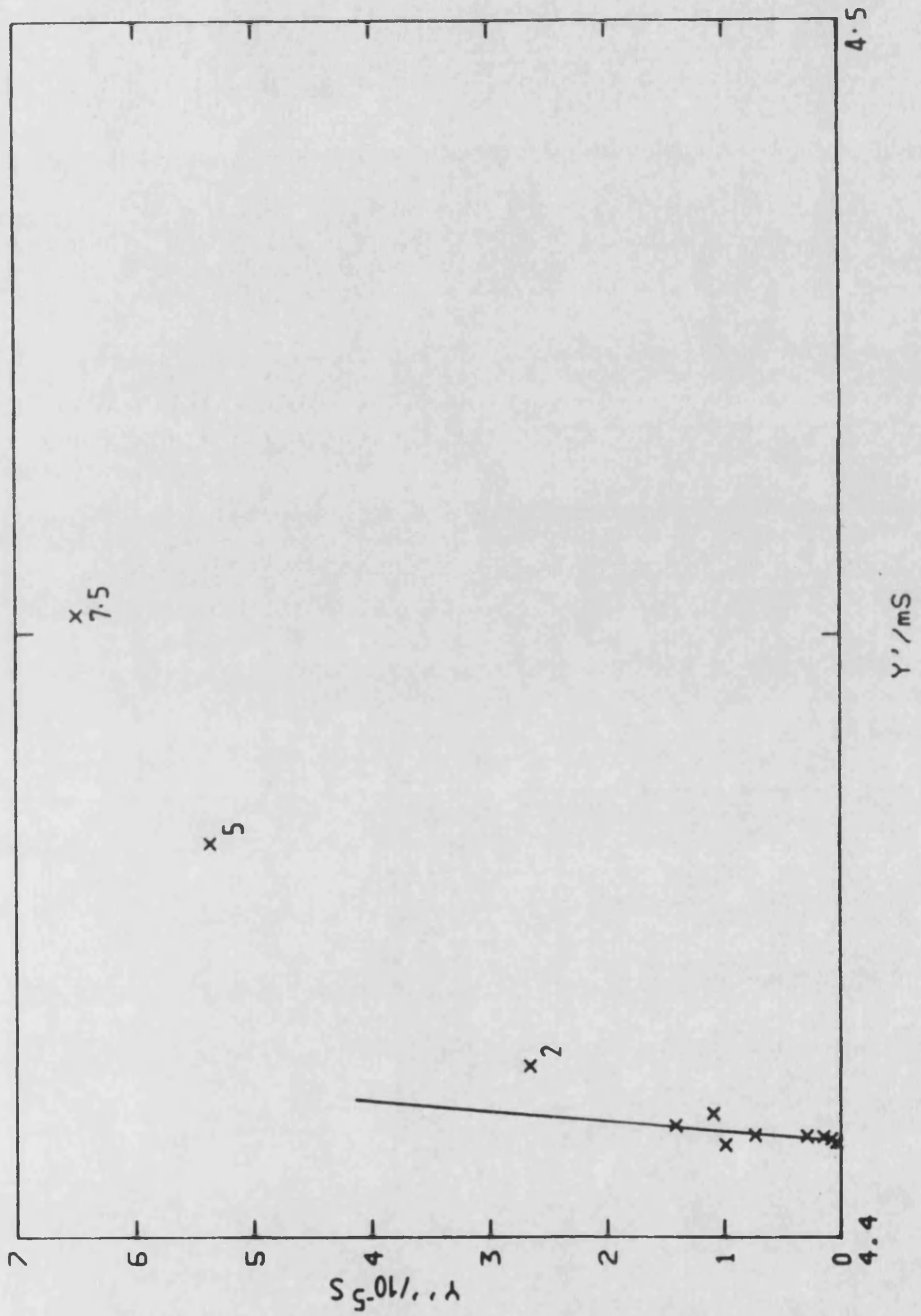

FIGURE 5.12
ADMITTANCE PROFILE OF SINGLE CRYSTAL (NORTON) MATERIAL AT A TEMPERATURE OF 300K AND A PRESSURE OF 70Kbar. THE FIGURES INDICATE THE FREQUENCY (KHz) OF SPECIFIC ADMITTANCE POINTS. THE SOLID LINE SERVES AS A GUIDE TO THE EYE.

Additionally the boundary layer effects contributed extensively to the electrical properties for frequencies up to 2MHz.

Data for a circuit of this form was most conveniently intepreted through the use of its complex admittance, with a plot of Y' against Y" resulting in a straight line, shown schematically in figure 3.14. The data itself (figure 5.12) validated the equivalent circuit that was assumed for low frequencies; contributions from the volume circuit would result in a deviation of the data from a straight line (as is evident for frequencies in excess of 2kHz). The data showed a marked dependence upon the applied test voltage; this was most pronounced at low frequencies; this property has been associated with boundary phenomena (sections 3.5 and 5.22 a)). The inclination of the linear portion of the profile was accounted for by replacing the ideal capacitor in the equivalent circuit with one with a "universal" response (section 3.7).

The dielectric properties were assessed either from the gradient of the admittance profiles, (section 3.7) or directly from the measured capacitance. The capacitance data were acquired through single frequency measurements made on the Wayne Kerr B905 Bridge. Conductance data were not available from these measurements as the frequencies used (100Hz, 1KHz, 2KHz

and 10KHz) straddled the boundary dominant and the mixed boundary-bulk regions causing inconsistent conductance data.

Section 5.41 PRESSURE DEPENDENCE OF THE CONDUCTIVITY

The conductance obtained at an ambient temperature of 300K from these analyses (figure 5.13) showed a sharp increase following the initial application of pressure; this was attributed to the settling of the contacts on the sample and not to any intrinsic behaviour of the material. This contention was supported by the ultrasonic studies of Fritz (1976) where no pressure induced phase transitions were found in UO_2 for pressures up to 20Kbar. The conductance achieved a stable value at a pressure of 30Kbar, beyond which it showed a steady increase with pressure. The dc conductance, previously reported (Vaidya et el 1976), as a function of pressure was qualitatively similar to the ac data presented here; the present measurements gave a value of $6.5\mu SKbar^{-1}$ for dG/dP whereas the previous data, yielded a value of $0.68\mu SKbar^{-1}$.

Section 5.42 PRESSURE DEPENDENCE OF THE DIELECTRIC CONSTANT

The dielectric constant was calculated as a function of frequency at selected pressures (figure 5.14) directly from measurements of the sample capacitance, using the known sample dimensions. The capacitance values did not display any of the inconsistencies

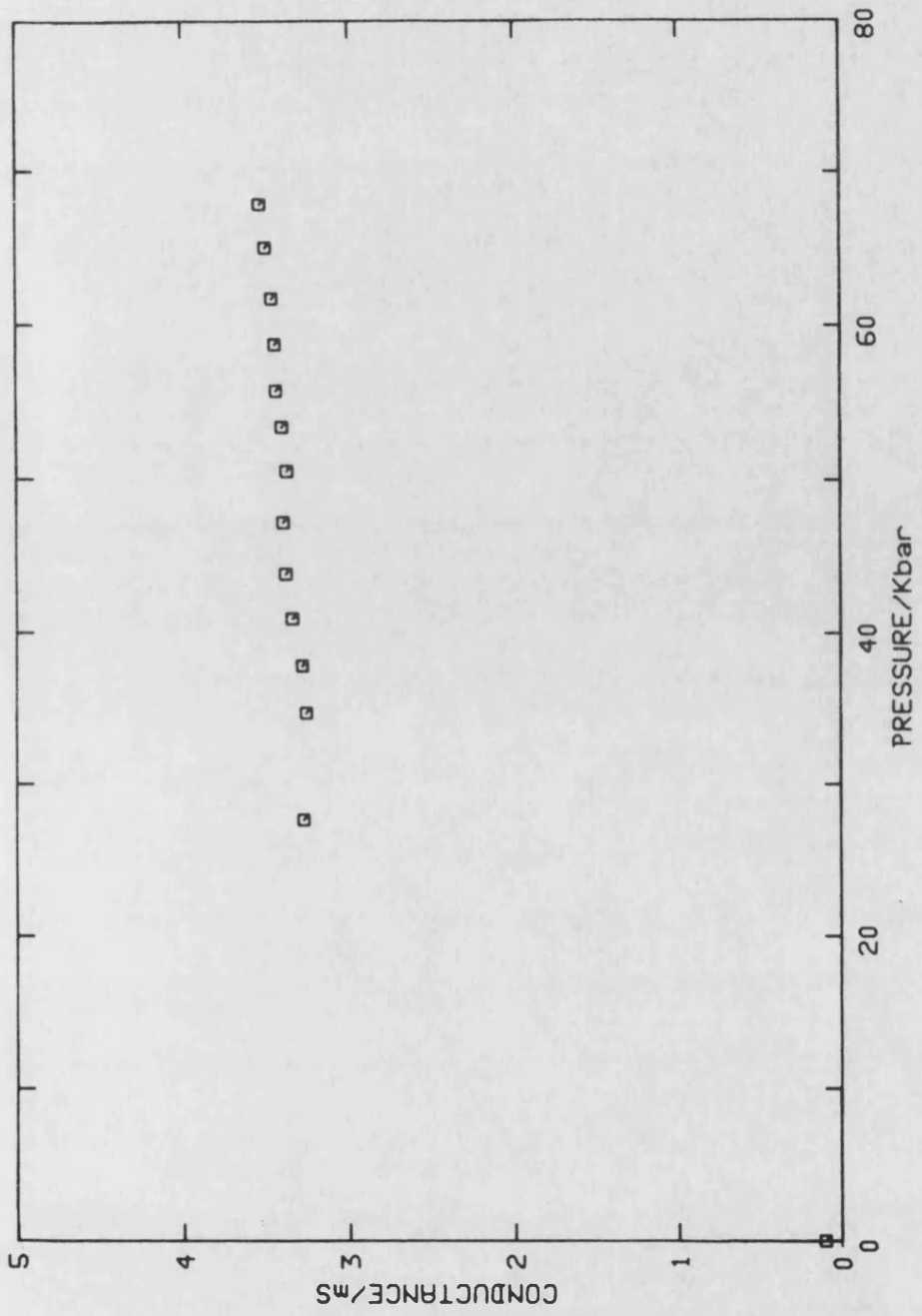

FIGURE 5.13

THE DC CONDUCTANCE, OBTAINED FROM THE REAL ADMITTANCE INTERCEPT, AS A FUNCTION OF HYDROSTATIC PRESSURE AT AN AMBIENT TEMPERATURE OF 300K.

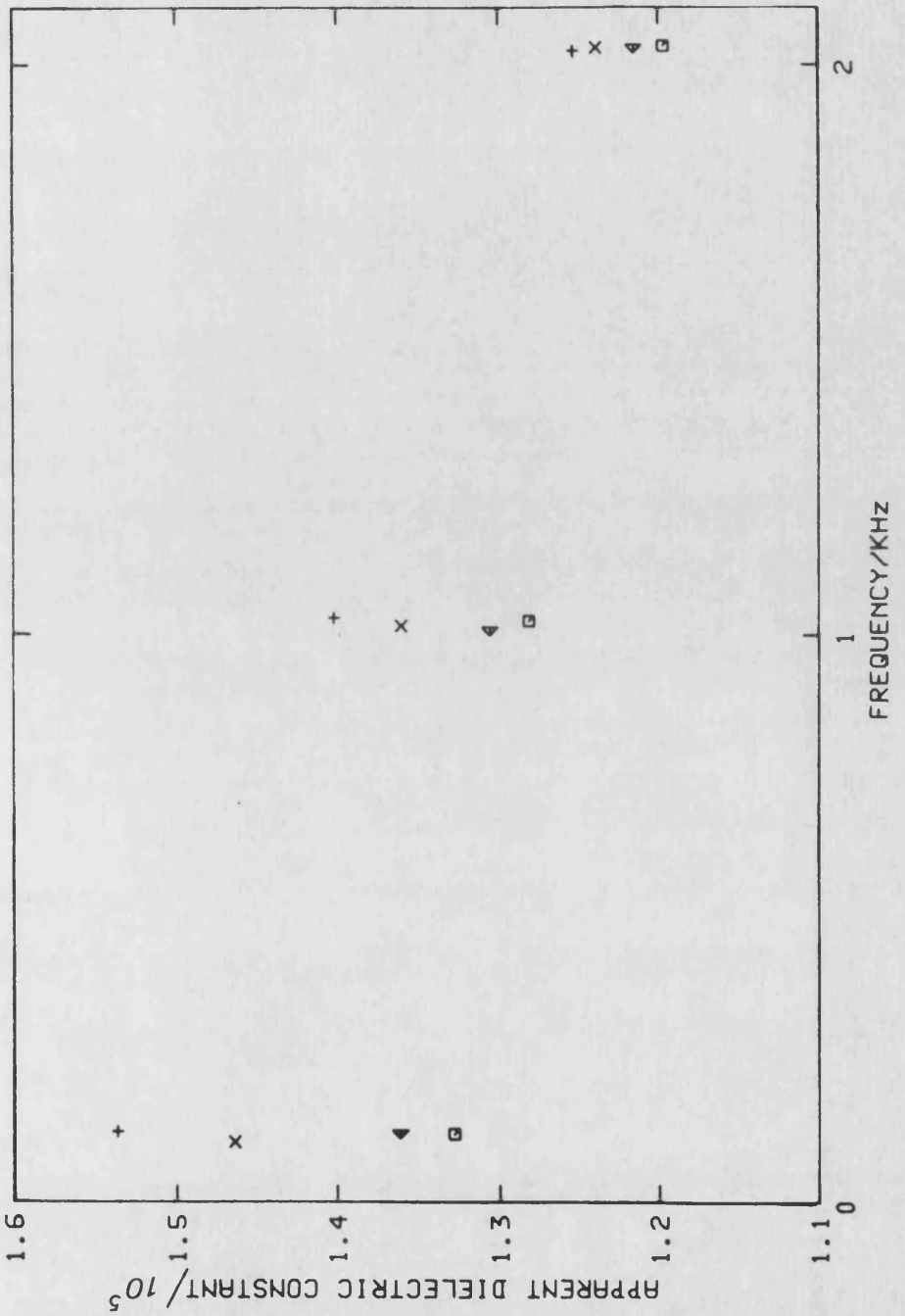

FIGURE 5.14

THE DIELECTRIC CONSTANT, CALCULATED FROM THE MEASURED CAPACITANCE ON THE BASIS OF THE SAMPLE DIMENSIONS, AS A FUNCTION OF FREQUENCY AT SELECTED PRESSURES (+ 25Kbar, × 37.5Kbar, ◁ 57.5Kbar AND □ 70Kbar).

exhibited by the simultaneously measured conductances (section 5.4). The dielectric constant values obtained were large and very dependent upon frequency - consistent with the other low frequency measurements on UO_2 (section 5.21), caused by the measurement of the boundary layer capacitance. Previous work (section 5.22(a)) on the boundary layer established its thickness as about 600Å, which was the correct thickness to use when evaluating the static dielectric constant for these samples. The variation of ϵ_o with pressure is shown in figure 5.15. The zero pressure dielectric constant was 21.5, this was lower than that found for the boundary layer (33) though the samples used were recently reduced (the experiments were conducted within two weeks of reduction).

A theoretical calculation (Harding private communication), using the Harwell PLUTO program, also showed a pressure dependence associated with the dielectric constant (figure 5.15). The zero pressure values of the experimental and theoretical data differed somewhat, this was attributed in part to the previously accepted value of ϵ_o used to parameterise the interatomic potential (section 2.5) and in part to the errors inherent when making capacitance measurements on samples with a small area to thickness ratio. Thus it was more instructive to note the reasonable agreement between the gradients: $-0.03 Kbar^{-1}$ (experimental) and

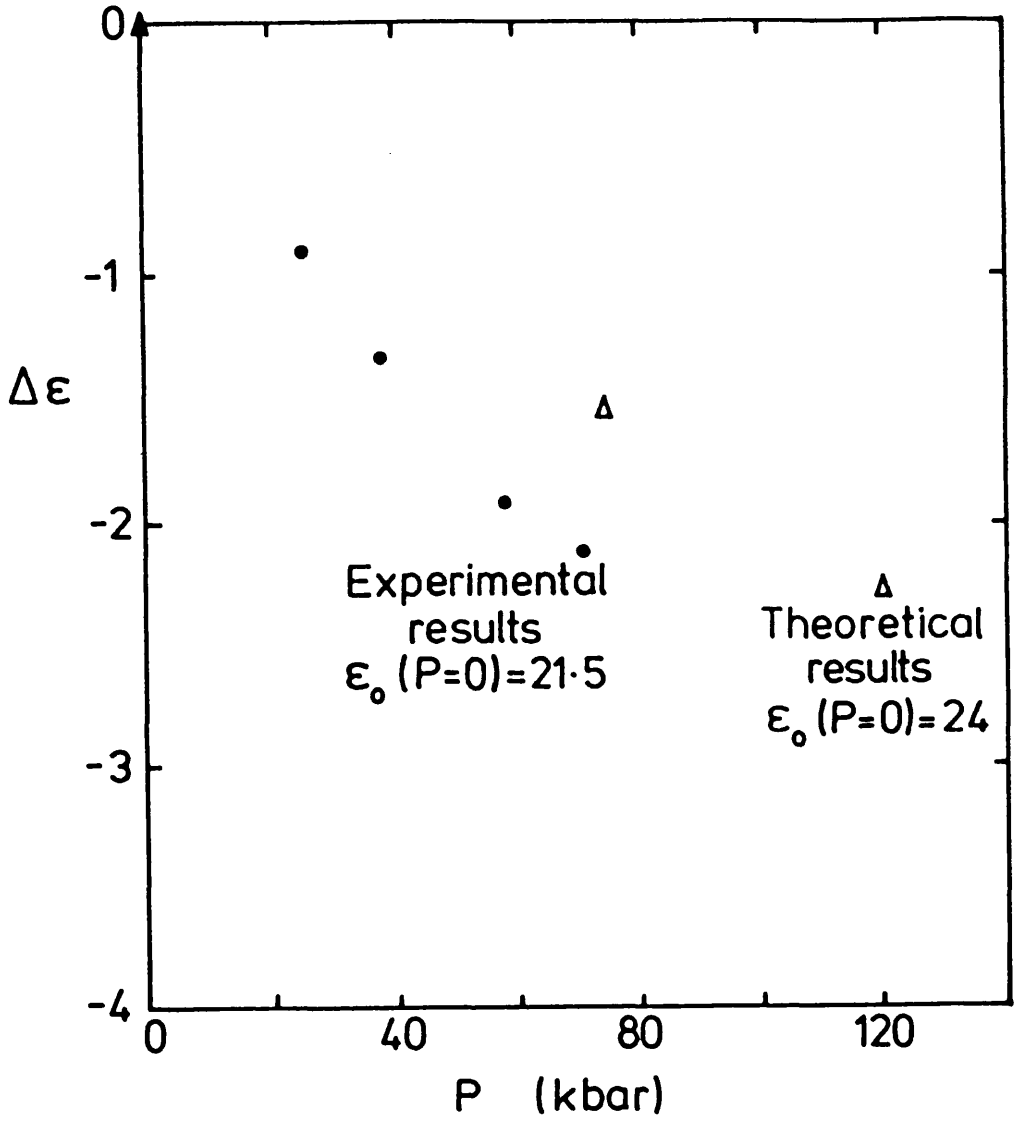

FIGURE 5.15

THE DIELECTRIC CONSTANT DEVIATION ($\Delta\epsilon=\epsilon(P=0)-\epsilon(P)$) AS A FUNCTION OF THE APPLIED HYDROSTATIC PRESSURE (• EXPERIMENTAL RESULTS AND ◅ THEORETICAL RESULTS). THE DIELECTRIC CONSTANTS WERE CALCULATED FROM THE DATA (FIGURE 5.14) USING 600Å AS THE THICKNESS OF THE BOUNDARY LAYER.

$-0.02 Kbar^{-1}$ (theoretical). It needs to be stressed here that these measurements correspond to the effect of hydrostatic presures on the boundary layer capacitance for nominally stoichiometric (recently reduced) material.

Section 5.43 CARRIER BINDING ENERGIES

The conductance will depend upon the conductivity and various geometrical factors. Its pressure dependence will come from the effects of pressure on the carrier concentration and carrier mobility. If we suppose that the carriers are electronic holes (U^{5+}) which are either free or bound to an oxygen interstitial, we can expect a carrier concentration (n) proportional to exp(-B/kT), with B the binding energy. If we suppose further that the holes are electronic small polarons, their mobility will have the form,

$$\mu = J^2 \exp(-D/kT) \qquad 5.5$$

where D is a hopping energy and J an electron transfer matrix element. We see that the pressure dependence has two main terms. First, there is the effect of changes in ϵ_o on B and D. Secondly there is the effect in the interionic spacing on J. We shall analyse each of these in turn.

In the simplest models, B corresponds to binding by a coulombic potential screened by the static dielectric constant ϵ_o, so we have $B=b/\epsilon_o$ (where $b=e^2/a$ with a the U^{5+} to oxygen interstitial spacing). Similarly the

polaron hopping energy depends upon the ionic polarization (rather than the total polarization) so one expects $D=d(1/\epsilon_\infty - 1/\epsilon_o)$. We shall ignore the dependence of the high frequency dielectric constant on pressure, since calculations suggest that it is small (Harding private communication). Thus the temperature dependent factors in the conductance contribute:

$$\xi = \exp(-d/\epsilon_o\ kT)\exp((d-b)/\epsilon_o kT) \qquad 5.6$$

with an overall activation energy of B+D. The pressure dependence at constant temperature gives

$$(1/\xi)(d\xi/dP)=(1/\epsilon_o^2 kT)(d-b)(-d\epsilon_o/dP) \qquad 5.7$$

Similarly we can write J with its standard exponential dependence on distance as a factor

$$\phi = J_o^2 \exp(-2R/q) \qquad 5.8$$

$$(1/\phi)(d\phi/dP)=2R/q(-1/R)(dR/dP) \qquad 5.9$$

Since the conductance is proportional to $\xi\phi$ we have

$$(1/G)(dG/dP)=$$

$$(d-b)/(\epsilon_o kT)(-1/\epsilon_o)(d\epsilon_o/dP)+2R/q(-1/R)(dR/dP) \qquad 5.10$$

Since we do not know (d-b) nor q, we cannot find a unique solution

The analysis now proceded in three directions. One option was to neglect the last term in equation 5.10; this analysis gives B and D as a combination and not as separate values. However the Arrhenius energy (E_a=B+D=0.17eV) was known from the conductivity data and this was used to obtain the separate energies. This approach leads to the values of 0.0145eV and 0.1555eV

for B and D respectively. Another approach considers only the last term and allows a value for 2R/q to be calculated - 17.105. This value for 2R/q gave the dimension for which d=b. A third approach was to postulate possible values for 2R/q and then to calculate values of B and D (table 5.3 and figure 5.16). The analysis indicated that B and D were adequately fitted by the equations:

$$B=0.0145+(2R/q)*1.601*10^{-3} \qquad 5.11$$

$$D=0.1553-(2R/q)*1.604*10^{-3} \qquad 5.12$$

Thus the analysis was able to give the range of 2R/q for which B, D and 2R/q were positive; the range of the binding and hopping energies that were encompased within the allowed values of 2R/q were also calculated:

$$0.0145eV < B < 0.17eV$$

$$0.155eV > D > 0eV$$

where B+D=0.17eV, within the range

$$0 < 2R/q < 96.84$$

Within the allowed range for the binding (B) and hopping (D) energies, at 2R/q=44, the two energies were equal (0.085eV).

Theoretically, the Harwell HADES code has been used to estimate the energy needed to ionise an oxygen interstitial cluster

TABLE 5.3 BINDING AND HOPPING ENERGIES AT SELECTED VALUES OF 2R/q, CALCULATED FROM EQUATION 5.10 WITH AN ARRHENIUS ENERGY OF 0.17eV.

2R/q	q/Å (R=2.7341Å)	BINDING ENERGY/eV	HOPPING ENERGY/eV
10	0.55	0.031	0.139
20	0.27	0.047	0.123
30	0.18	0.063	0.107
40	0.14	0.078	0.091
50	0.11	0.094	0.075
60	0.09	0.111	0.059
70	0.08	0.127	0.043
80	0.07	0.143	0.027
90	0.06	0.158	0.011
100	0.05	0.175	-0.005

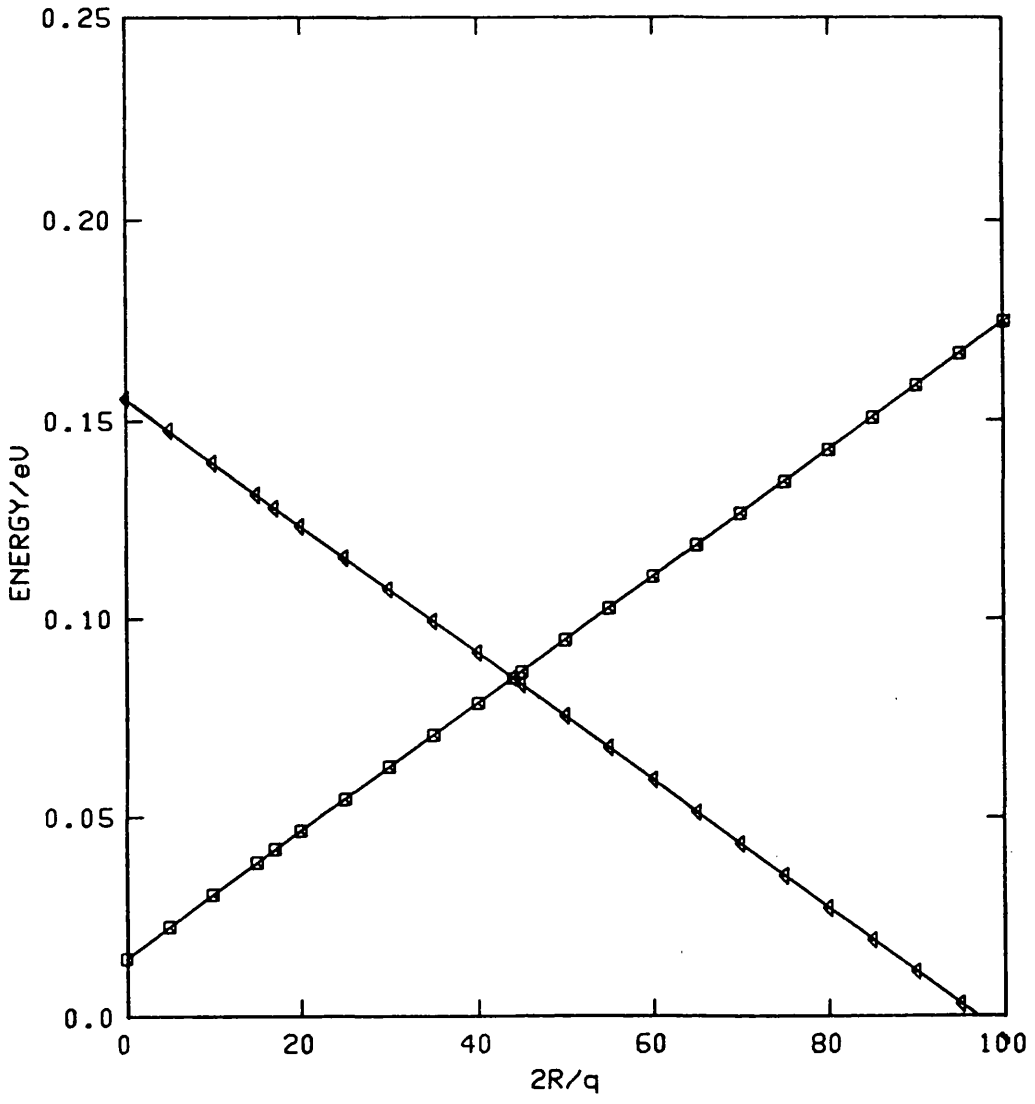

FIGURE 5.16

THE BINDING (◁) AND HOPPING (□) ENERGIES, CALCULATED FROM EQUATION 5.10, AT SELECTED VALUES OF 2R/q.

O^{2-}_{int} + 2 adj U^{5+}_{holes} > O^{2-}_{int} + 2 dist U^{5+}_{holes} 5.13

This energy has been calculated as being about 0.86eV. We can assume that the second hole will be twice as strongly bound as the first, so that the cost of successively ionising each hole is 0.29eV and 0.57eV respectively. Thus the calculated binding energy for the first hole (0.29eV) does not seem to agree with the observed value (0.17eV at most!).

The author is indebted to Dr AM Stoneham for the assistance rendered with this section.

Section 5.44 ELECTRICAL PROPERTIES AT HIGH PRESSURES AND HIGH TEMPERATURES

The temperature dependence of the high pressure admittance profiles was assessed by using a resistance heater incorporated in the sample assembly (section 4.43(e)). Experiments using nichrome windings were attempted but sample assembly failure occured before data was extracted. The tetrahedral anvil sample holder was loaded to a sample pressure of 50Kbar and the sample temperature was increased until sample assembly failure, due to the degradation of the carbon resistance heater (section 4.43(e)). The sample temperature was assessed from the power calibration curve (figure 4.15) because the incorporated thermocouple fractured during each experiment. The conductance of the sample was

calculated from the intercept on the Y' axis in a similar manner to that used at ambient temperatures (figure 3.14): the admittance profiles of the boundary layer of the large disc samples did not show any inclination. The dielectric properties were assessed from the exponent n, calculated from the gradient ($n\pi/2$) of the admittance profiles using the "universal" response of the capacitor to incorporate the frequency dependence of the components of the equivalent circuit. The dielectric constant could then be calculated on the basis of this analysis (section 3.7). The observed "universal" response was expressed in terms of the real and imaginary parts of the complex permittivity.

$$\epsilon'(\omega) = \epsilon_{\infty} + a_n \omega^{n-1} \qquad 5.14$$

$$\epsilon''(\omega) = a_n \cot(n\pi/2)\omega^{n-1} \qquad 5.15$$

The exponent n was also calculable from the frequency dependence of the imaginary dielectric constant $(Y'-G)/\omega C_o$, where C_o was the geometrical capacitance (Jonscher and Reau 1978). However this procedure required that G be known to a higher precision than was available with this data. Thus the only reliable source of information on n was the admittance profile. The constant of proportionality a_n was estimated by analogy with the capacitance measurements detailed in section 5.42. The temperature dependences of the conductance and the exponent n at 50Kbar are given in figures 5.17(a) & (b),

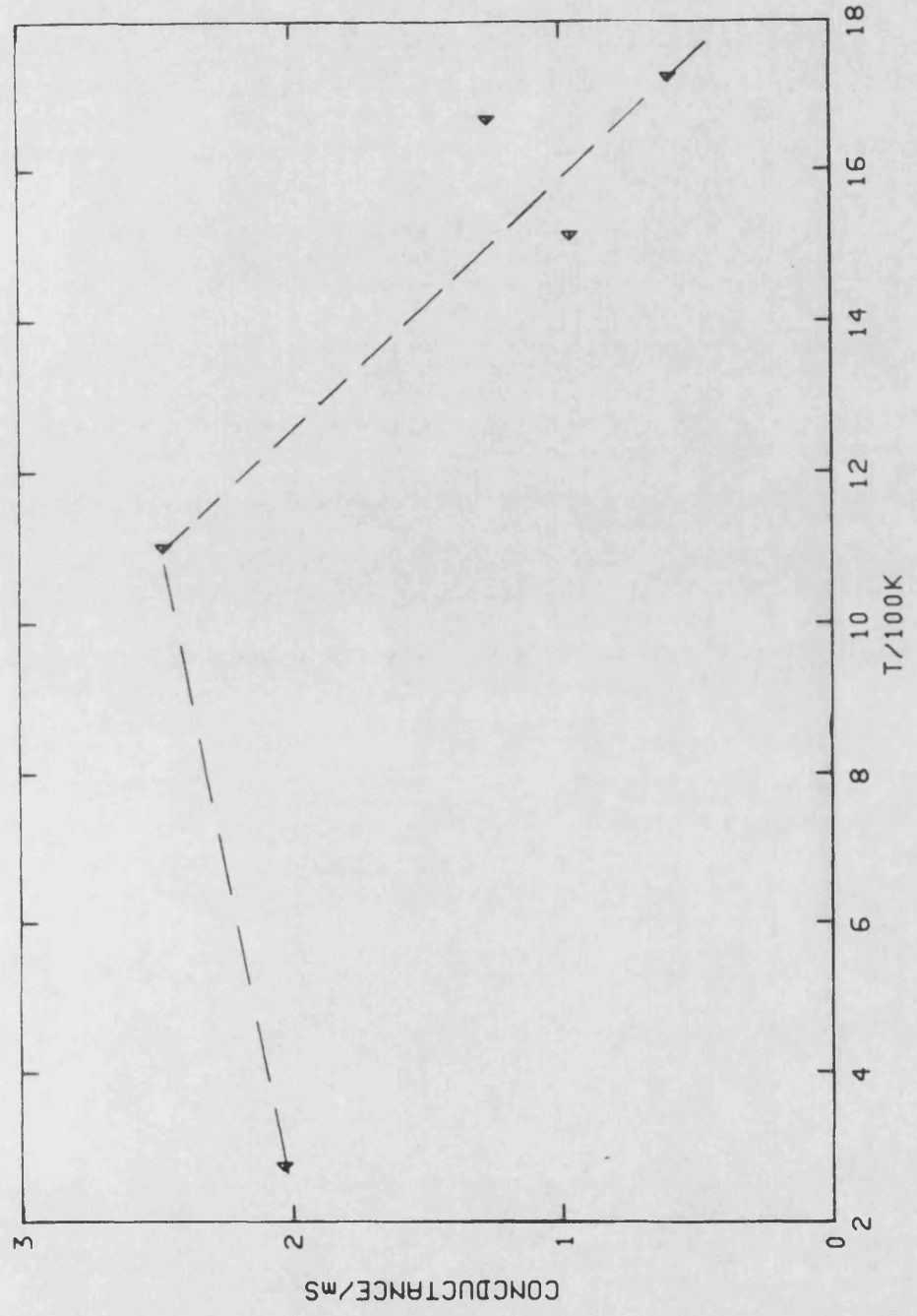

FIGURE 5.17(a)

THE CONDUCTANCE AS A FUNCTION OF TEMPERATURE AT A CONSTANT HYDROSTATIC PRESSURE OF 50Kbar FOR SINGLE CRYSTAL (NORTON) MATERIAL.

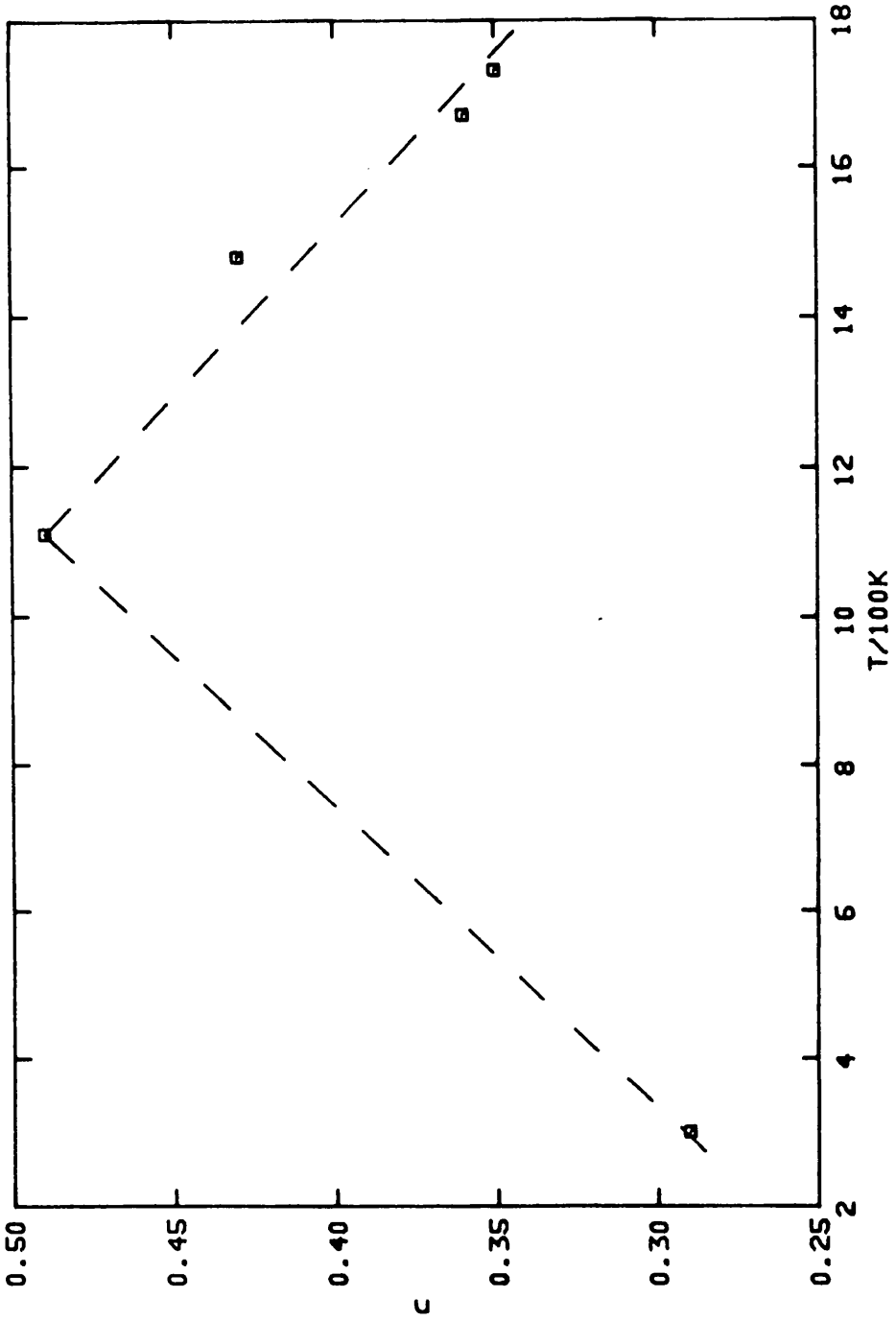

FIGURE 5.17(b)

THE EXPONENT n, REPRESENTING THE FREQUENCY DEPENDENT DIELECTRIC PROPERTIES, AS A FUNCTION OF THE TEMPERATURE AT A CONSTANT HYDROSTATIC PRESSURE OF 50Kbar FOR SINGLE CRYSTAL (NORTON) MATERIAL.

respectively.

The conductance as a function of temperature steadily increased up to a about 1100K; for temperatures in excess of this value the conductance steadily decreased. A similar change in character was exhibited by n (hence the dielectric constant) as a function of temperature. The change in the shape of the conductance and dielectric response of the boundary layer occured at the same temperature. This temperature was not greatly different to the temperature at which a transition from extrinsic to intrinsic conduction was observed for bar shapped Norton material (to be discussed in section 5.5). However in this case it would have been expected that the high pressure conductance would have increased rather than have decreased, as was observed. One possible explanation was that some other factor, the dimensions of the system say, altered which caused a conductance decrease.

Section 5.5 ELECTRICAL PROPERTIES AT HIGH TEMPERATURES

The admittance of bar shaped (3mm*3mm*10mm) samples as a function of temperature (figure 5.18) up to 1500°C was examined using the procedure detailed in section 4.5. The data indicated that the admittance profiles were not fully traversed. The thermal activation of the circuit components did not alter the characteristic frequencies sufficiently to fully identify the profile.

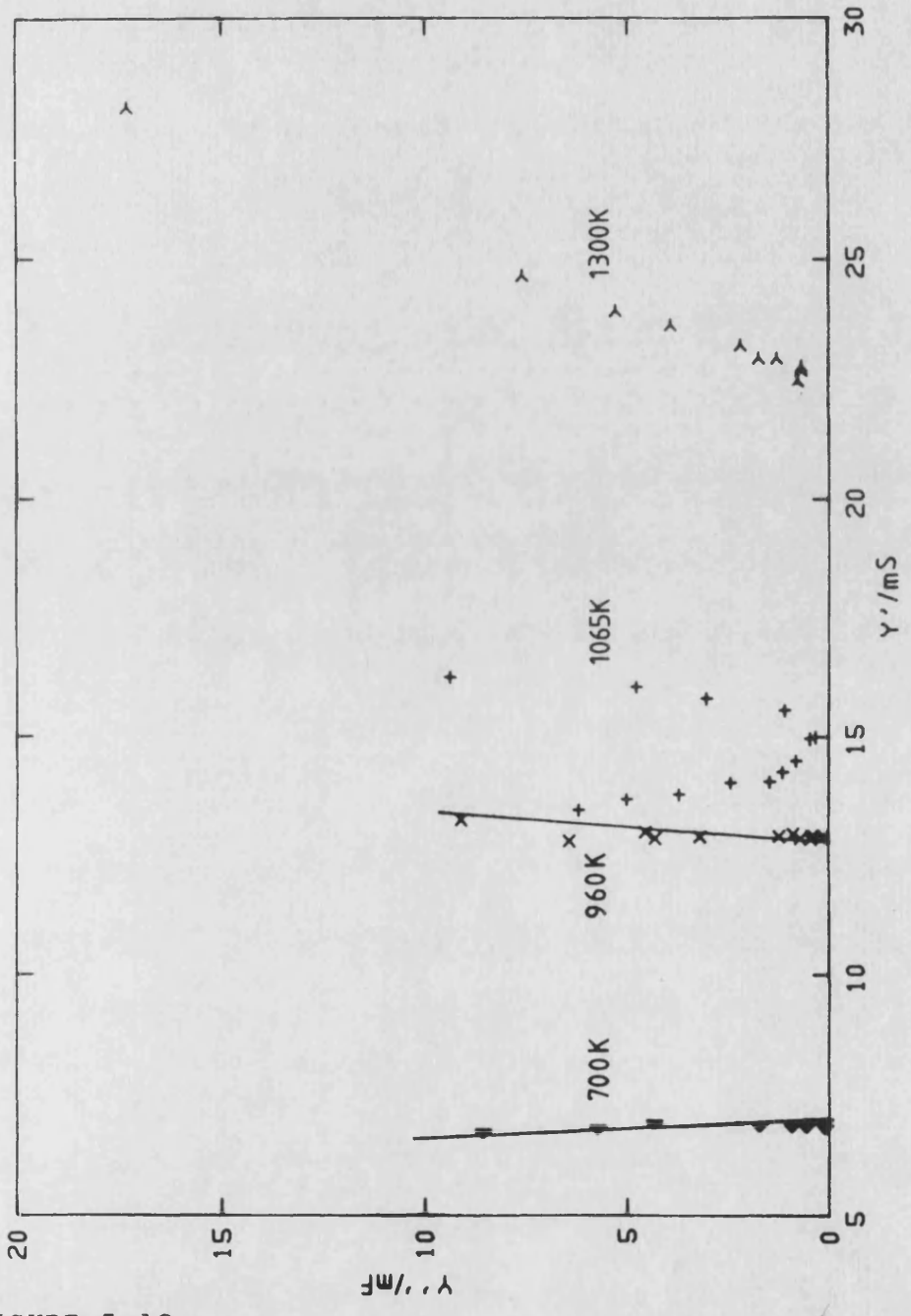

FIGURE 5.18

THE ADMITTANCE PROFILES OF SINGLE CRYSTAL (NORTON) MATERIAL AT SELECTED MEASUREMENT TEMPERATURES (◁ 700K, × 960K, + 1065K AND ≻ 1300K). THE SOLID LINES SERVE TO ILLUSTRATE THE GRADIENT OF THE PROFILES.

However the small portions of the profile that were available allowed for some of its features to be deduced. At low temperatures (700K) the profiles exhibited negative gradients with an intercept on the Y' axis. The Y' intercept was still identifiable at high temperatures (1300K), though the profile gradient was now positive. For intermediate temperatures (1065K) the profile exhibited a "V" shape, with a negative gradient at low frequencies and a positive gradient at high frequencies. The most plausible profile that fitted the observed data was that of a semicircular arc with an added high frequency spur (figure 3.6(b)); this was most clearly displayed at 1300K (figure 5.18). Such an admittance profile could be produced by two different equivalent circuits: figure 3.6 b), figure 3.6 c). To establish the correct equivalent circuit the complex capacitance $C^*=Y^*/j\omega$ was analysed (figure 5.19). Unfortunately only a very small portion of the profile was revealed, though this was useful in establishing the most likely circuit. Each circuit produced a semicircular capacitance profile, yet the ratio of the C' intercepts were widely different (Jonscher 1983). The low frequency C' intercept was approximately 1.1μF and was assessed as independent of the measurement temperature, whereas the high frequency intercept was over 2000 times larger than the low frequency intercept and highly temperature dependent. The results of the

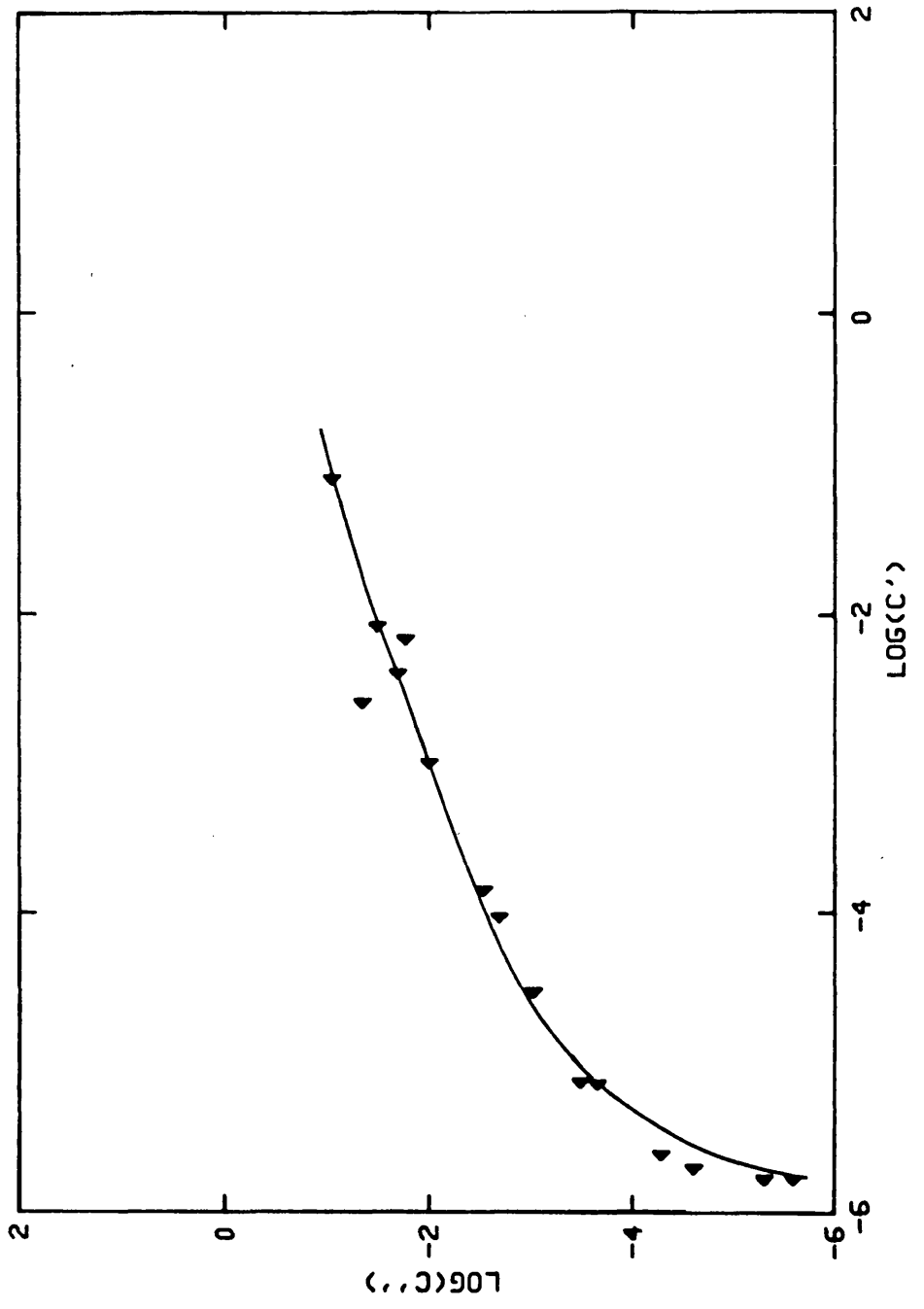

FIGURE 5.19 A)
THE LOGARITHMIC REPRESENTATION OF THE COMPLEX CAPACITANCE PROFILE FOR SINGLE CRYSTAL (NORTON) MATERIAL AT 1065K. THE PROFILE CLEARLY ILLUSTRATES THE LOW FREQUENCY INTERCEPT WITH THE REAL AXIS (PARALLEL CAPACITANCE).

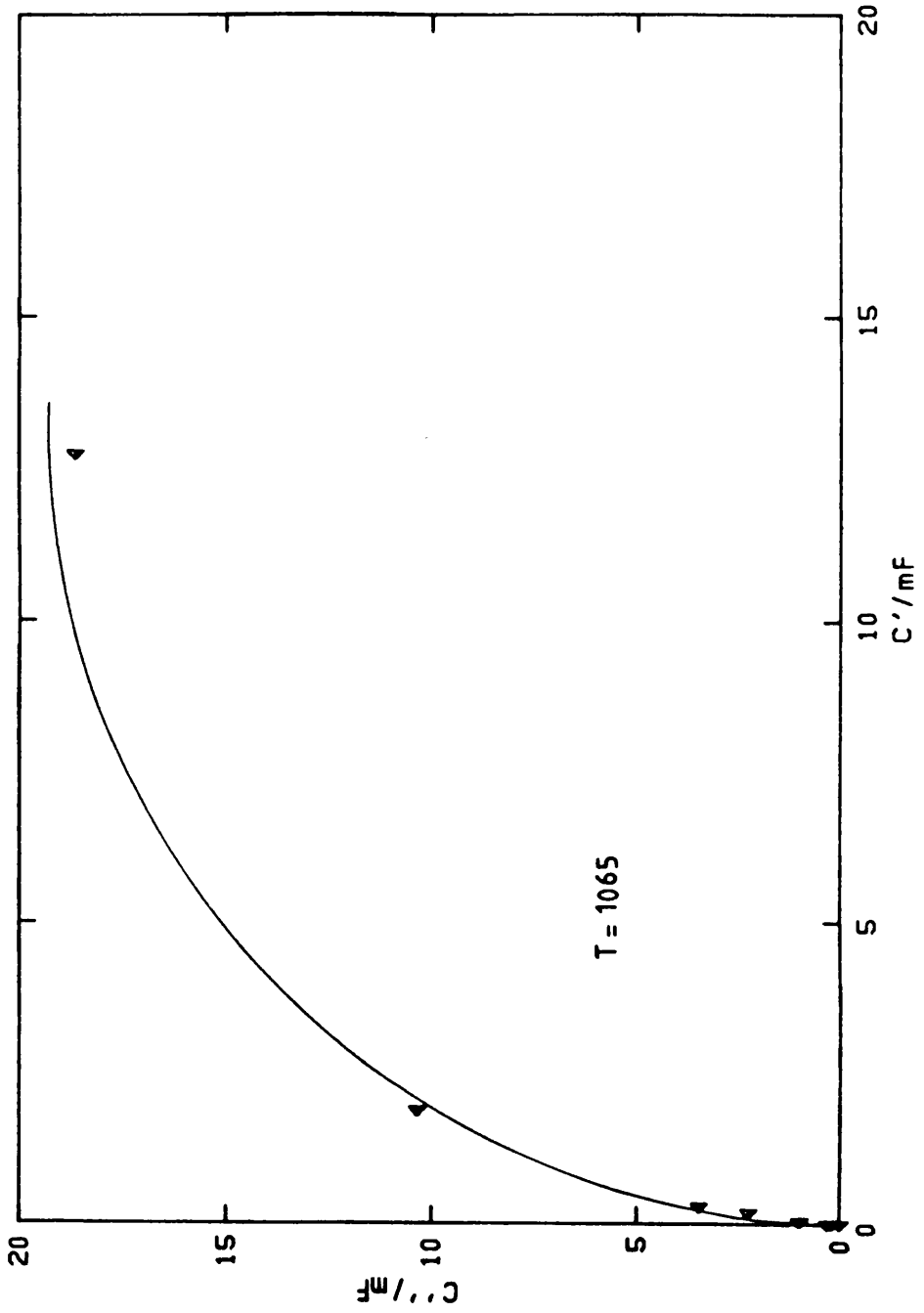

FIGURE 5.19 B)
A LINEAR REPRESENTATION OF THE COMPLEX CAPACITANCE PROFILE, AT 1065K, FOR SINGLE CRYSTAL (NORTON) MATERIAL. THE SEMICIRCULAR ARC ALLOWS FOR THE ESTIMATION OF THE HIGH FREQUENCY INTERCEPT WITH THE REAL AXIS (SERIES CAPACITANCE).

capacitance profile analysis and the voltage dependence of the semicircular arc of the admittance profile suggested that the most plausible equivalent circuit was that of figure 3.6 b): a parallel combination of capacitance and conductance in series with a capacitance. The high frequency capacitance intercept was tentatively assessed, for all temperatures, by fitting the low frequency portion of the capacitance profiles with a semicircular arc. To enable analysis the centres of the capacitance profiles were assumed to lie on the real capacitance axis. This simplistic approach neglected the slight inclination of the high frequency spur; such an inclination has previously been encompassed within a re-casting of the equivalent circuit (sections 3.6 and 5.43) ie replacing the parallel capacitance. The dielectric properties, for the low valued parallel capacitance, were assessed from the exponent n, where n was calculated from the gradient of the admittance profiles. This could only be done where the profiles exhibited positive gradients. Only values of n calculated from the admittance were used (for the reasons that were outlined in section 5.44). The value of A_n was estimated as $9.77*10^{-7}$. The temperature dependences of the high frequency capacitance, identified as the series capacitance in figure 3.6 b), and the exponent n (corresponding to the parallel capacitance) are given in figure 5.20. The

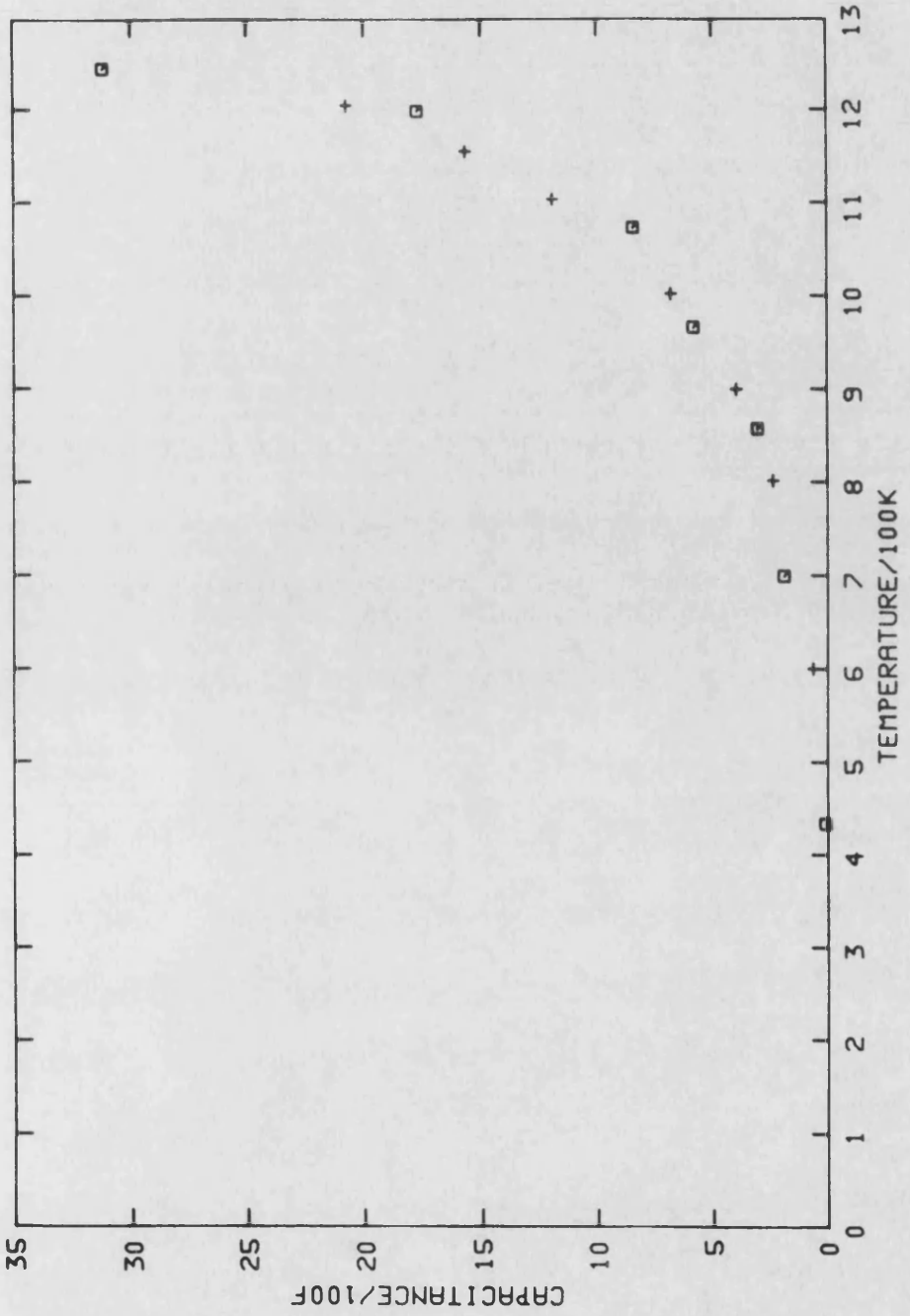

FIGURE 5.20 A)

THE SERIES CAPACITANCE OF A SINGLE CRYSTAL (NORTON) BAR AS A FUNCTION OF THE MEASUREMENT TEMPERATURE (□ EXPERIMENTAL DATA AND + DATA CALCULATED FROM EQUATION 5.13).

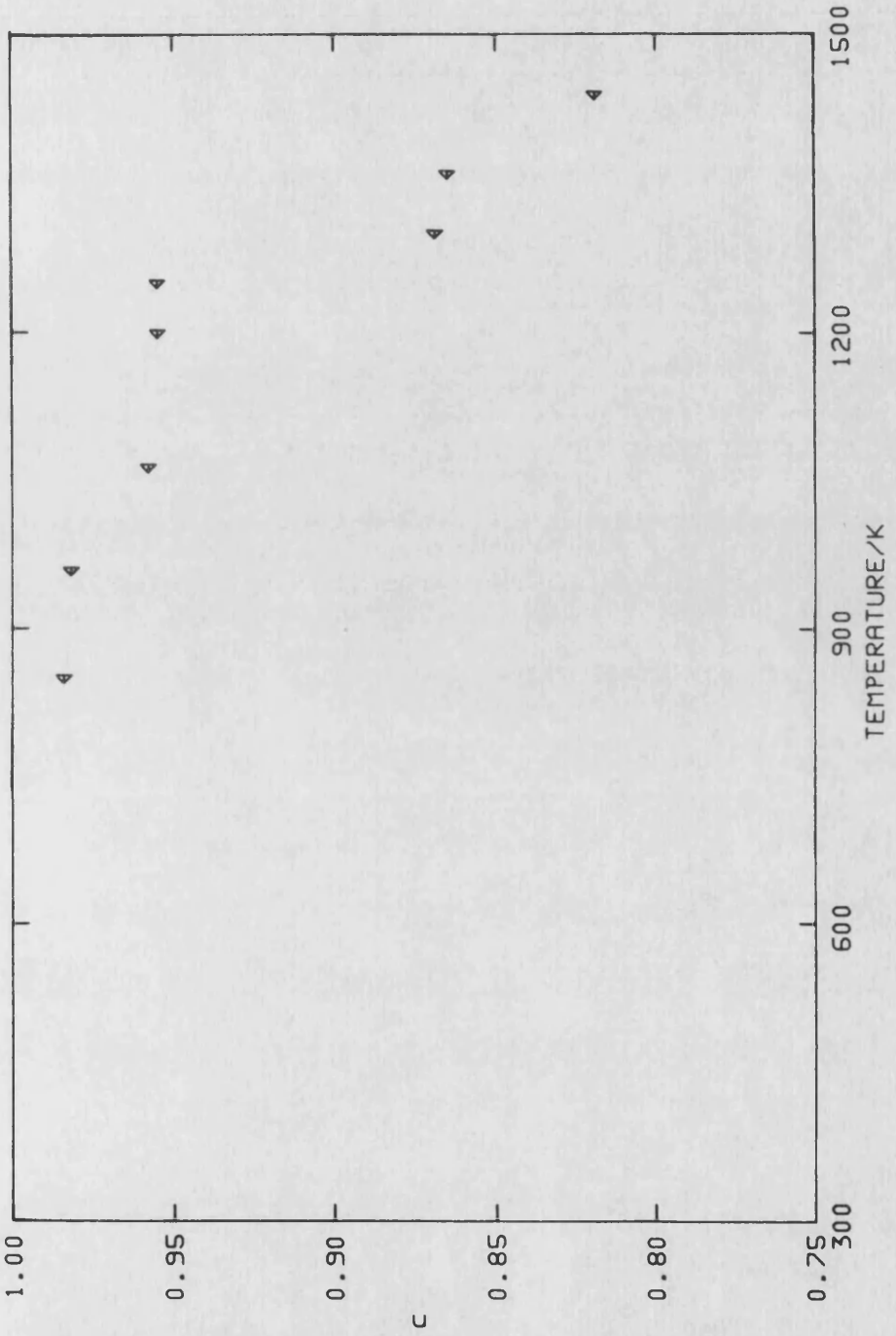

FIGURE 5.20 B)

THE TEMPERATURE DEPENDENCE OF THE EXPONENT n ASSOCIATED WITH THE PARALLEL CAPACITANCE OF A SINGLE CRYSTAL URANIUM DIOXIDE BAR.

temperature dependence of the series capacitance accounts for the change in the magnitude of the semicircular admittance arcs, from 700K to 1300K say, this temperature dependence could be adequately fitted by:

$$C=4.4*10^{-4}\exp(T/200) \qquad 5.16$$

The origins of the two capacitances were not established definitively. However the temperature dependences of the capacitances indicated that the parallel capacitance was possibly a stray one because it showed minimal voltage and temperature dependences, whereas the series capacitance displayed a large temperature dependence and was consequently ascribed to surface effects. This identification was considered to be reasonably consistent with the electrode system.

The conductance as a function of temperature (figure 5.21), in an Arrhenius format, showed two regions of good linearity above and below 1275K. The value of the conductance was assessed with a high degree of confidence as the identification of the Y' intercept was common to both of the possible equivalent circuits. The activation energies and conductance prefactors were calculated on the basis of both band conduction and small polaron models and are given in table 5.4. Conductivity values were not calculated for the conductance data due to the inaccuracies inherent in assessing the associated geometrical factor (Valdes

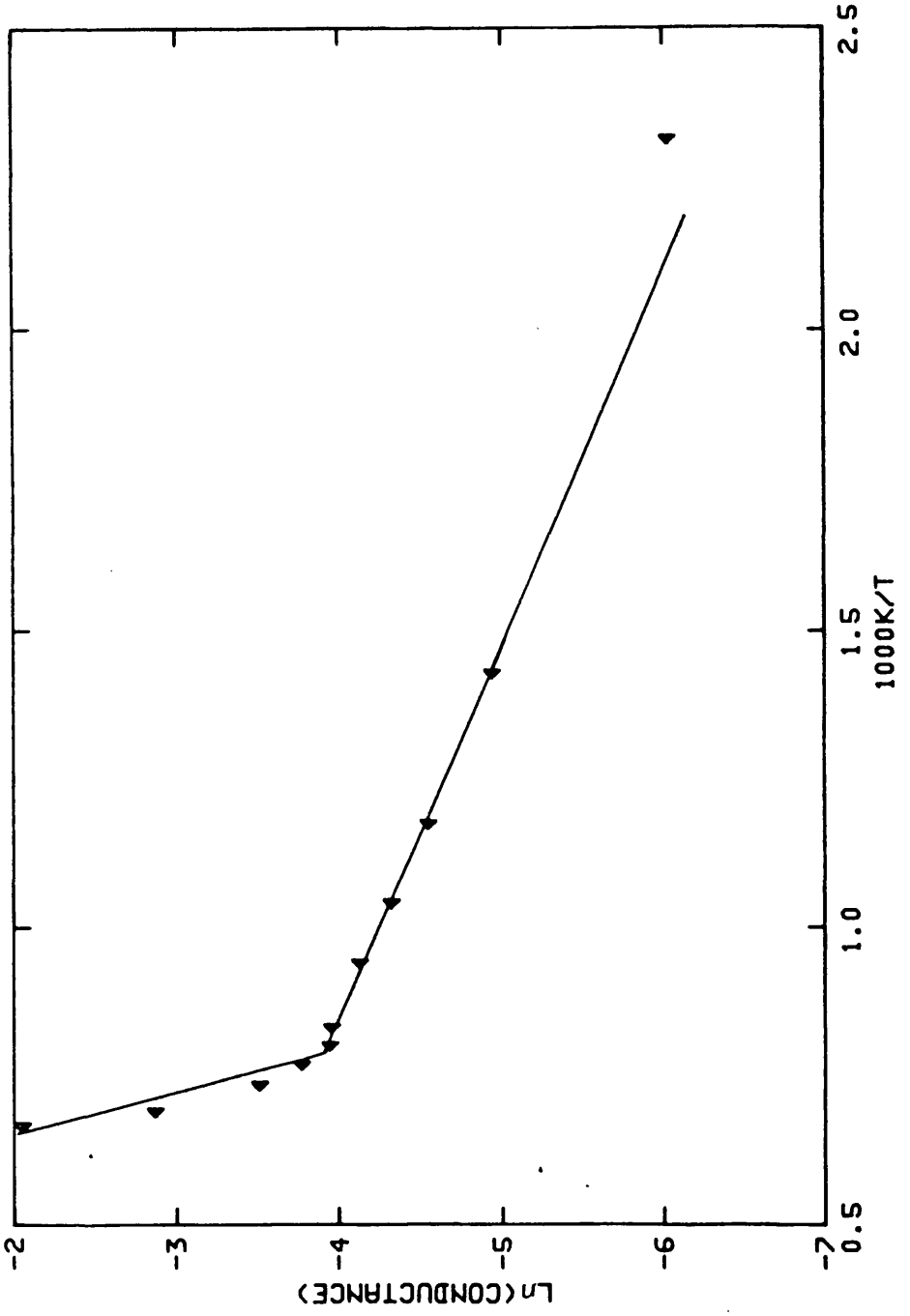

FIGURE 5.21

THE CONDUCTANCE, CALCULATED FROM ADMITTANCE PROFILES (FIGURE 5.18), AS A FUNCTION OF TEMPERATURE FOR SINGLE CRYSTAL (NORTON) MATERIAL. THE SOLID LINES SERVE AS A GUIDE TO THE EYE.

TABLE 5.4 ACTIVATION PARAMETERS FOR SINGLE CRYSTAL URANIA CALCULATED FROM ADMITTANCE PROFILE DATA FROM HIGH TEMPERATURE EXPERIMENTS, ON THE BASIS OF BOTH BAND CONDUCTION AND SMALL POLARON MODELS.

MODEL		PRE-FACTOR	ACTIVATION ENERGY/eV
#BAND	*	0.06	0.12±0.004
CONDUCTION	+	5079	1.404±0.23
$SMALL	*	1134	0.186±0.008
POLARON	+	$19*10^6$	1.52±0.208

* LOW TEMPERATURE REGION

\+ HIGH TEMPERATURE REGION

\# PREFACTOR DIMENSIONS Ω^{-1}

$ PREFACTOR DIMENSIONS $\Omega^{-1}K$

1953). The change in the activation energy at 1273K can be identified as being due to a change in the conductivity mechanism (section 2.27). The activation energies and the transition temperature were consistent with other work (table 2.1). Hyland and Ralph (1983) were able to calculate the energy of the Mott-Hubbard gap (the energy neccessary for the disruption of the Mott insulating state) from conductivity data above and below the intrinsic-extrinsic phase transition (Killeen 1980); the value so calculated was 1.86eV. Using the same approach the value of the Mott-Hubbard gap was calculated, using the activation energies obtained from the present work, for both small polaron and band conduction models: 2.67eV (small polaron), 2.57eV (band conduction). Both of these values were significantly larger than that calculated from Killeens work. However the only difference between the two conductivity studies was the use of ac techniques rather than dc methods (both investigations were carried out in the same furnace at CEGB, Berkeley with essentially the same electrode system).

The transition temperatures of the conductance data of figures 5.17(a) and 5.21 correlated well. This suggested that the high pressure (50Kbar) conductance decrease observed at about 1100K (figure 5.17(a)) and the decrease at about this temperature in the capacitive exponent (figure 5.17(b)) were related to the change in

the conduction mechanism.

The equivalent circuit and the values obtained from this analysis were used to calculate normalised impedance frequency profiles, which were complimentary to those produced by Bates (1967) (figure 2.8). The calculated profiles (figure 5.22) indicated that, given a sufficiently large frequency range, a "dual plateau" shape with a steep low frequency enhancement was exhibited. These profiles were displaced as the measurement temperature was altered. The displacement was caused by the thermal activation of the characteristic frequency of the parallel portion of the circuit ($1/C_pR$), through the resistance and parallel capacitance values (the parallel capacitance values were only slightly temperature dependent). It was convenient for the data (figure 5.22), which were clearly of the same shape at each temperature, to be normalised to provide a "master curve". This was achieved using a procedure developed to handle dielectric loss data (Jonscher 1983). Essentially one of the curves was traced, and this tracing was then displaced laterally to coincide with another curve, which was also subsequently traced. This procedure was repeated at each temperature to produce the master curve (figure 5.23). The high frequency portions of the curves were overlapped to produce the master curve as this portion was of most interest; the technique worked equally well for the low

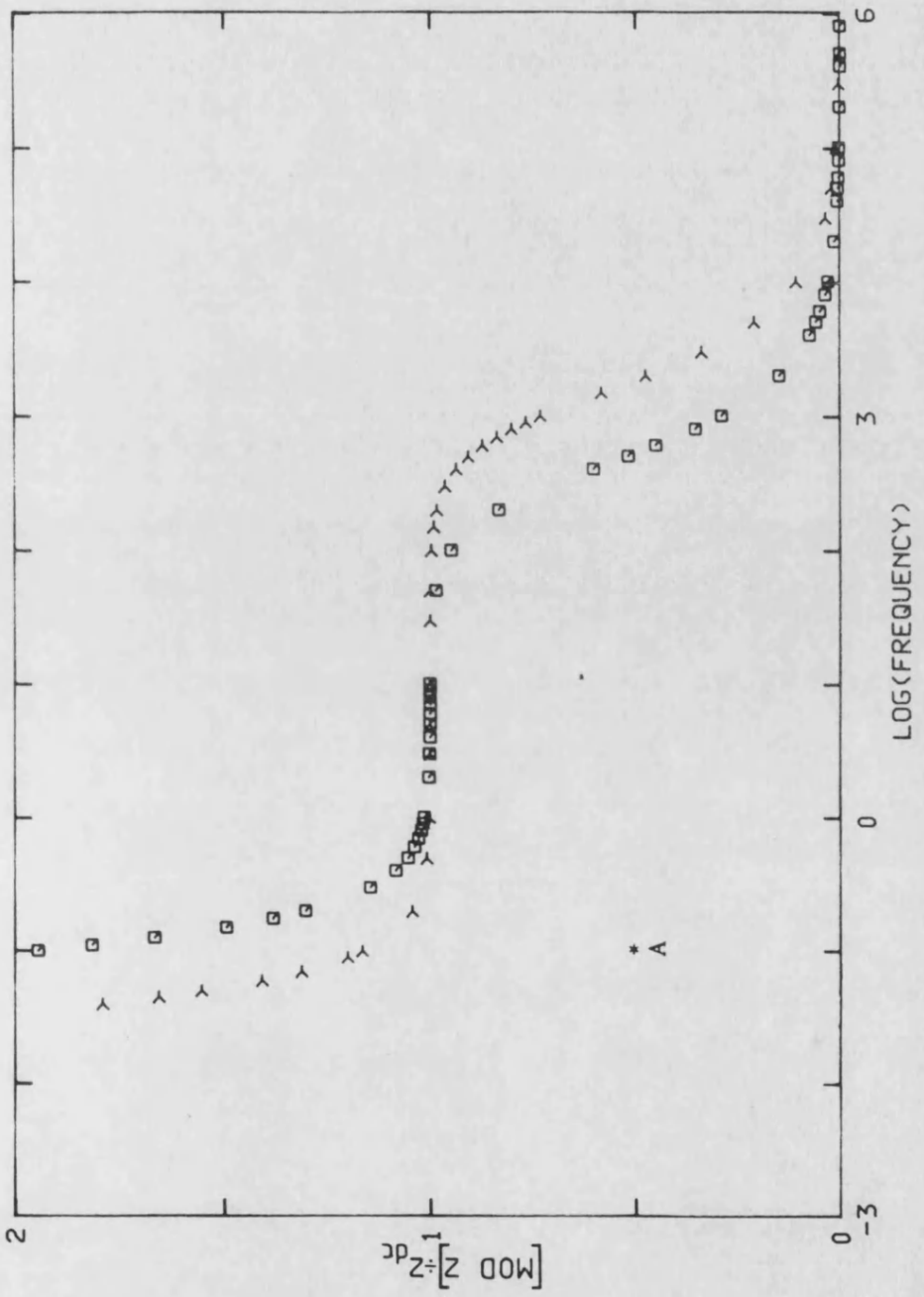

FIGURE 5.22
THE RATIO OF THE MODULUS OF THE IMPEDANCE TO THE DC IMPEDANCE AS A FUNCTION OF THE MEASUREMENT FREQUENCY CALCULATED ON THE BASIS OF THE PROPOSED EQUIVALENT CIRCUIT (SECTION 5.5) USING COMPONENT VALUES CALCULATED FROM THE ADMITTANCE ANALYSIS AT SELECTED TEMPERATURES (□ 430K; R=500Ω, C_s=0.002F: ⋎ 700K; R=140Ω, C_s=0.02F), C_s=1μF.

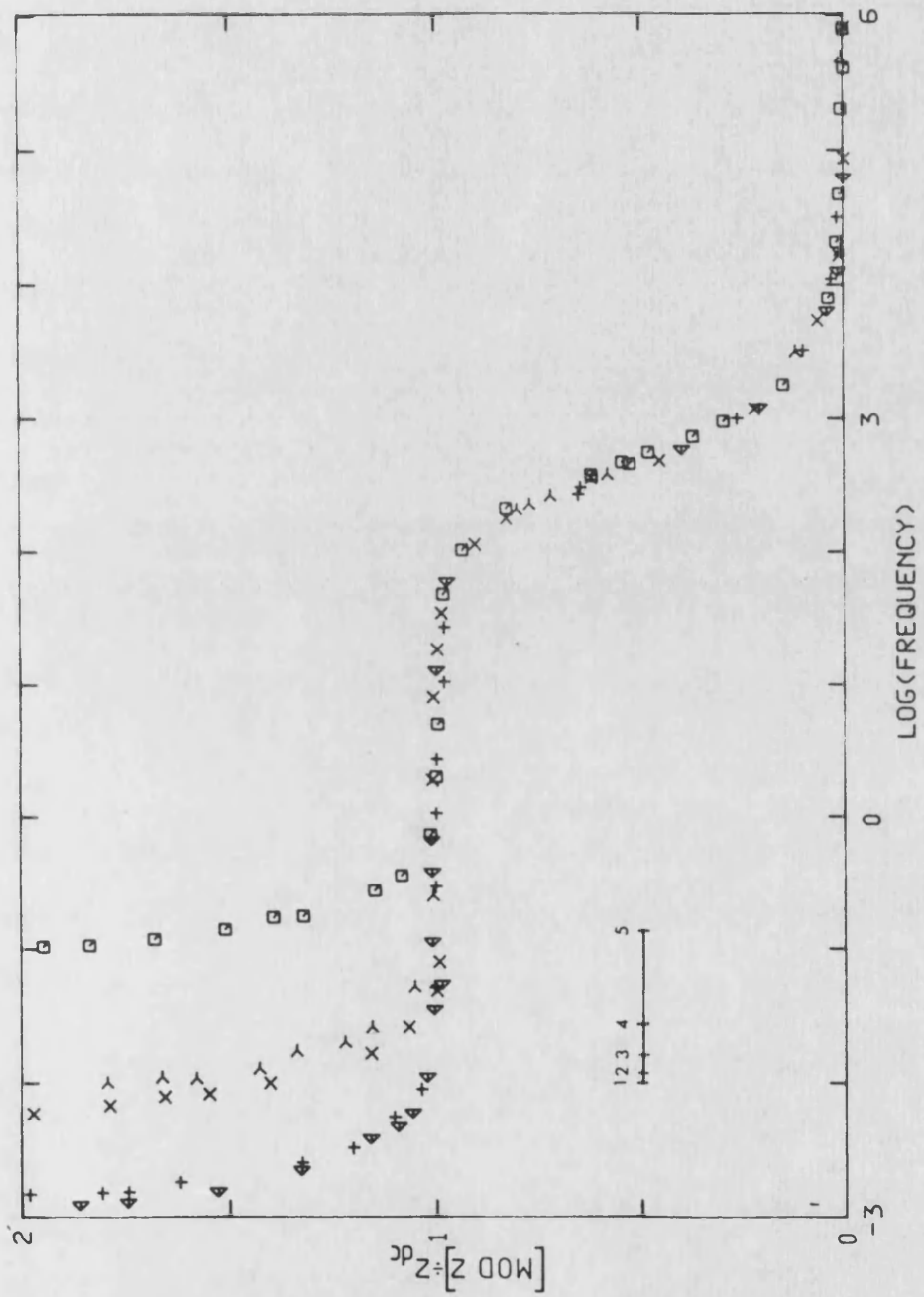

FIGURE 5.23
THE MASTER CURVE FOR THE DATA PRESENTED IN FIGURE 5.22 (◁ 1400K; R=16Ω, C_s=0.59F. ≻1200K; R=54Ω, C_s=0.18F.+ 850K; R=95Ω, C_s=0.03F. ×700K; R=140Ω, C_s=0.02F.□430K; R=500Ω, C_s=0.002F), C_s=1μF. THE SOLID LINE REPRESENTS THE LOCUS OF THE POINT A, IN FIGURE 5.22, AT SELECTED TEMPERATURES OR CHARACTERISTIC FREQUENCIES((1) 1440K, 9947Hz: (2) 1200K, 2953Hz: (3) 850K, 1677Hz: (4) 700K, 1134Hz: (5) 430K, 318Hz).

frequency spur, though a different locus curve would be produced. The locus (the solid line in figure 5.23) of an arbitrary reference point (A) was incorporated to retain all of the information necessary to reconstruct the initial data; it also allowed data for any intermediate temperature to be constructed. The locus curve was more usefully calibrated in terms of the characteristic frequency of the parallel combination ($1/C_pR$); it was the thermal activation of this quantity that caused the shift of the curves.

The shape of the master curve (figure 5.23) fitted the high temperature data of Bates (1967), which showed a plateau that merged with a downwardly curved region at higher frequencies. The frequency independence of the low temperature data was well represented by the plateau region of figure 5.23. The manner in which the data of Bates (1967) were offset with temperature could not be assessed accurately. An estimate of this offset was attempted (figure 5.24) using the resistance data of Bates et al (1967) and anticipating the likely capacitances for their measurement system. The parallel (stray) capacitance used was the same as that identified in this text whilst the series (surface) capacitance was calculated from the sample dimensions using the capacitance per unit area from this text. The calculated profiles showed the same two plateau shape as that previously obtained (figures 5.22 and 5.23), except

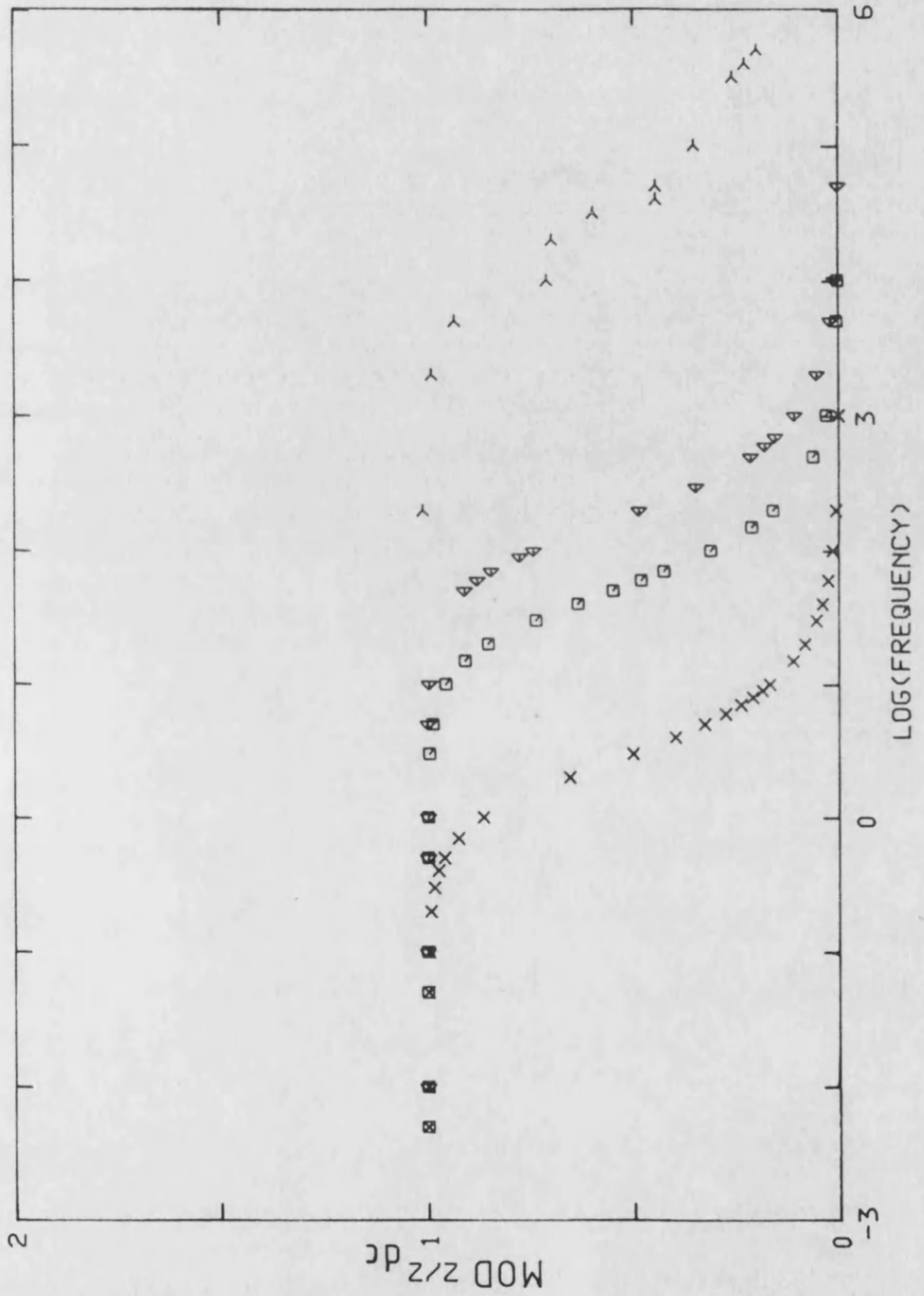

FIGURE 5.24
THE RATIO OF THE MODULUS OF THE IMPEDANCE TO THE DC IMPEDANCE AS A FUNCTION OF THE MEASUREMENT FREQUENCY CALCULATED ON THE BASIS OF THE PROPOSED EQUIVALENT CIRCUIT (SECTION 5.5) USING COMPONENT VALUES ESTIMATED FROM THE ADMITTANCE ANALYSIS AND THE ANALYSIS OF BATES (1967) AT SELECTED TEMPERATURES (◁ 1500K; R=1.36KΩ, C_s=2.35F. □ 1000K; R=4.6KΩ C_s=0.19F. × 500K; R=87KΩ, C_s=0.01F). ACTUAL DATA FROM FIGURE 2.7 (≻) AT 2628K HAS BEEN INCLUDED FOR COMPARISON.

that the larger values of the series capacitance meant that the low frequency enhancement was not developed until much lower frequencies. One added complication was the nature of the sample supports (6.2mm diameter tungsten discs at the sample ends) which were used as the current probes, in all of the work by Bates et al (1966,1967) and Bates (1967). The contact impedances should, in a four electrode system, not be measured; the contacts used were not of a type normally used for conductivity measurements: which are point contacts with a surface area very much smaller than the sample dimensions. The impedance of these contacts were significant in comparison with the sample resistance; this was indicated by the difference between the two probe and four probe measurements of Bates et al (1966). The crucial question is whether the contact impedances contributed to the equivalent circuit, and if so how? The possible effects of these on the equivalent circuit cannot be assessed. However as long as no resistive components attributable to these probes were measured then the impedances would have added, at most, an extra geometrical capacitance to the equivalent circuit, adding only to the curvature of the curves (figure 5.25). If they added a resistive component then the plateau region would be displaced vertically. Bates et al (1967) explained the curvature of their data (figure 2.8) through effects within the measurement system by

calibration using a test material (graphite); however if the current probes played a part in the curvature then their effect would not be expected to be the same for different materials. Not withstanding these possible problems this analysis has enabled the ac data of Bates (1967), more specifically its shape, to be interpreted as being due to different portions of the profile being traversed at different temperatures. More importantly, however, it has indicated that the low frequency frequency independent plateau from which Bates et al chose to extract their dc resistances could in fact be identified as the dc resistance. Additionally the identification of an alternative equivalent circuit, through the present ac work, does not require that the ac and dc work of Bates et al (1967) be reassessed.

This analysis was not helpful in interpreting the polycrystalline results of Bates et al as it failed to identify data rising to a plateau. This was not unexpected as the equivalent circuit for polycrystalline material would include, at least, another capacitance and resistance to take into account the effects of the grain boundaries.

CHAPTER 6 SUMMARY AND CONCLUSIONS

This thesis has detailed the construction and development of an impedance profiling system, together with the application of these techniques to a wide range of physical situations. An example of this usage is the high pressure sample assembly that has been designed to facilitate the investigation of the temperature dependence of the conductivity at elevated pressures. The objective has been to investigate some of the problems posed by the electrical properties of uranium dioxide.

The capacitance of uranium dioxide slices measured at high temperatures or low frequencies takes on anomalously high values. This problem has been resolved with the identification of a thin boundary layer with a thickness of 600Å. When this is included the correct geometrical factor for the conversion of the capacitance data to dielectric constants is obtained. The dielectric constant calculated in this manner from the boundary capacitance is 33. The anomalous dielectric constants arise if the high value of the measured boundary capacitance is associated with the sample thickness rather than, as it should be, with that of the

boundary layer. In fact the high boundary capacitance swamps the smaller bulk capacitance at low frequencies or high temperatures. The differences between certain dielectric constant determinations can be explained by the different combinations of sample dimensions and measurement frequencies that have been used. The dual values of the capacitance that can be measured lead to an apparent frequency dependence of the capacitance, reported by Huntley (1966). The dielectric constant calculated from the bulk capacitance, using the actual sample dimensions, is 36. Work at low temperatures (130K), on the same sample, produced a dielectric constant that is somewhat lower (25.5). The difference between these two values has been interpreted by assessing the effect of dipoles caused by excess oxygen, analysis indicates the level of non-stoichiometry as 0.005. It is interesting to note that the dielectric constant that is commonly used to parameterise the interatomic potentials (table 2.6) is 24. This is the value measured by A Briggs in 1957 and it is indeed fortunate that the conditions he chose to apply to his sample (frequency=178KHz) were sufficient to ensure the measurement of the bulk capacitance.

As part of this work the first measurement has been made of the static dielectric constant (23.6) in the antiferromagnetic phase below the magnetic phase transition at 30.8K. The measurement of the dielectric

constant above this temperature in the paramagnetic phase was 23.8 (close to the transition temperature at 43K) and corroborates the values obtained by single frequency techniques at higher temperatures (130K). Cooling the sample through the phase transition causes a decrease in the dielectric constant of approximately only 0.8%.

These measurements have now clarified the status of the static dielectric constant in uranium dioxide at low temperatures. It can be concluded that the most reasonable value to take for the dielectric constant of stoichiometric uranium dioxide is 23, which is not significantly different from the preciously accepted values and does not vary appreciably with temperature at low temperatures.

The identification of the boundary layer in the equivalent circuit cast some doubt on the previous conductivity data for uranium dioxide. Most of the previous work had been concerned with the acquisition of high temperature data and thus four point probe techniques had been applied. The nature of these experiments have minimised the effects of the boundary layer, as there would have been minimal areas of the conductor in contact with the material (Stratton et al 1980). The temperature dependence and the transition temperature of the high temperature conductivity data detailed in this thesis (section 5.5) correlates well

with the data of Bates et al (1967) and of other workers (section 2.3). Thus it can be concluded that the boundary layer has had little effect on the previously accepted conductivity (as measured at high temperatures) values.

The data of Bates (1967) displayed an odd frequency dependence, and this has been shown, from high temperature admittance studies, to arise plausibly from capacitance perturbations on the equivalent circuit for four point measurements. Although the exact origins of the capacitance effects have not been established, it can be reasonably assumed that they are in some way connected with the surface of the material and the measurement leads. Bates examined the frequency dependence of the modulus of the impedance, by measuring the voltage dropped across the sample for a constant ac current through it. The correct conversion of this data to conductivity values is dependent upon the proper evaluation of the equivalent circuit: Bates assumed a simple parallel or series combination for his analysis. Analysis has shown that the data of Bates were not compromised by his choice of a simple circuit over the one described in this thesis to analyse his data. Thus it can be assumed that a boundary, stray or surface layer capacitance played a contributary part in the curvature of the frequency plots reported by Bates.

The boundary layer had minimal effect on four point

measurements, though this is not the case for experiments where the application of the four point method is inappropriate eg high pressure measurements. The correct assignment of sample dimensions in calculating the electrical properties from the measurements is crucial. Knowledge of the correct circuit to use has allowed the extraction of conductivity data from experiments which have not been specifically designed for conductivity studies ie dielectric constant determinations. This has permitted activation energies to be assessed for both the bulk and boundary conductivities for disc shaped samples; the activation energies calculated in this manner for the bulk conductivity agree well with the previous low temperature values (section 5.5 and tables 2.1 and 2.2). Without this approach, it would have been impossible to analyse the high pressure data correctly, as these experiments were only able to examine the electrical properties of the boundary layer. The pressure dependences of the dielectric constant and conductance for the boundary layer are $-0.03 Kbar^{-1}$ and $6.5 \mu S Kbar^{-1}$, respectively. The zero pressure dielectric constant is 21.5: the samples used in this work had been recently reduced. The range of the binding (B) and hopping (D) energies for the carriers has been estimated as:

$0eV < B \text{ or } D < 0.17eV$, where $B+D=0.165eV$.

There have been several possible areas of further research identified by this work and these can be divided into two areas: 1) reinforcement of this work, 2) extension of these techniques to other materials.

1) The single crystal work reported in this thesis has been conducted on a minimal number of sample geometries (discs) and dimensions. Repeating this work for a different geometry for example on a bar will allow the bulk and boundary layer contributions to the sample impedance to be separated. Additionally the work detailed within this text could be repeated using a different measurement device to provide an alternate frequency range ie a frequency response analyser which provides frequencies down to 10^{-4}Hz. Low frequencies would allow more of the boundary profile to be traversed, thus the temperature dependence of the boundary layer could be examined at lower temperatures. The values calculated for the Mott Hubbard gap (U) from the high temperature ac data presented in this text are larger than the value calculated by Hyland and Ralph (1983) from the dc data of Killeen (1980), but closer to the calculated value of 3.6eV. These new values of U would, if included in the analysis of Hyland and Ralph, give larger thermal conductivities and specific heats than had previously been calculated. However it would be unwise to instigate a large scale re-examination ot

the previously calculated thermophysical data on the basis of these preliminary measurements of the ac conductivity. Thus these measurements will need experimental corroboration. Finally it could prove fruitful to repeat the low temperature (T<77K) work in a cryostat which could provide better stability near the phase transition. This would allow us to examine more carefully the dielectric constant in the vicinity of the phase transition.

2) Almost all of the existing high temperature conductivity measurements have been conducted on single crystal samples; however fuel pins are not constructed from such material. The most likely fuel for use within a reactor is polycrystalline uranium dioxide. Fuel pins are encased in stainless steel tubes with intimate contact between the fuel and the metal of the tube. As a consequence high temperature conductivity data for all components of the electrical system (bulk, grain boundaries and boundary layer) needs to be obtained for polycrystalline material, including the effects of stoichiometry and dopant level. Indeed the originally anticipated 1 to 3% burn ups for the fuel may eventually be increased up to 20%: the fuel would then consist of almost 40% fission products (JR Mathews to be published). Complex plane impedance studies would provide an ideal tool to use in such an examination as

the equivalent circuit for this material is anticipated as being quite complicated. Dielectric constant determinations would also be possible. There has been considerable interest in mixed oxide fuels. There is a lack of conductivity data for such materials. Only one set of conductivity data exists for the fuel $(U,Pu)O_2$ up to 1100K (Schmitz and Couty 1976). Thus conductivity measurements are needed to extend the data on the mixed fuels.

In conclusion, the technique of complex plane analysis has been shown to be a versatile and powerful tool in the examination of the electrical properties of uranium dioxide. The technique, properly handled, shows great potential for studies of mixed oxide fuels and a wide range of other materials.

REFERENCES

P Abelard and JF Baumard, Phys Rev B, 26 (1982), 1005

RJ Ackerman, RJ Thorn and GH Winslow, J Opt Soc Am, 49 (1959), 1107

DP Almond amd AR West, J Electroanal Chem, 186 (1985), 17

S Aronson, JE Rulli and BE Schaner, J Chem Phys, 35 (1961), 1382

A Arrott and JE Goldman, Phys Rev, 108 (1957), 948

JD Axe and GC Pettit, Phys Rev, 151 (1954),676

JL Bates, CA Hinman and T Kawada, BNWL-296 PT1 (1966)

JL Bates, BNWL-296 PT2 (1967)

JL Bates, CA Hinman and T Kawada, J Am Ceram Soc, 50 (1967), 652

MA Bredig, Etude des Transformations Cristallines a Haute Temperature, Colloques Int CNRS No 205 (1972), 183

A Briggs, Report to International Atomic Energy Agency: Vienna, 1964

P Browning, J Nucl Mater, 98 (1981),345

CRA Catlow and AB Lidiard, Proc Symposium in Thermodynamics of Reactor Materials, 2 (1974), 27

CRA Catlow, Proc Roy Soc, A353 (1977), 533

CRA Catlow and MJ Norgett, AERE Report, R.2763 (1976)

CRA Catlow, Proc Roy Soc, A364 (1978), 473

CRA Catlow, JD Comins, FA Germano, RT Harley, W Hayes

and IB Owen, J Phys C, 14 (1981), 329

AV Chadwick, Solid State Ionics, 8 (1983), 209

HC Chen, E Gartstein and TO Mason, J Phys Chem Solids, 43 (1982), 991

K Clausen, W Hayes, JE Macdonald, P Schnabel, MT Hutchings and JK Kjems, High Temperatures - High Pressures, 15 (1983), 383

K Clausen, W Hayes, JE Macdonald, R Osborn and MT Hutchings, Phys Rev Letts, 52 (1984), 1238

CE Derrington and M O'Keeffe, Nature: Phys Sci, 44 (1973), 246

CE Derrington, A Linder and M O'Keeffe, J Solid State Chem, 15 (1975), 171

NJ Dudney, RL Coble and HL Tuller, J Am Ceram Soc, 64 (1981), 627

AL Dragoo, CK Chiang, AD Franklin and J Bethin, Advances in Ceramics, 7 (1984), 184

F English and B Gossick, Solid State Electron, 7 (1964), 193

P Erdos and JM Robinson, The Physics of Actinide Compounds (Plenum Press 1983)

TH Etsell and SN Flengas, Chem Rev, 70 (1970), 339

J Faber and GH Lander, Phys Rev, 14 (1976), 1151

DF Fischer, JK Fink and L Liebowitz, J Nucl Mater, 102 (1981), 220

JK Fink, MG Chasanov and L Leibowitz, J Nucl Mater, 102 (1981), 17

BC Frazer, G Shirane, DE Cox and CE Olsen, Phys Rev, 140 (1965), A1448

IJ Fritz, J Appl Phys, 47 (1976), 4353

H Frohlich, Theory of dielectrics, 2nd Ed, Clarendon Press: Oxford (1958)

K Gesi and J Tateno, Japan J Appl Phys, 8 (1969), 1358

JH Harding, P Masri and AM Stoneham, J Nucl Mater, 92 (1980), 73

WE Henry, Phys Rev, 109 (1958), 1976

JM Honig, AA Cella and JC Cornwell, Rare Earth Research II: Gordon and Breach, New York, (1964), 255

DJ Huntley, Can J Phys, 44 (1966), 2952

MT Hutchings, Proc Symp Neutron Scattering: Argonne National Laboratory, 1981

G Hyland, J Nucl Mater, 113 (1983), 125

G Hyland and J Ralph, High Temperatures - High Pressures, 15 (1983), 179

S Iida, Japan J Appl Phys, 4 (1965), 833

S Ikeda, O Sakurai, K Uematsu, N Mizutani and M Kato, J Mater Sci, 20 (1985), 4593

RA Jackson, AD Murray, JH Harding and CRA Catlow, AERE report, TP1109 (1985)

WM Jones, J Gordon and EA Long, J Chem Phys, 20 (1952), 695

AK Jonscher, J Mater Sci, 13 (1978), 553

AK Jonscher, Dielectric Relaxation in Solids, Chelsea Dielectrics Press: London (1983), 62-95

AK Jonscher and JM Reau, J Mater Sci, 13 (1978), 563

DP Karim and AT ALdred, Phys Rev B, 20 (1979), 2255

JF Kerrisk and DG Clifton, Nucl Technol, 16 (1972), 531

JC Killeen. J Nucl Mater, 88 (1980), 185

MJM Leask, LEJ Roberts, AJ Walker and WP Wolf, J Chem Soc, (1963), 4788

HM Lee, J Ncl Mater, 56 (1975), 81

RP Lowndes, J Phys C, 4 (1971), 3083

JE Macdonald, PhD thesis St Johns College: Oxford, (1985)

DA MacInnes, J Nucl Mater 78 (1978), 225

DA MacInnes, Proc Intl Symp on Thermodynamics of Nuclear Materials (IAEA: Vienna), SM - 236/37 (1979), 129

JR Mathews, to be published in the Journal of the Chemical Society (Faraday discussions).

T Matsui and K Naito, J Nucl Mater, 138 (1986), 19

ZA Munir, Int J Thermophysics, 2 (1981), 177

HP Myers, T Jonsson and R Westin, Solid Statt Commun, 2(10) (1964), 321

P Nagels, M Denayer and J Deveresse, Solid State Commun, 1(2) (1963), 35

J Oberschmidt and D Lazarus, Phys Rev, 21 (1980), 177

PO Peron, Tech Rept AECL-3072, 1968

MH Rand, RJ Achermann, F Gronvold and A Pattoret, Rev Int Hautes Temper Refract Fr, 15 (1978), 355

F Schmitz and Y Couty, Plutonium 1975 and other Actinides, North Holland (1976), 165

J Schoenes, Phys Reports, 63 (1980), 301

K Shahi, Phys Status Solidi A, 41 (1977), 11

AM Stoneham, AERE Harwell Report, R.9598 (1981)

T Stratton, A McHale, DButton and HL Tuller, Materials Science Research vol 14 -surface and interfaces in ceramic and ceramic-metal systems, (1980), 71

GB Subba Rao, S Ramdas, PN Mahrotra and CNR Rao, J Solid State Chem, 2 (1970), 377

R Szwarc, J Phys Chem Solids, 30 (1969), 705

J Tateno, J Chem Phys, 81 (1984), 6130

HL Tuller and AS Nowick, J Phys Chem Solids, 38 (1977), 859

SN Vaidya, C Karunakaran, MD Karkhanavala and R Krishnan, J Nucl Mater, 60 (1976) 339

LB Valdes, Proc IRE, R282.12 (1953)

RK Willardson, JW Moody and HL Goering, J Inorg Nucl Chem, 6 (1958), 19

BTM Willis, Nature, 197 (1965), 755

AJ Winnubst, MJ Verkerk and AJ Burggraaf, Advances in Ceramics, 7 (1984), 177

AL Wright, TS Cress, AM Smith and JM Rochelle, Trans Am Nucl Soc, 34 (1980), 551

AA Zaky and R Hawley, Dielectric Solids, Routledge and Keegan Paul: London (1970), 27-51